BIOLOGICAL MARKERS: BLURRED IN TIME AND SPACE

by

Christopher H. Remien

A dissertation submitted to the faculty of
The University of Utah
in partial fulfillment of the requirements for the degree of

Doctor of Philosophy

Department of Mathematics

The University of Utah

December 2012

The University of Utah Graduate School

STATEMENT OF DISSERTATION APPROVAL

The dissertation of **Christopher H. Remien**

has been approved by the following supervisory committee members:

Frederick R. Adler	, Chair	**Aug. 15, 2012** Date Approved
James P. Keener	, Member	**Aug. 15, 2012** Date Approved
Fernando Guevara Vasquez	, Member	**Aug. 15, 2012** Date Approved
Thure E. Cerling	, Member	**Aug. 15, 2012** Date Approved
James R. Ehleringer	, Member	**Aug. 15, 2012** Date Approved

and by **Peter E. Trapa**, Chair of the Department of **Mathematics**

and by Charles A. Wight, Dean of The Graduate School.

ABSTRACT

We develop mathematical models relating measured biological markers to how animals process nutrients and toxins. Our models track molecules as they are ingested, transformed through metabolic processes, and excreted, and relate measurements of biological markers to these processes. We focus on specific problems of practical interest. We begin by developing a model of acetaminophen metabolism and use our model to estimate outcome of acetaminophen overdose patients. Acetaminophen overdose increasingly occurs as a result of chronic use. We analyze the dynamics of chronic use and find threshold dynamics that result from the structure of acetaminophen metabolism. We next study animal nitrogen metabolism. Nitrogen stable isotope ratios in consumer tissue are used by ecologists to estimate diet and trophic dynamics, but feedbacks between diet and physiology complicate the relationship between diet and the nitrogen isotope ratio of consumer tissue. We develop a model of animal nitrogen metabolism to study the influence of diet on stable nitrogen isotope ratios of consumer tissue. Finally, hair is often measured to understand how animals process nutrients and toxins because organic and inorganic substances are incorporated into hair, remaining inert for long periods of time. We develop a model based on the known physiology of hair growth to describe the signal averaging caused by bundling multiple hairs for segmental analysis.

CONTENTS

ABSTRACT iii

LIST OF FIGURES vi

LIST OF TABLES viii

ACKNOWLEDGEMENTS ix

CHAPTERS

1. INTRODUCTION 1

2. MATHEMATICAL MODELING OF LIVER INJURY AND DYSFUNCTION AFTER ACETAMINOPHEN OVERDOSE 3

2.1 Introduction 3
2.2 Materials and methods 4
2.2.1 Model background 4
2.2.2 Model description 4
2.2.3 Patients 8
2.2.4 Ethics statement 8
2.2.5 Serum creatinine 9
2.2.6 Fitting the model to individual patients 9
2.2.6.1 Posttreatment model fits 9
2.2.6.2 Pretreatment model fits 11
2.3 Results 11
2.4 Discussion 18

3. CHRONIC ACETAMINOPHEN USE AND ACUTE LIVER INJURY 26

3.1 Introduction 26
3.2 Methods 27
3.2.1 Chronic acetaminophen metabolism and marker dynamics 27
3.2.2 Time-invariant chronic use 28
3.2.2.1 Steady states 28
3.2.2.2 Stability of steady states 29
3.2.2.3 Approximation of bifurcation points 29
3.2.3 APAP-induced liver injury on background of chronic use 31
3.2.4 Single overdose fits to markers from chronic use 36
3.3 Results 36
3.4 Discussion 38

4. HOW ANIMAL NITROGEN METABOLISM SHAPES ISOTOPIC SIGNATURES OF TROPHIC DYNAMICS **48**
4.1 Introduction 48
4.2 Methods 50
4.2.1 Nitrogen cycling in an animal 50
4.2.2 Model description 50
4.2.3 Model parameterization 52
4.2.4 Steady states 55
4.2.5 Stable isotope model 55
4.2.6 Stable isotope steady states 57
4.2.7 Diet isotope switch 57
4.3 Results 61
4.4 Discussion 61

5. DECONVOLUTION OF ISOTOPE SIGNALS FROM BUNDLES OF MULTIPLE HAIRS **65**
5.1 Introduction 65
5.2 Methods 66
5.2.1 Model formulation 66
5.2.1.1 Mapping single hair signal to hair bundle measurements 66
5.2.1.2 Derivation of integration kernel 67
5.2.1.3 Averaging due to sample interval 69
5.2.2 Inverse method 70
5.3 Results 70
5.4 Application of inverse method to murder victim data 77
5.4.1 Estimating equilibrium signal from estimated primary body signal 80
5.4.2 Region-of-origin maps 80
5.5 Discussion 81

REFERENCES **86**

LIST OF FIGURES

2.1 Diagram of model of liver damage following acetaminophen overdose 5
2.2 Estimates of time since overdose and overdose amount 13
2.3 Individual patient results 14
2.4 Individual patient results 15
2.5 Individual patient results 16
2.6 Individual patient results 17
2.7 Description of the Model of Acetaminophen-induced Liver Damage 23
3.1 Bifurcation diagram as function of acetaminophen intake 30
3.2 Approximation of bifurcation points 32
3.3 Scenarios of chronic use followed by overdose 33
3.4 Scenarios of chronic use followed by decreased glutathione prduction 35
3.5 Example of typical chronic marker fit 37
3.6 Pulse of acetaminophen needed for given damage 41
3.7 Reduction of glutathione production required for given damage 42
3.8 Extent of damage for chronic-pulse scenarios 43
3.9 Extent of damage for decreased glutathione production scenarios 44
3.10 Estimated liver damage compared to actual extent of damage 45
4.1 Diagram of animal nitrogen model 51
4.2 Steady states as a function of dietary nitrogen input 56
4.3 Isotope steady states as a function of dietary nitrogen intake 58
4.4 Turnover of body pools following diet switch with intake fixed 59
4.5 Turnover of body pool following diet switch for various intakes 60
5.1 Integral transform kernel as function of length 73
5.2 Summary statistics of transform kernel 74
5.3 Expected bundle signal for synthetic input signal 75
5.4 Reconstruction of primary input signal 76
5.5 Reconstruction of hair of murder victim 78
5.6 Maps of reconstruction of isotopic signature from hair of a murder victim 79

5.7 Comparison of regions of origin of murder victim 82
5.8 Comparison of regions of origin of murder victim 82

LIST OF TABLES

2.1 Sensitivity, specificity, PPV, and NPV 12
2.2 Estimates of time since overdose, overdose amount, and outcome 19
2.3 Summary of how changes in parameter values affect predictions of outcome . . 21
3.1 Regression of estimated time since overdose to actual time since overdose 39
3.2 Regression of estimated liver damage to actual liver damage 40
4.1 Factors affecting nitrogen stable isotope ratios of consumers 49
4.2 Variables in nitrogen model 53
4.3 Parameters in nitrogen model 54
5.1 General distributions used in hair bundle modeling 67
5.2 Parameters and specific distributions used in hair bundle modeling. 72

ACKNOWLEDGEMENTS

Thanks to my family for their support. They believed in me, despite not knowing exactly what I was doing.

Dr. Fred Adler taught me much about creative problem solving. Group meetings were always spirited and fun, and I always looked forward to our meetings. You taught me how to approach modeling, to embrace complexity when needed, but not for its own sake.

I am greatly indebted to Dr. Thure Cerling for teaching me, a naive mathematician, biogeochemistry. From the lab to the field, you taught me how to get things done, especially when creative improvisation is required. The field seasons in Kenya taught me so much, not least that lab troubleshooting and data analysis are not always the most difficult part of science. I really enjoyed all of our adventures.

Dr. James Keener has built an incredible, supportive, creative program to train and inspire mathematical biologists, without which I would not have come to Utah. You have taught me that good problems are viscerally exciting and found everywhere, and that very applied math seminars are the perfect compliment to traditional group meetings.

Dr. James Ehleringer, along with Dr. Thure Cerling, has made Utah a leader in stable isotope biogeochemistry. In particular, the summer stable isotope short course is a wonderful program. I learned something new every year and had so many positive interactions as a result of that course. Dr. Fernando Guevara Vasquez offered insight to and interest in my problems.

Many people helped me with projects contributing to this thesis. Dr. Norman Sussman's intuition and eagerness to branch out and talk to mathematicians led to a great collaboration. I appreciate your excitement and insight. Dr. Terry Box and Lindsey Waddoups supplied acetaminophen overdose patient data and offered insight into the nature acetaminophen overdose that a mathemetician can not aquire in an office. Lesley Chesson and Dr. Luciano Valenzuela helped me with the application of our hair bundling model to stable isotope measurements.

I thank David Kimutai, Douglas Kimanzi, and the many individuals who contributed to three memorable field seasons. David Kimutai was an incredible resource and taught

me the environment and wildlife of Kenya. Douglas Kimanzi was a gracious host, safely escorting us around his country.

Thanks to vice presidents and more recently officers of the Seger/Adler Lab, especially Jon Seger and Vicky Rowntree. Thanks to the members of the Cerling Lab, who were patient and understanding as they taught me the workings of a stable isotope lab. Thanks to the math biology graduate students, who became not just colleagues, but some of my best friends. Thanks to my biology friends, from whom I learned much science as we slogged on skis and bikes in the Wasatch. Thanks to my former teachers, who inspired me to continue studying mathematics.

Thanks to Diana Mitchell. You have supported me more than you know. Thanks to Newton, Jasper, and Louie for making me smile and getting me outside.

I was funded by IGERT (NSF-DGE-0217424) and RTG (NSF-DMS-0354259).

CHAPTER 1

INTRODUCTION

Animals ideally process nutrients and toxins in a way that maximizes the opportunity for growth and reproduction while minimizing damage, dynamically altering their response to changing inputs and environmental conditions. Complex cascades of regulation, fine-tuned through generations of selected refinement, allow for a dynamic, adaptive response to ever-changing conditions. In animals, the liver plays a central role in this regulation. Hepatocytes are responsible for detoxification of the blood and processing nutrients, and as such play a major role in the regulation and control required to maintain homeostasis.

Those interested in understanding how animals process nutrients and toxins must make observations and measurements. Data must be collected and interpreted, experiments refined, but it is often impossible or impractical to measure the process of interest directly. Instead, researchers rely on indirect measurements of biological markers. The complexity of life, the regulation and control, often leads to a complex, nonlinear relationship between measurements and the process of interest.

We wish to understand how animals process nutrients and toxins by better interpreting measurements. We ideally connect measurements of biological markers to the biological state or process of interest with mathematical models accounting for the regulation and control that is central to physiology, lending new insight to measurements. Questions arise from human disease, human and animal nutrition, or ecology, but rely on a mechanistic understanding metabolism. The mathematics is built upon conservation. We dynamically track nutrients and toxins as they are ingested, transformed, and excreted, and link these processes to measurable biological markers. Using our mathematical models, we further interpret the marker measurements to gain new insight.

While we are interested in how animals process nutrients and toxins in general, we focus on specific questions of practical interest. We begin in Ch. 2 by developing a model of acetaminophen toxicity. We wish to understand how the liver processes acetaminophen and how the build up of toxic metabolites causes liver damage. While safe in small doses, large

doses of acetaminophen can lead to acute liver failure and ultimately death. We use our model to interpret clinical data of markers of liver damage to predict if patients will live or die following an overdose. If a patient is predicted to die, liver transplantation may be the only life saving treatment. In recent years, overdoses increasingly occur over a background of chronic use. In Ch. 3 we further analyze the dynamics of our model of acetaminophen toxicity, with the addition of chronic use. The structure of the dynamic response of the liver to acetaminophen overdose leads to a threshold system, such that damage occurs acutely, if at all, even with chronic use. The acute nature of liver injury creates characteristic injury curves and robust predictions of outcome using the model devloped in Ch. 2, even with a background of chronic use. The liver also plays a central role in protein metabolism. In Ch. 4 we develop a dynamic model of nitrogen metabolism. The model tracks the fate of nitrogen as it is ingested as protein, converted to the toxic metabolite ammonia, processed by the liver to urea, and excreted. We use the model to estimate the role of dietary protein intake on stable nitrogen isotope ratios of tissue. Finally, in Ch. 5 we develop a model of how chemical signals in hair are blurred in sample preparation. Drugs, chemicals, and toxins are incorporated into hair, which can be sampled segmentally to provide a chronology of measurements. Variations of hair growth due to physiology can blur the chemical signal of interest. We develop a model based on the physiology of hair growth that we use to better interpret measurements. The regulation and control that is central to physiology leads to complex relationships between the signal of interest and measured biological markers. The mathematical models are built on known physiology, tracking molecules from ingestion to measurement, and are used to better interpret the blurred signal of biological markers.

CHAPTER 2

MATHEMATICAL MODELING OF LIVER INJURY AND DYSFUNCTION AFTER ACETAMINOPHEN OVERDOSE: EARLY DISCRIMINATION BETWEEN SURVIVAL AND DEATH [1]

2.1 Introduction

Acetaminophen (APAP: N-acetyl-para-aminophenol) is the leading cause of acute liver injury in the United States, accounting for some 56,000 emergency room visits, 26,000 hospital admissions, and about 500 deaths annually [1]. APAP toxicity is caused by the formation, within hepatocytes, of N-acetyl-p-benzoquinoneimine (NAPQI), a highly reactive benoquinonamine [2, 3]. Intracellular NAPQI initially binds to glutathione (GSH), and is safely eliminated [4, 5]. Once GSH stores are depleted, residual free NAPQI reacts with cellular components and causes injury to APAP-metabolizing hepatocytes [6, 7]. Early administration of the GSH precursor, N-acetylcysteine (N-Ac), ideally within 12 hours of overdose, prevents life-threatening liver injury and ensures recovery [8]. Later administration may limit the liver injury, but its utility decreases with time [9]. In the presence of a sufficiently large overdose, the administration of N-Ac beyond a certain time window becomes futile. In these cases, liver transplantation becomes the only life-saving measure.

A number of factors may determine whether a dose of APAP is fatal. Among the most important are the size of the overdose and the time to first administration of N-Ac [8]. Unfortunately, these two values are frequently not available at the time of admission to the hospital: patients often arrive confused or comatose, the family is usually unaware of the

---

[1] REPRINTED WITH PERMISSION FROM HEPATOLOGY: Remien CH, Adler FR, Waddoups L, Box TD, and Sussman NL. Mathematical modeling of liver injury and dysfunction after acetaminophen overdose: Early discrimination between survival and death. *Hepatology*, 56(2):727-734, 2012.

timing or the dose of drug taken, and concomitant use of other medications or drugs often obscures the clinical picture.

We therefore sought a method for rapidly determining the time of overdose, extent of injury, and likelihood of spontaneous survival using laboratory data available at the time of admission. Our method is based on a mathematical model that describes typical hepatic injury progression, dependent only on overdose amount. Fitting patient laboratory values to our mathematical model allows for the estimation of overdose amount and timing, as well as a prediction of outcome. We tested the mathematical model on 53 patients from the University of Utah.

2.2 Materials and methods

2.2.1 Model background

Our mathematical model, the Model of Acetaminophen-induced Liver Damage (MALD), is based on a reproducible pattern of APAP-induced liver injury. The enzymes aspartate aminotransferase (AST) and alanine aminotransferase (ALT) are released by injured hepatocytes [10, 11]. These enzymes peak at about 36 hours from initial injury and have distinct injury and clearance curves. AST concentration in blood is initially approximately double that of ALT, with a clearance rate of about 50 % every 24 hours. ALT peaks at about the same time as AST, but with a slower elimination rate of about 33 % every 24 hours [12]. These measures of damage are complemented by a measure of liver function, prothrombin time/ international normalized ratio (INR). Decreased production of essential clotting factors manifests as reduced clotting and increased INR, again with characteristic rates of increase and decay [13]. The values of AST, ALT, and INR at the time of admission thus encode the course of disease progression over time and can be used, with a suitable mathematical model, to estimate initial dose and time of overdose.

2.2.2 Model description

We developed a system of nonlinear ordinary differential equations to describe the temporal dynamics of APAP-induced acute liver failure (ALF) based on known mechanisms of APAP metabolism. The equations describe NAPQI production from APAP metabolism, glutathione conjugation, hepatocyte death by NAPQI, release and clearance of AST and ALT in the blood, hepatocyte regeneration, and clotting factor production (Fig. 2.1).

The dynamics of total serum APAP (A), intracellular NAPQI concentration (N), intracellular GSH concentration (G), number of functional hepatocytes (H), number of damaged

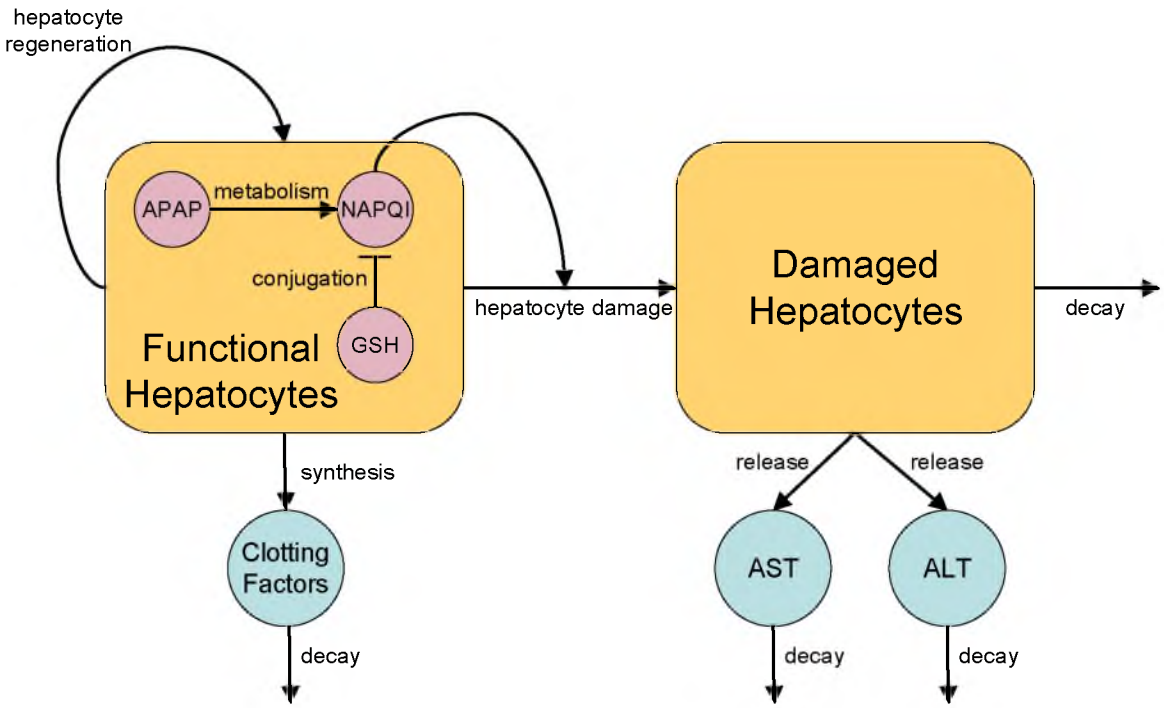

Figure 2.1. A schematic diagram representing the dynamics of the mathematical model. A fraction of APAP is oxidized to NAPQI, bound to GSH, and safely eliminated. As GSH stores are depleted, NAPQI damages hepatocytes, releasing AST and ALT into the blood. Meanwhile, functional hepatocytes regenerate and produce essential clotting factors. Red represents the intracellular variables, yellow represents healthy and damaged hepatocytes, and blue represents markers of liver damage.

hepatocytes (Z), serum AST concentration (S), serum ALT concentration (L), and serum clotting factor concentration (F) are governed by the following system of ordinary differential equations:

APAP $$\frac{dA}{dt} = -\frac{\alpha}{H_{max}} AH - \delta_A A$$

NAPQI $$\frac{dN}{dt} = \frac{qp\alpha}{H_{max}} A - \gamma NG$$

GSH $$\frac{dG}{dt} = \kappa - \gamma NG - \delta_G G$$

Functional Hepatocytes $$\frac{dH}{dt} = rH\Big(1 - \frac{H+Z}{H_{max}}\Big) - \eta NH$$

Damaged Hepatocytes $$\frac{dZ}{dt} = \eta NH - \delta_Z Z$$

AST $$\frac{dS}{dt} = \frac{\delta_Z \beta_S}{\theta H_{max}} Z - \delta_S (S - S_{min})$$

ALT $$\frac{dL}{dt} = \frac{\delta_Z \beta_L}{\theta H_{max}} Z - \delta_L (L - L_{min})$$

Clotting Factor $$\frac{dF}{dt} = \beta_F \Big(\frac{H}{H_{max}} - F\Big).$$

APAP is cleared by conjugation at a rate $\alpha \dfrac{H}{H_{max}}$, and a small amount is cleared unconjugated at rate δ_A. A fraction p of the APAP is converted to NAPQI and is cleared at a rate γG. GSH has a constant production κ and decays at a rate δ_G. Hepatocytes grow logistically with rate r saturating at H_{max} and become damaged at a rate ηN releasing AST and ALT into the blood at rates $\delta_Z \beta_S/(\theta H_{max})$ and $\delta_Z \beta_L/(\theta H_{max})$, respectively. Clotting factors are produced by hepatocytes and decay at a rate β_F. INR (I) is related to the concentration of clotting factors by the algebraic equation $I = \left(\frac{1+F_{min}}{F+F_{min}}\right)^4$.

The variables and parameters can be divided into those describing hepatocyte, APAP, glutathione, INR, and AST/ALT dynamics. Functional hepatocytes (H) become damaged hepatocytes (Z) and regenerate with the following parameters:

- The number of hepatocytes in a healthy liver is $H_{max} = 1.6 * 10^{11}$ cells [12, 14].
- Damaged hepatocytes lyse with rate $\delta_Z = 5$ /day.
- Functional hepatocytes regenerate with rate $r = 1$/day [15].
- Functional hepatocytes become damaged with rate $\eta = 5.12 * 10^{13}$ cell/mol/day.

- The fraction of liver required for survival is $\mu = 0.3$ [16].

Serum APAP (A) is a surrogate for liver APAP, which is converted to NAPQI (N) with the following parameters:

- APAP is cleared by hepatocytes with rate $\alpha = 6.3$/day [17].
- APAP is cleared unconjugated with rate $\delta_A = 0.33$/day [2, 3].
- The fraction of APAP that is oxidized to NAPQI is $p = 0.5$ [2, 3].
- The conversion factor from grams of APAP to mol of NAPQI is $q = 0.0067$ mol/g.

GSH (G) is associated with the following parameters:

- GSH binds to NAPQI with rate $\gamma = 1.6 * 10^{18}$ cell/mol/day [18].
- GSH decays with rate $\delta_G = 2$/day [19, 20, 21]
- GSH is produced with rate $\kappa = 1.375 * 10^{-14}$ mol/cell/day.

INR (I) is related to the clotting factor concentration as a fraction of normal (F) and is associated with the following parameters:

- Clotting factor VII is cleared with rate $\beta_F = 5$/day [22].
- The minimum clotting factor concentration is $F_{min} = 0.75$.

Serum AST concentration (S) and serum ALT concentration (L) increase and decay with the following parameters:

- AST is cleared with rate $\delta_S = 0.92$/day [12].
- ALT is cleared with rate $\delta_L = 0.35$/day [12].
- The total amount of AST in a healthy liver is 200,000 IU.
- The total amount of ALT in a healthy liver is 84,800 IU.
- The amount of blood in a human body is $\theta = 5$ L.
- The minimum AST level is $S_{min} = 12$ IU/L.

- The minimum ALT level is $L_{min} = 9$ IU/L.

Six parameters were adjusted to match properties of the data, independent of patient survival information. The amounts of AST and ALT in the liver, β_S and β_L, respectively, were scaled to the maximum observed AST and ALT values, and the minimum AST and ALT levels, S_{min} and L_{min}, respectively, were scaled to the minimum observed AST and ALT values. The minimum clotting factor concentration F_{min} was scaled to the maximum observed INR value. The damaged hepatocyte lysis rate δ_Z was adjusted to the timing of peak AST and ALT values.

Two parameters were scaled to the dose of APAP required for hepatotoxicity and death. The glutathione production rate, κ, was scaled to the dosage at which glutathione reserves are depleted. The minimum dosage predicted to lead to hepatotoxicity varies, but typically ranges from 7.5 to 10 g for an adult [8, 23]. We chose a slightly lower value of 6.0 g for the dosage at which glutathione reserves are depleted. The rate at which hepatocytes become damaged by NAPQI, η, is a scaling factor that was chosen so that a 20 g overdose is equivalent to 70 % hepatic necrosis and predicted death.

2.2.3 Patients

Between January 1, 2006, and December 31, 2009, all hospital discharges from the University of Utah were queried for the diagnosis of severe, acute APAP toxicity. Charts were excluded if they included acute hepatitis A or B, autoimmune hepatitis, Wilson Disease, or multisystem failure. Laboratory data and admission and discharge notes were further reviewed to identify cases in which acute liver disease was due to APAP overdose only. Charts that had overdose with additional medications were not included in this analysis. Demographics, N-Ac administration, and medical outcome information were collected. Laboratory results of AST, ALT, INR, bilirubin, and creatinine were also collected. Charts without at least one measure of AST, ALT, and INR were excluded from the study. In total, 53 patients were included. The patient population was diverse, with varying alcohol use, body mass index, and ingestion type, including suicide attempts, single accidental overdoses, and multiple day chronic overdoses.

2.2.4 Ethics statement

Patient consent was not obtained because data were retrospective, were based on standard care, and were analyzed anonymously. The protocol was approved by the Institutional

Review Board (IRB) of the University of Utah in accordance with the Declaration of Helsinki.

2.2.5 Serum creatinine

Serum creatinine was added as an additional criterion separate from the model because it is a marker of kidney damage and our dynamic model does not describe kidney damage. Because kidney function is ultimately important in survival in APAP overdose, patients with serum creatinine greater than 3.4 mg/dL were predicted to die [24].

2.2.6 Fitting the model to individual patients

Upon admission, before administration of N-Ac, a patient's AST, ALT, and INR values in the mathematical model are a function of two parameters, APAP overdose amount, A_0, and time since overdose, τ. These two parameters were estimated using weighted least-squares and values of AST, ALT, and INR on admission. The weights were determined by posttreatment model fits.

2.2.6.1 Posttreatment model fits

To estimate uncertainty in measurements of AST, ALT, and INR, we define a posttreatment model as a special case of the pretreatment model. Treatment with N-Ac leads to a high concentration of intracellular GSH, preventing further damage to hepatocytes (i.e., $N = 0$). This reduces the AST subsystem to

$$\begin{aligned}\frac{dZ}{dt} &= -\delta_Z Z \\ \frac{dS}{dt} &= \frac{\delta_Z \beta_S}{\theta H_{max}} Z - \delta_S (S - S_{min}),\end{aligned}$$

the ALT subsystem to

$$\begin{aligned}\frac{dZ}{dt} &= -\delta_Z Z \\ \frac{dL}{dt} &= \frac{\delta_Z \beta_L}{\theta H_{max}} Z - \delta_L (L - L_{min}),\end{aligned}$$

and the INR subsystem to

$$\begin{aligned}
\frac{dZ}{dt} &= -\delta_Z Z \\
\frac{dH}{dt} &= rH(1 - \frac{H+Z}{H_{max}}) \\
\frac{dF}{dt} &= \beta_F(\frac{H}{H_{max}} - F) \\
I &= \Big(\frac{1+F_{min}}{F+F_{min}}\Big)^4.
\end{aligned}$$

The posttreatment model subsystems were fit to individual patients using least squares. In the AST subsystem, the modeled AST value is a function of two parameters, the modeled AST concentration at the time of admission, S_0, and the number of damaged hepatocytes on admission, Z_0. For each individual patient, the best fit solution is the one that minimizes, over all possible combinations of S_0 and Z_0, the sum of the squared residual

$$\sum_i \Big(\log(AST_i) - \log(S_i(S_0, Z_0))\Big)^2,$$

where AST_i is the patient's measured AST value i days after the first measurement, and $S_i(S_0, Z_0)$ is the modeled AST value i days after the first measurement with initial conditions S_0 and Z_0. All logarithms indicate the natural log. The residual for each measurement is defined as $\log(AST_i) - \log\Big(S_i(S_0^*, Z_0^*)\Big)$ where S_0^* and Z_0^* are the AST and damaged hepatocyte initial conditions that minimize the least squares problem, respectively. The standard deviation of all of the residuals from all measurements of AST from all patients is $\omega_S = 0.60$.

Using the same approach described above, but replacing AST_i, S_i, and S_0 by ALT_i, L_i, and L_0, respectively, the standard deviation of all of the residuals from all measurements of ALT from all patients is $\omega_L = 0.43$.

For INR, the modeled value I_i depends on three parameters, modeled clotting factor concentration at the time of admission, F_0, modeled number of damaged hepatocytes at admission, Z_0, and modeled number of functional hepatocytes at admission, H_0. Again minimizing the least squares difference between measured INR_i and modeled $I_i(F_0, Z_0, H_0)$, the standard deviation of the residuals from all measurements of all patients is $\omega_I = 0.26$.

2.2.6.2 Pretreatment model fits

For each patient, the estimated A_0 and τ are those that minimize

$$R = \Big(\frac{\log(AST) - \log(S(A_0,\tau))}{\omega_S}\Big)^2 + \Big(\frac{\log(ALT) - \log(L(A_0,\tau))}{\omega_L}\Big)^2 + \Big(\frac{\log(INR) - \log(I(A_0,\tau))}{\omega_I}\Big)^2$$

where AST, ALT, and INR are a patient's measured AST, ALT, and INR on admission, and S, L, and I are modeled AST, ALT, and INR for overdose amount A_0 at time τ since overdose.

The line separating predicted recovery and predicted death in Fig. 2.2 was determined by numerically solving the full pretreatment model for a range of A_0, marking the time since overdose when H equals 30 % of its initial value (i.e., 70 % hepatic necrosis occurs). The estimated probability of death for each patient is calculated as the fraction of R within 2 of R^* for which A_0 and τ lie in the region of predicted death.

The confidence regions of A_0 and τ for individual patients in Figs. 2.3, 2.4, 2.5, and 2.6 are defined as follows. We begin with the best least squares estimate for A_0 and τ, where the residual R takes its minimum R^*. We then find regions A_0 and τ for which R is within 0.5 of R^*, R exceeds R^* by 0.5 to 1, R exceeds R^* by 1 to 1.5, and R exceeds R^* by 1.5 to 2.

To test the sensitivity of model predictions to parameters, we fit patients to the pretreatment model with each parameter perturbed by 50 % and 150 % of its original value.

2.3 Results

We tested the model on 53 patients from the University of Utah. The time since overdose and overdose amount were estimated for each patient using initial measurements of AST, ALT, and INR on admission (Fig. 2.2). Based on the extent of estimated liver injury, the model predicts death for patients who took over 20 g of APAP without N-Ac administration within the first 24 hours.

Excluding patients who were transplanted, death versus recovery was predicted with 75 % sensitivity and 95 % specificity (Tab. 2.1). With the addition of initial serum creatinine exceeding 3.4 mg/dL, sensitivity increased to 100 %. For this dataset the subset of the Kings College Criteria (KCC) to which we had access (INR $>$ 6.5 and creatinine $>$ 3.4 mg/dL) had 13 % sensitivity and 100 % specificity. Only one patient had both INR $>$ 6.5 and creatinine $>$ 3.4 on admission. Thinking of the KCC as either INR $>$ 6.5 or creatinine $>$

Table 2.1. Sensitivity, specificity, PPV, and NPV for a subset of King's College Criteria (INR > 6.5 and creatinine > 3.4), either INR > 6.5 or creatinine > 3.4 mg/dL, and the current study both with and without creatinine as an independent marker. Absolute numbers and 95% Clopper-Pearson confidence interval are given in parentheses.

Model	Specificity	Sensitivity	PPV	NPV
INR > 6.5 and creatinine > 3.4 mg/dL	1 (43/43, 0.92-1)	0.13 (1/8, 0-0.53)	1 (1/1, 0-1)	0.86 (43/50, 0.73-0.94)
INR > 6.5 or creatinine > 3.4 mg/dL	0.95 (41/43, 0.84-0.99)	0.88 (7/8, 0.47-1)	0.78 (7/9, 0.4-0.97)	0.98 (41/42, 0.87-1)
MALD (No Creatinine)	0.95 (41/43, 0.84-0.99)	0.75 (6/8, 0.35-0.97)	0.75 (6/8, 0.35-0.97)	0.95 (41/43, 0.84-0.99)
MALD (With Creatinine)	0.91 (39/43, 0.78-0.97)	1 (8/8, 0.63-1)	0.67 (8/12, 0.35-0.90)	1 (39/39, 0.91-1)

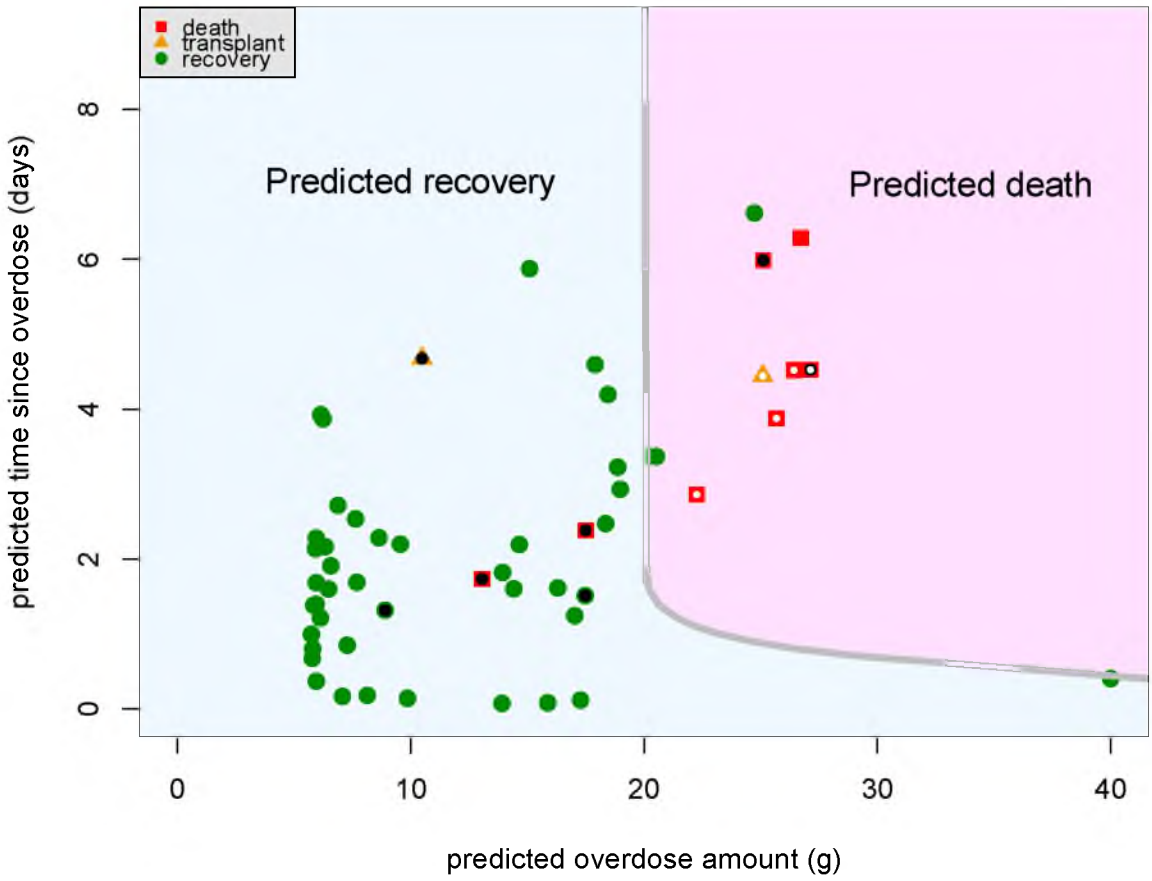

Figure 2.2. MALD derived estimates of time since overdose and overdose amount for 53 patients with known APAP overdose. Red squares indicate eventual death, green circles recovery, and orange triangles transplant. Small white dots indicate INR > 6.5 and small black dots indicate serum creatinine > 3.4 mg/dL on admission. The gray line indicates overdose amounts and times since overdose for which 70 % hepatic necrosis is predicted. Patients to the right and above the gray line are predicted to die.

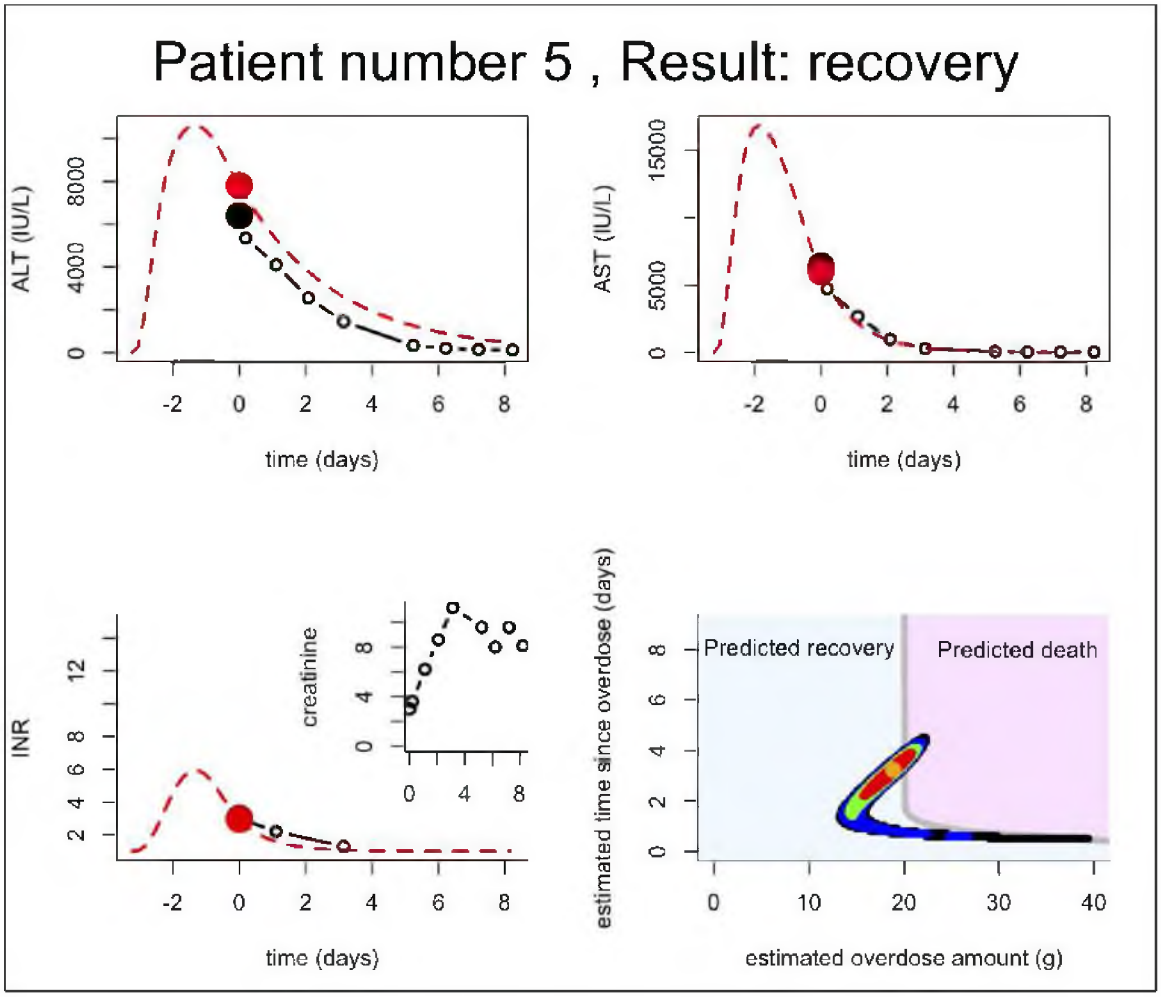

Figure 2.3. Markers of liver damage (small black open circles) and model predictions (red dashed line) based on least squares fits of initial AST, ALT, and INR (large black filled circle) to modeled AST, ALT, and INR (large red filled circle). Time $t = 0$ indicates the time of admission to hospital. The estimated overdose amount and time since overdose for each patient is given by the orange dot in the lower right panel.

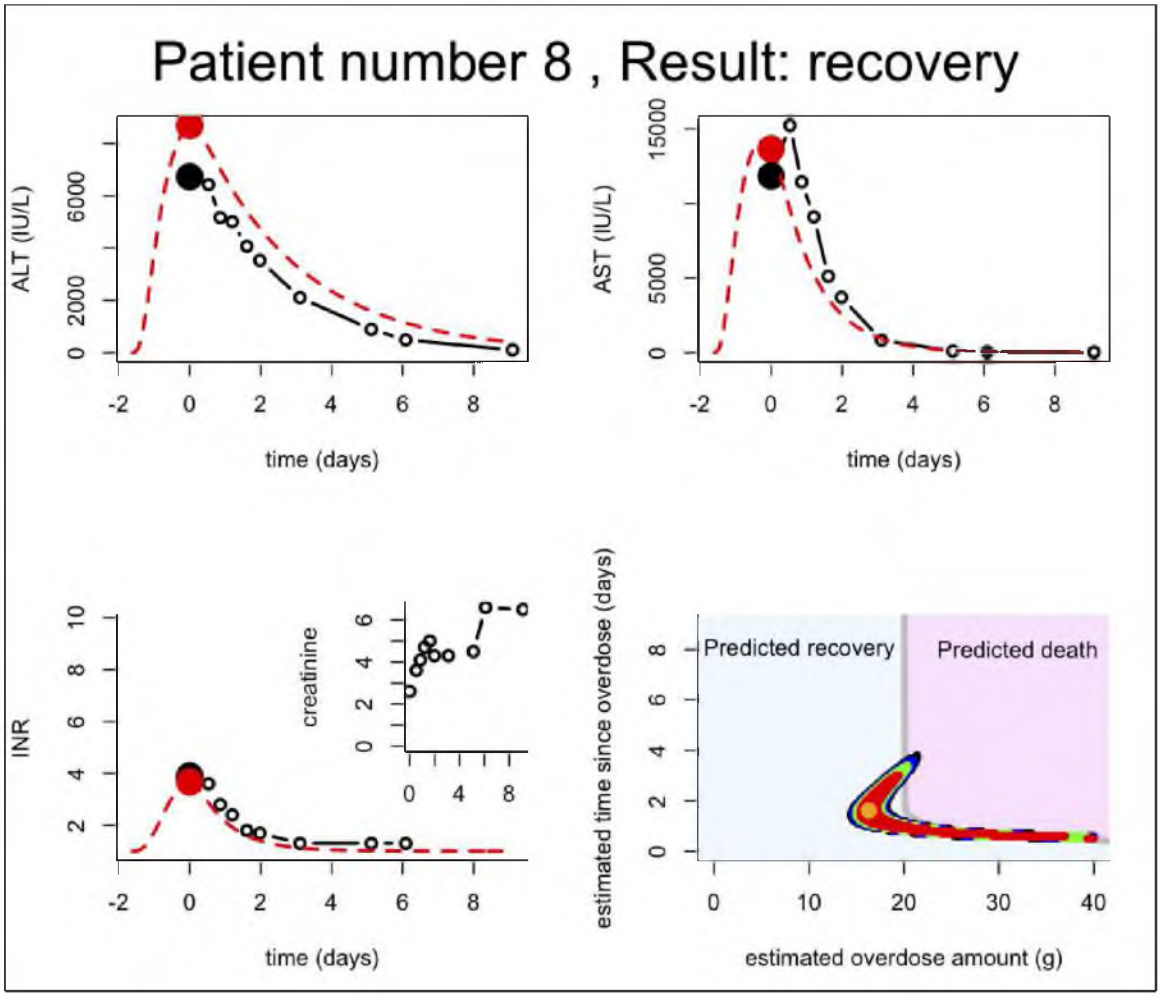

Figure 2.4. Markers of liver damage (small black open circles) and model predictions (red dashed line) based on least squares fits of initial AST, ALT, and INR (large black filled circle) to modeled AST, ALT, and INR (large red filled circle). Time $t = 0$ indicates the time of admission to hospital. The estimated overdose amount and time since overdose for each patient is given by the orange dot in the lower right panel.

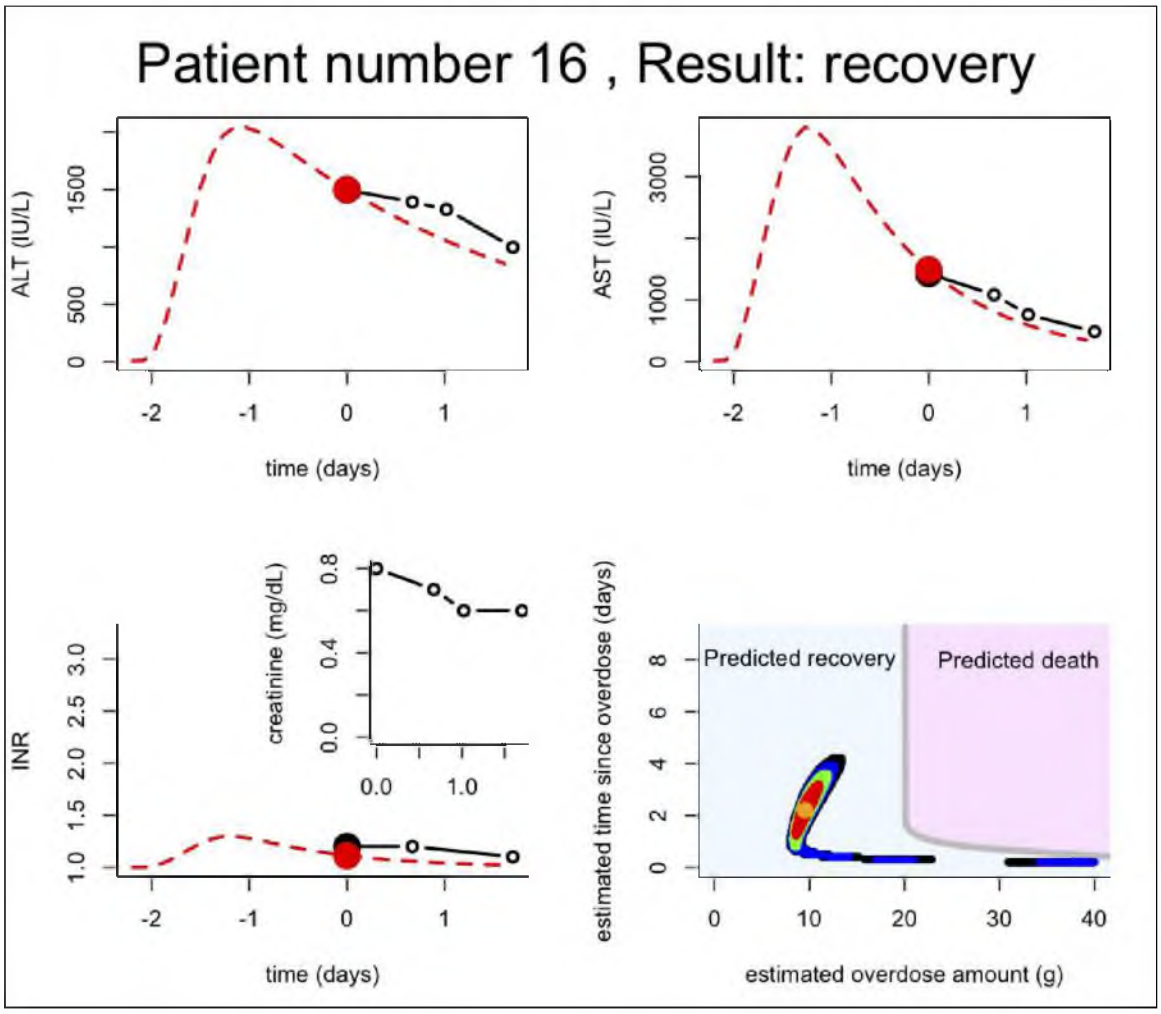

Figure 2.5. Markers of liver damage (small black open circles) and model predictions (red dashed line) based on least squares fits of initial AST, ALT, and INR (large black filled circle) to modeled AST, ALT, and INR (large red filled circle). Time $t = 0$ indicates the time of admission to hospital. The estimated overdose amount and time since overdose for each patient is given by the orange dot in the lower right panel.

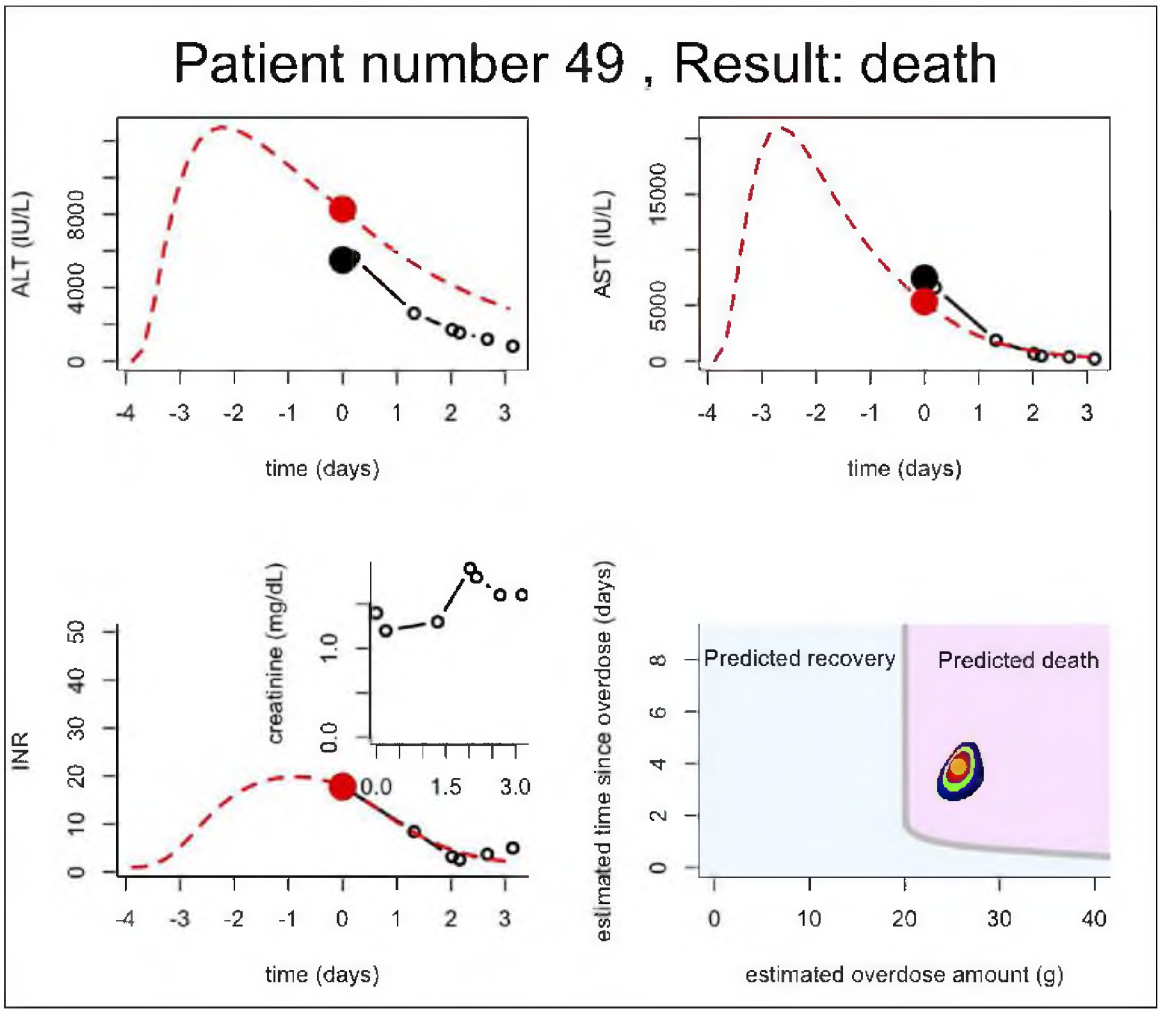

Figure 2.6. Markers of liver damage (small black open circles) and model predictions (red dashed line) based on least squares fits of initial AST, ALT, and INR (large black filled circle) to modeled AST, ALT, and INR (large red filled circle). Time $t = 0$ indicates the time of admission to hospital. The estimated overdose amount and time since overdose for each patient is given by the orange dot in the lower right panel.

3.4 mg/dL increased sensitivity to 88 %. We did not have access to patient encephalopathy or arterial pH.

Using only data available on admission, the model results fit the posttreatment time-series of the markers of liver damage for the majority of individual patients (Tab. 2.2). The results from four representative patients are shown in (Figs. 2.3, 2.4, 2.5, 2.6). Patients 5 and 8 were predicted to have had overdoses that were very close to the lethal threshold, whereas patient 49 was predicted to have exceeded the lethal threshold. Patient 16 was predicted to have had a smaller overdose. The confidence region for some patients who recovered (e.g., patient 16) includes regions with high overdose amount and very early N-Ac administration, as well as regions with low overdose amount and late N-Ac administration. In both cases AST, ALT, and INR are low.

Model predictions of outcome were robust to 50 % increase or decrease in parameter values (Tab. 2.3). The most sensitive model parameters were the fraction of liver required for survival, μ, the amount of AST in the liver, β_S, and the decay rate of AST, δ_S. Increasing μ to 0.45 caused more patients who eventually recovered to be predicted to die, and resulted in 100 % sensitivity and 77 % specificity, whereas decreasing μ to 0.15 resulted in 88 % sensitivity and 93 % specificity. Increasing β_S by 50 % resulted in 100 % sensitivity and 79 % specificity, whereas decreasing β_S by 50 % resulted in 88 % sensitivity and 88 % specificity. Increasing δ_S by 50 % resulted in 100% sensitivity and 91 % specificity, whereas decreasing δ_S by 50 % resulted in 88 % sensitivity and 74 % specificity.

Some parameters such as p, the fraction of APAP oxidized to NAPQI, have a large effect on predicted dose of APAP, but no effect on predicted outcome. If p is 0.025, an overdose amount of 40 g is required for 70 % hepatic necrosis and predicted death, whereas if p is 0.075, an overdose amount of 13.3 g is required for 70 % hepatic necrosis and predicted death. Estimates of overdose amount scale with lethal dose so that estimates of outcome remain the same despite large changes in estimated overdose amount.

2.4 Discussion

APAP, alone or in combination, accounts for about 50 % of cases of ALF in the USA [25]. Survival largely depends on two parameters: the size of the initial dose and time elapsed prior to the administration of N-Ac. Very early administration (up to 12 hours after overdose) of N-Ac results in almost 100 % survival [8].

Table 2.2. Observed AST, ALT, INR, creatinine, and result, and predicted overdose amount A_0, time since overdose τ, predicted result without creatinine, residual, and estimated probability of death. Patients with predicted results marked with a star ($*$) were predicted to die with the inclusion of creatinine.

patient number	AST	ALT	INR	creatinine	result	A_0	τ	predicted result (without creatinine)	residual	probability of death
1	18	27	1.2	0.8	recovery	6.1	3.9	recovery	0.5	0
3	138	128	1.2	0.5	recovery	6.6	1.9	recovery	0.46	0
4	6023	3352	11	1.5	transplant	25.1	4.4	death	3.73	1
5	6432	6390	3	3	recovery	18.9	3.2	recovery	0.23	0.12
6	5267	12202	4.3	0.6	recovery	20.5	3.4	death	0.82	0.44
8	11842	6731	3.9	2.6	recovery	16.3	1.6	recovery	0.46	0.15
9	2381	4960	1.6	0.8	recovery	18.5	4.2	recovery	0.03	0.16
10	26	19	1.1	0.7	recovery	5.8	1.4	recovery	0.13	0
11	1546	3642	1.4	0.7	recovery	17.9	4.6	recovery	0.26	0.18
14	313	402	1.1	0.6	recovery	7.6	2.5	recovery	0.09	0
16	1427	1497	1.2	0.8	recovery	9.6	2.2	recovery	0.1	0
17	29	18	1.1	0.6	recovery	5.8	0.8	recovery	0.13	0
18	17	11	1.3	0.4	recovery	7.1	0.2	recovery	1.04	0
21	14230	6746	10.5	2.7	death	22.2	2.9	death	1.36	0.99
22	52	21	1	0.6	recovery	8.1	0.2	recovery	0.11	0
25	184	48	1	0.7	recovery	17.3	0.1	recovery	0.58	0
26	15953	5598	2	2.8	recovery	40	0.4	recovery	0.46	0
28	28	17	1.1	0.8	recovery	5.8	0.7	recovery	0.13	0
29	10394	8392	3.7	5	death	17.5	2.4	recovery*	0.02	0.14
31	24	16	1.1	0.6	recovery	5.7	1	recovery	0.14	0
33	774	443	1.7	0.7	recovery	7.3	0.8	recovery	3.44	0
36	509	7686	3.3	4	death	25.1	6	death*	2.84	1
37	53	19	1.1	0.5	recovery	9.9	0.1	recovery	0.39	0
38	69	71	1	1	recovery	6.3	2.2	recovery	0	0
39	8122	8134	3.8	0.8	recovery	19	2.9	recovery	0.03	0.17
41	443	3368	1.9	0.8	recovery	24.7	6.6	death	0.01	1

Table 2.2 cont.

patient number	AST	ALT	INR	creatinine	result	A_0	τ	predicted result (without creatinine)	residual	probability of death
43	23	22	1.2	0.7	recovery	5.9	2.3	recovery	0.5	0
44	35	19	1.2	0.7	recovery	6	0.4	recovery	0.5	0
47	23	21	1.2	0.6	recovery	5.9	2.1	recovery	0.5	0
49	7454	5507	17.8	1.4	death	25.7	3.9	death	1.19	1
51	37	27	1.4	0.9	recovery	5.9	1.4	recovery	1.69	0
53	626	563	1.6	0.7	recovery	7.7	1.7	recovery	2.75	0
54	24000	15000	3.1	0.9	recovery	17	1.2	recovery	2.84	0.14
55	289	1884	1.1	0.6	recovery	15.1	5.9	recovery	0.07	0.31
58	21	35	1.2	0.7	recovery	6.2	3.9	recovery	0.5	0
59	5238	3641	17.3	2.8	death	26.4	4.5	death	2.65	1
60	6298	2792	21.1	3.8	death	27.1	4.5	death*	5.3	1
61	230	921	1.7	6.7	transplant	10.5	4.7	recovery*	4.03	0.29
62	744	903	1.5	0.9	recovery	8.6	2.3	recovery	1.89	0
63	8029	6989	2	1	recovery	14.6	2.2	recovery	0.1	0
65	147	117	1.3	0.6	recovery	6.5	1.6	recovery	0.97	0
67	21	9	1.2	1	recovery	13.9	0.1	recovery	0.86	0
68	1621	1404	1.8	5.5	recovery	8.9	1.3	recovery*	3.11	0
71	10810	9218	4.4	2.4	recovery	18.4	2.5	recovery	0	0.23
74	5562	4449	2.2	3.5	death	13.1	1.7	recovery*	0.76	0.05
75	14520	9159	2.3	1.3	recovery	14.4	1.6	recovery	0.85	0.02
77	1545	1228	6.3	1.2	death	26.7	6.3	death	8.26	1
78	7716	5588	2.3	0.7	recovery	13.9	1.8	recovery	0.15	0
79	37	13	1.2	0.8	recovery	15.9	0.1	recovery	0.92	0
81	31	25	1.1	0.7	recovery	5.9	1.7	recovery	0.13	0
82	115	163	1.5	3.1	recovery	6.9	2.7	recovery	2.41	0
83	78	52	1.5	0.7	recovery	6.1	1.2	recovery	2.43	0
84	17161	12147	4.2	3.5	recovery	17.5	1.5	recovery*	0.42	0.23

Table 2.3. A summary of how changes in parameter values affect predictions of outcome.

Modified Parameter	New Value	Specificity	Sensitivity	PPV	NPV
Current Study (With Creatinine)		0.91 (39/43)	1 (8/8)	0.67 (8/12)	1 (39/39)
μ	0.45	0.77 (33/43)	1 (8/8)	0.44 (8/18)	1 (33/33)
μ	0.15	0.93 (40/43)	0.88 (7/8)	0.7 (7/10)	0.98 (40/41)
H_{max}	$2.4 * 10^{11}$	0.93 (40/43)	1 (8/8)	0.73 (8/11)	1 (40/40)
H_{max}	$8 * 10^{10}$	0.91 (39/43)	1 (8/8)	0.67 (8/12)	1 (39/39)
β_F	7.5	0.88 (38/43)	0.88 (7/8)	0.58 (7/12)	0.97 (38/39)
β_F	2.5	0.88 (38/43)	1 (8/8)	0.62 (8/13)	1 (38/38)
η	480	0.91 (39/43)	1 (8/8)	0.67 (8/12)	1 (39/39)
η	160	0.93 (40/43)	1 (8/8)	0.73 (8/11)	1 (40/40)
β_L	127200	0.88 (38/43)	0.88 (7/8)	0.58 (7/12)	0.97 (38/39)
β_L	42400	0.91 (39/43)	1 (8/8)	0.67 (8/12)	1 (39/39)
β_S	$3 * 10^5$	0.79 (34/43)	1 (8/8)	0.47 (8/17)	1 (34/34)
β_S	$1 * 10^5$	0.88 (38/43)	0.88 (7/8)	0.58 (7/12)	0.97 (38/39)
q	0.01005	0.91 (39/43)	1 (8/8)	0.67 (8/12)	1 (39/39)
q	0.00335	0.91 (39/43)	1 (8/8)	0.67 (8/12)	1 (39/39)
δ_L	0.525	0.88 (38/43)	1 (8/8)	0.62 (8/13)	1 (38/38)
δ_L	0.175	0.93 (40/43)	0.88 (7/8)	0.7 (7/10)	0.98 (40/41)
δ_S	1.38	0.91 (39/43)	1 (8/8)	0.67 (8/12)	1 (39/39)
δ_S	0.46	0.74 (32/43)	0.88 (7/8)	0.39 (7/18)	0.97 (32/33)
r	1.5	0.84 (36/43)	1 (8/8)	0.53 (8/15)	1 (36/36)
r	0.5	0.93 (40/43)	1 (8/8)	0.73 (8/11)	1 (40/40)
κ	0.0033	0.91 (39/43)	0.88 (7/8)	0.64 (7/11)	0.98 (39/40)
κ	0.0011	0.93 (40/43)	0.88 (7/8)	0.7 (7/10)	0.98 (40/41)
δ_G	3	0.91 (39/43)	1 (8/8)	0.67 (8/12)	1 (39/39)
δ_G	1	0.91 (39/43)	1 (8/8)	0.67 (8/12)	1 (39/39)
δ_Z	7.5	0.93 (40/43)	1 (8/8)	0.73 (8/11)	1 (40/40)
δ_Z	2.5	0.91 (39/43)	1 (8/8)	0.67 (8/12)	1 (39/39)
γ	$1.5 * 10^7$	0.91 (39/43)	1 (8/8)	0.67 (8/12)	1 (39/39)
γ	$5 * 10^6$	0.91 (39/43)	1 (8/8)	0.67 (8/12)	1 (39/39)
p	0.075	0.91 (39/43)	1 (8/8)	0.67 (8/12)	1 (39/39)
p	0.025	0.91 (39/43)	1 (8/8)	0.67 (8/12)	1 (39/39)
δ_A	0.495	0.91 (39/43)	1 (8/8)	0.67 (8/12)	1 (39/39)
δ_A	0.165	0.91 (39/43)	1 (8/8)	0.67 (8/12)	1 (39/39)
α	9.45	0.91 (39/43)	1 (8/8)	0.67 (8/12)	1 (39/39)
α	3.15	0.91 (39/43)	1 (8/8)	0.67 (8/12)	1 (39/39)
F_{min}	0.85	0.91 (39/43)	1 (8/8)	0.67 (8/12)	1 (39/39)
F_{min}	0.65	0.93 (40/43)	1 (8/8)	0.73 (8/11)	1 (40/40)
θ	2.5	0.86 (37/43)	0.88 (7/8)	0.54 (7/13)	0.97 (37/38)
θ	7.5	0.91 (39/43)	1 (8/8)	0.67 (8/12)	1 (39/39)

Some models of APAP toxicity rely on the time between ingestion and hospital admission to determine the need for treatment [17] or as a measure of exposure [26]. These are risky approaches because the timing of the overdose provided by the patient is frequently unobtainable or unreliable. Moreover, patients who arrive at the hospital 24 hours or more postingestion may have plasma APAP levels below the detection limit.

The KCC [24] provides a well-validated method for predicting death without transplantation in APAP-induced ALF [27], although they have been criticized for low sensitivity [28] and low negative predictive value (NPV) [29]. KCC used an initial dataset of 310 patients to identify statistically significant prognostic indicators to distinguish survivors and nonsurvivors and used a validation set of 121 patients to identify cutoff values associated with survival rates less than 20 % for the statistically significant prognostic indicators, with no physiologically defined model of mortality. Many modifications of the KCC have been suggested [30, 31, 32, 33, 34, 35], perhaps most importantly the addition of arterial lactate [36]. Arterial lactate has consistently been shown to be associated with survival, although its prognostic value has been questioned [37].

In contrast to other modifications of the KCC, MALD is novel because we build upon the KCC by utilizing an understanding of the dynamics of hepatocyte damage following APAP overdose in the form of a dynamic mathematical model. Hepatic necrosis is directly related to the extent of covalent binding of NAPQI to intracellular components [2, 4, 6, 7], which causes hepatocyte lysis and release of AST and ALT into the blood. This produces a characteristic time course of injury with an early rise and predictable decay of AST, ALT, and INR. We have developed a system of differential equations based on the principles of APAP-induced liver damage. All parameters in MALD were estimated from the literature, except six that were adjusted to match general properties of AST and ALT dynamics, and two that were scaled to the dosages thought to cause hepatotoxicity and death. Survival information from University of Utah patients was not used in model development or parameterization. The equations describe how AST, ALT, and INR levels change over time as a function of overdose amount. Because these curves over time are only a function of initial overdose amount, AST, ALT, and INR levels in the model only depend on initial overdose amount and time since overdose. Our method works by fitting measured AST, ALT, and INR values to the curves described by our differential equations to estimate overdose timing and amount (Fig. 2.7). An outcome of death is predicted when the estimate of overdose amount is sufficiently high and the estimate of timing predicts N-Ac to be ineffectual, or

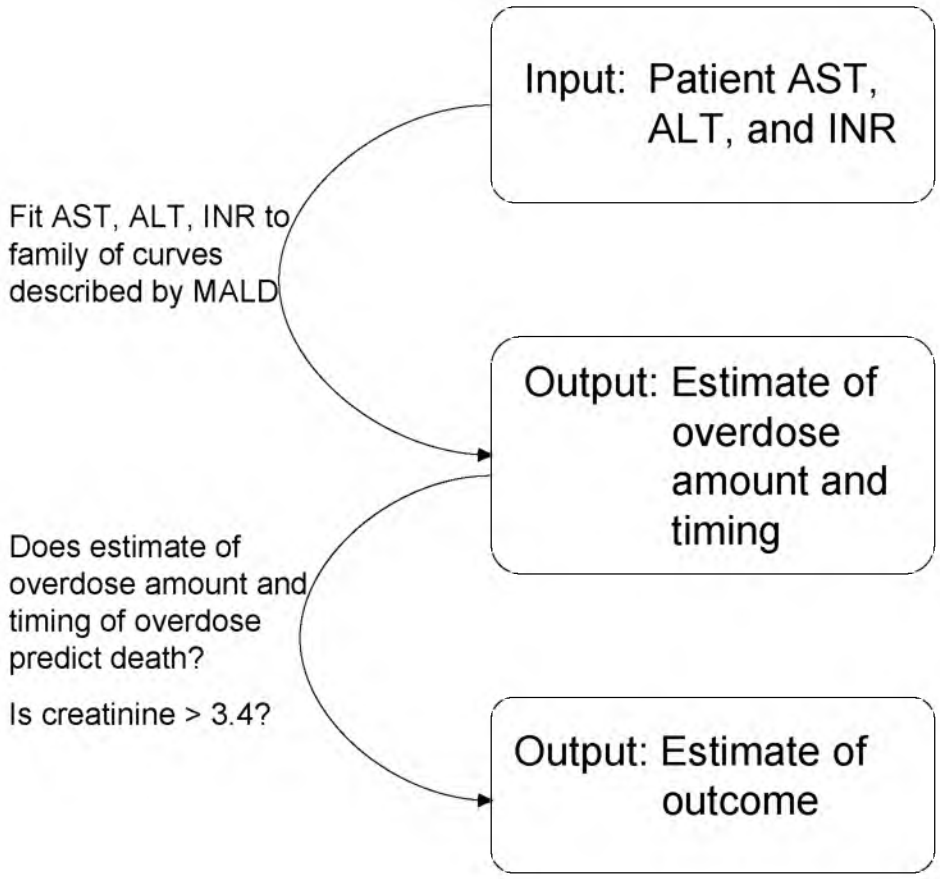

Figure 2.7. A schematic description of how MALD can be used to estimate overdose amount, timing, and outcome. Patients' AST, ALT, and INR are fit to a family of curves described by MALD to estimate overdose amount, timing, and outcome. If outcome is predicted to be poor, liver transplantation may be necessary.

when serum creatinine measurements are sufficiently high. If the outcome is predicted to be poor, liver transplantation may be the only life-saving treatment.

Previous studies have not found absolute aminotransferase levels to be significant predictors of outcome in cases of APAP-induced ALF [24]. This is not surprising because aminotransferase levels will be low, even with a high dose, both early and late in the course of the injury based on known mechanisms of liver damage following APAP overdose. Similarly, high aminotransferase levels may be measured near peak liver damage, even in cases of nonlethal overdose. In conjunction with INR and a suitable mathematical model describing these mechanisms, however, aminotransferase levels do contain sufficient information to estimate the timing and amount of overdose.

Our model cannot distinguish patients with high overdose amounts and early administration of N-Ac from patients with low overdose amounts and delayed treatment because in both cases AST, ALT, and INR levels are low. However, this ambiguity affects only patients who are predicted to recover.

Some patients with unique characteristics, such as those with significant muscle damage, may not fit the model. Muscle damage increases the level of AST, which may lead to poor estimation of liver damage. Because ALT and INR values are not affected by muscle damage, this effect may be minimal. Further studies are warranted to determine whether more refinements are needed for special patient groups.

Our treatment of all patients as having the same parameter values is unrealistic. Well-known covariates of disease severity such as age [38], chronic alcohol use [39, 40], starvation or malnutrition [41], and interactions with other drugs [42, 43, 44] may affect the parameter values of an individual. In some cases these differences will not affect the accuracy of predictions of outcome. Model predictions derive from the amount of unconjugated NAPQI that results from a given dose, but that amount may depend on patient characteristics. For example, alcoholics may make excessive NAPQI because of elevated p-450 levels, or individuals may have decreased levels of GSH because of starvation, competition from other drugs, or genetic variation. These differences might make the model estimates of initial dose seem overly high, but the outcome could still be accurately predicted because these patients have more unconjugated NAPQI than is typical for the overdose amount.

James et al. [45] show that APAP protein adduct levels may be used as specific biomarkers of APAP toxicity. If measurements were routinely available, adducts could easily be added to our model, and might provide additional predictive value. However, the correlation

of protein adducts with AST and their similar kinetics lead us to predict this effect would be small, although their more direct relationship to liver damage might reduce noise and make them a superior predictor.

Gregory et al. [46] found that individuals with overdose amounts greater than 10 g did not have significantly different mortality than those reporting smaller overdoses in patients with eventual hepatic encephalopathy. The authors suggest that this may be due to inaccurate reporting of dosing information by patients with eventual hepatic encephalopathy, or from a plateau effect in APAP overdose amount, such that above a threshold the effect of APAP overdose ceases to be additive. A plateau is built into our model, but at 20 g rather than 10 g. In our model, without treatment, any overdose above 20 g will result in severe hepatic injury, maximal AST, ALT, and INR levels, and poor outcome. Our patient set is quite different because Gregory et al. required eventual hepatic encephalopathy for inclusion, a parameter unknown on admission and associated with poor prognosis [47].

Methods to determine whether to use dangerous and costly interventions, such as transplantation, will ideally be based on clinical data that are readily available at the time of admission. Using only initial measurements of AST, ALT, and INR, we were able to predict the hepatic injury progression and extent of liver damage following APAP overdose. Unlike statistical models to predict outcome, which must build on survivorship data, our mechanistic approach is based on the independently testable assumption that 70 % hepatic necrosis leads to death. Our dynamic model yields a prediction of outcome by estimating the time since overdose and overdose amount from commonly obtained laboratory data on admission. With the inclusion of creatinine, we were able, in this retrospective analysis, to predict survival versus death with 91 % specificity, 100 % sensitivity, 67 % PPV, and 100 % NPV. Our initial analysis suggests that MALD compares favorably to statistical methods, and should be validated in multicenter retrospective and prospective evaluation.

CHAPTER 3

CHRONIC ACETAMINOPHEN USE AND ACUTE LIVER INJURY

3.1 Introduction

Acetaminophen is the most commonly used over the counter drug in the United States with over 40 % of adults reporting consumption in a given month and 23 % reporting weekly use [48]. It is found in at least 600 over the counter products, in pain relievers, fever reducers, cold and alergy medicines, and sleep aids, in tablet, gel tab, caplet and liquid form. From 1993 to 2007 there were over 750,000 emergency department visits in the United States attributable to APAP overdose [49]. While acute liver injury due to acetaminophen overdose was historically the result of a single overdose, often a suicide attempt, increasingly overdoses occur unintentionally, with dosages in excess of drug manufacturer recommendations for a period of several days [50]. Unintentional overdoses are associated with poorer outcome, possibly because they are often recognized only after symptoms have developed [51].

The reason for the increase in accidental overdose is likely multifaceted, but may partially be explained by consumer confusion. Since acetaminophen is found in combination with many other drugs, people may exceed the recommended dosage by accidentally "double dipping," not realizing that acetaminophen is present in multiple drugs, and taking more than intended. Consumers do not always adhere to package or label instructions, a problem that is even more prevalent in patients with limited health literacy [52].

Hepatotoxicity is often associated with short-term fasting, chronic alcohol use, or use of P450-inducing medications [39, 40, 41]. Each of these risk factors increases hepatotoxicity for a given dose by altering NAPQI and/or glutathione dynamics. Short-term fasting lowers glutathione production rate, P450-inducing medications increase the amount of NAPQI produced for a given dose, and chronic alcohol use may either increase the amount of NAPQI produced or compete for GSH, lowering the amount of GSH available to metabolize NAPQI.

We further analyzed the mathematical model developed in Ch. 2 to understand the effect of chronic APAP use on liver injury. The mathematical model developed in Ch. 2

assumed a single overdose, with APAP input only as an intial condition. Predictions of outcome were based on estimates of time since overdose and the size of the APAP initial condition. We extended this model to accomodate chronic acetaminophen use and analyzed model dynamics. We found that there is a threshold in the model with respect to APAP intake and hepatocyte damage. Low intake produces no hepatocyte damage since NAPQI is rapidly bound to GSH and safely eliminated, but if APAP intake produces a quantity of NAPQI large enough to fully deplete GSH reserves, hepatocyte damage ensues acutely. We fit our mathematical model describing single overdose marker dynamics to synthetic markers of liver damage from overdose scenarios involving chronic use. The fits produced estimated time since overdose, overdose amount, and predicted outcome, with predicted outcome based on the minimum value of hepatocytes prior to admission. We found that outcome could be accurately predicted from our synthetic data, even when the overdose occured on a background of chronic use, or as a result of a change in APAP metabolism efficiency.

3.2 Methods

3.2.1 Chronic acetaminophen metabolism and marker dynamics

We developed a model of acetaminophen metabolism and associated liver damage in Ch. 2. The model described below is identical to the model in Ch. 2, but with an APAP intake term in the serum APAP equation, σ, and a small leak term in the NAPQI equation unrelated to GSH metabolism, $\delta_N N$. The small leak in the NAPQI equation was added for mathematical convenience, so that N is bounded as H goes to zero.

APAP
$$\frac{dA}{dt} = \sigma - \frac{\alpha}{H_{max}} AH - \delta_A A$$

NAPQI
$$\frac{dN}{dt} = \frac{qp\alpha}{H_{max}} A - \gamma NG - \delta_N N$$

GSH
$$\frac{dG}{dt} = \kappa - \gamma NG - \delta_G G$$

Functional Hepatocytes
$$\frac{dH}{dt} = rH\left(1 - \frac{H+Z}{H_{max}}\right) - \eta NH$$

Damaged Hepatocytes
$$\frac{dZ}{dt} = \eta NH - \delta_Z Z$$

AST $$\frac{dS}{dt} = \frac{\delta_Z \beta_S}{\theta H_{max}} Z - \delta_S (S - S_{min})$$

ALT $$\frac{dL}{dt} = \frac{\delta_Z \beta_L}{\theta H_{max}} Z - \delta_L (L - L_{min})$$

Clotting Factor $$\frac{dF}{dt} = \beta_F \Big(\frac{H}{H_{max}} - F \Big).$$

In principle the parameters may be time-dependent. We will first consider the time-invariant chronic use case, and later develop time-variant chronic use scenarios, with APAP input, σ, and/or GSH production, κ, changing with time.

3.2.2 Time-invariant chronic use

3.2.2.1 Steady states

Setting the time derivatives to zero, we found the steady states of A, G, Z, S, L, and F in terms of the steady states of H and N to be

$$\begin{aligned}
A^* &= \frac{\sigma H_{max}}{\alpha H^* + \delta_A H_{max}} \\
G^* &= \frac{\kappa}{\gamma N^* + \delta_G} \\
Z^* &= \frac{\eta N^* H^*}{\delta_Z} \\
S^* &= \frac{1}{\delta_S} \left(\frac{\delta_Z \beta_S}{\theta H_{max}} Z^* + \delta_S S_{min} \right) \\
L^* &= \frac{1}{\delta_L} \left(\frac{\delta_Z \beta_L}{\theta H_{max}} Z^* + \delta_L L_{min} \right) \\
F^* &= \frac{H^*}{H_{max}}.
\end{aligned}$$

The steady states of H in terms of the steady states of N are $H^* = 0$ and $H^* = \dfrac{-\delta_z H_{max}(\eta N^* - r)}{r(\delta_Z + \eta N^*)}$. The steady state of N corresponding to $H^* = 0$ is the positive root of the quadratic equation

$$(\delta_N \delta_A H_{max} \gamma) N^2 + (-qp\alpha\sigma\gamma + \gamma\kappa\delta_A H_{max} + \delta_N \delta_A H_{max} \delta_G) N - qp\alpha\sigma\delta_G = 0.$$

The steady states of N corresponding to $H^* = \dfrac{-\delta_z H_{max}(\eta N^* - r)}{r(\delta_Z + \eta N^*)}$ are the roots of the cubic equation $aN^3 + bN^2 + cN + d = 0$, where

$$a = \delta_N H_{max} \alpha \delta_Z \eta\gamma - \delta_N H_{max} \delta_A r \eta\gamma$$

$$
\begin{aligned}
b =& qp\alpha\sigma r\eta\gamma - \gamma\kappa H_{max}\delta_A r\eta - \delta_N H_{max}\alpha\delta_Z r\gamma + \delta_N H_{max}\alpha\delta_Z\eta\delta_G - \delta_N H_{max}\delta_A r\delta_Z\gamma \\
&+ \gamma\kappa H_{max}\alpha\delta_Z\eta - \delta_N H_{max}\delta_Z r\eta\delta_G \\
c =& qp\alpha\sigma r\delta_Z\gamma - \gamma\kappa H_{max}\delta_A r\delta_Z + qp\alpha\sigma r\eta\delta_G - \gamma\kappa H_{max}\alpha\delta_Z r - \delta_N H_{max}\alpha\delta_Z r\delta_G \\
&- \delta_N H_{max}\delta_A r\delta_Z\delta_G \\
d =& qp\alpha\sigma r\delta_Z\delta_G.
\end{aligned}
$$

3.2.2.2 Stability of steady states

Because the markers are not coupled to the intracellular or hepatocyte equations, we need only determine the stability of intracellular and hepatocyte subsystem to determine the stability of the steady states of the full system. Linearizing our system of intracellular and hepatocyte differential equations yields the Jacobian

$$
J = \begin{bmatrix}
-\dfrac{\alpha H}{H_{max}} - \delta_A & 0 & 0 & -\dfrac{\alpha A}{H_{max}} & 0 \\
\dfrac{qp\alpha}{H_{max}} & -\gamma G - \delta_N & -\gamma N & 0 & 0 \\
0 & -\gamma G & -\gamma N - \delta_G & 0 & 0 \\
0 & -\eta H & 0 & r\left(1 - \dfrac{H+Z}{H_{max}}\right) - \dfrac{rH}{H_{max}} - \eta N & -\dfrac{rH}{H_{max}} \\
0 & \eta H & 0 & \eta N & \delta_Z
\end{bmatrix}.
$$

We found the steady states numerically for a range of acetaminophen input σ, using parameter values described in Ch. 2, and $\delta_N = 10^{-4}$. We determined the stability of these steady states by numerically solving for the eigenvalues of J, evaluated at the steady states. We found a bifurcation at approximately $\sigma = 0.34$, when the $H^* = 0$ steady state changes stability, and another at approximately $\sigma = 6.83$, at which point the stable fixed point associated with $H^* \approx 1$ and the unstable fixed point collide and vanish (Fig. 3.1). For σ between approximately 0.34 and 6.83, the unstable fixed point has four eigenvalues with negative real part and one eigenvalue with positive real part.

3.2.2.3 Approximation of bifurcation points

Examining the steady states in the limit as γ goes to infinity gives an approximation to the bifurcation points (Fig. 3.2). The steady state of N corresponding to $H^* = 0$ is the positive root of the quadratic equation

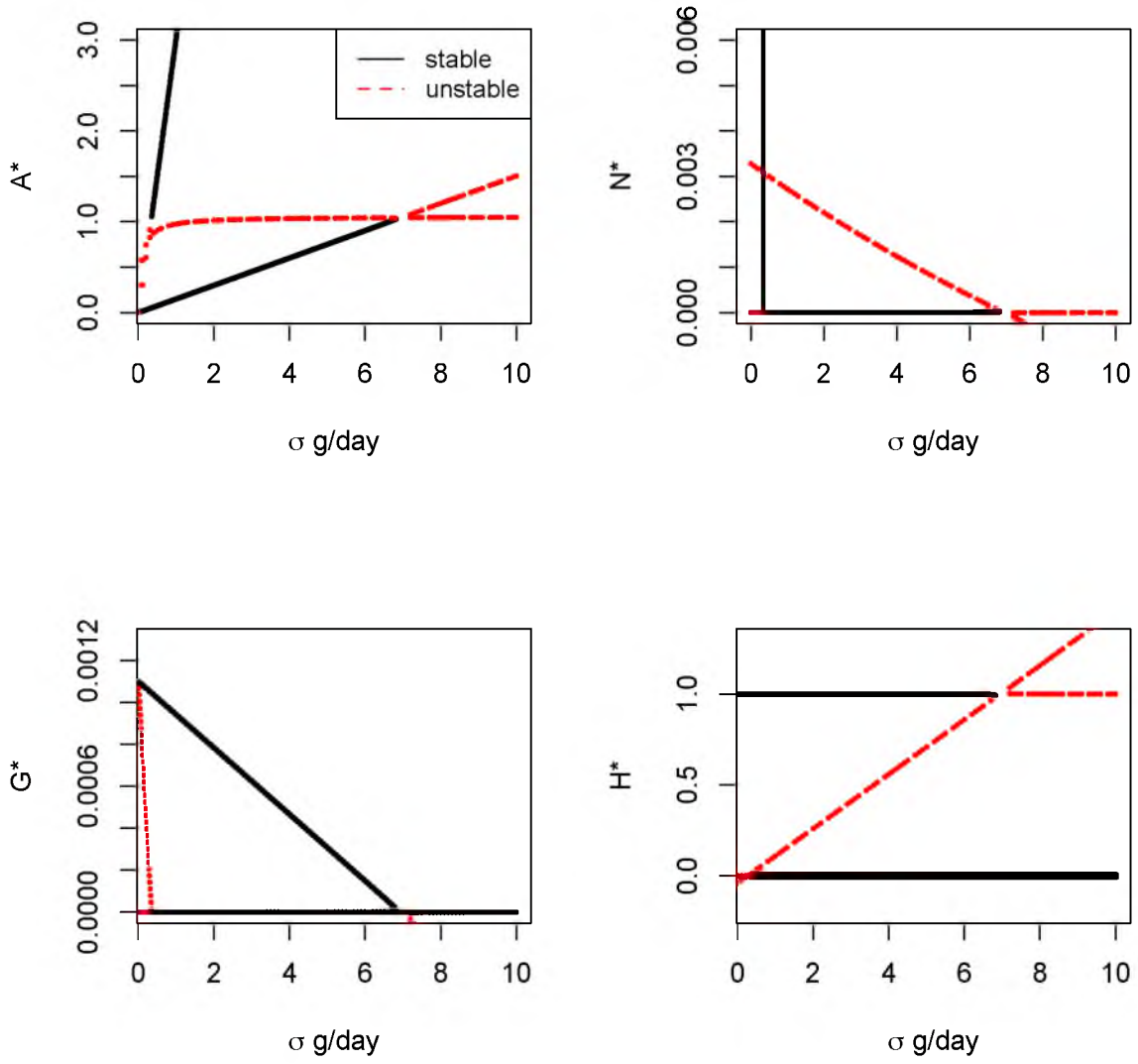

Figure 3.1. Bifurcation diagrams for APAP, NAPQI, GSH, and Hepatocytes as a fraction of normal, as a function of the bifurcation parameter APAP input σ.

$$(\delta_N \delta_A H_{max} \gamma) N^2 + (-qp\alpha\sigma\gamma + \gamma\kappa\delta_A H_{max} + \delta_N \delta_A H_{max} \delta_G) N - qp\alpha\sigma\delta_G = 0.$$

Dividing by γ and taking the limit as γ goes to infinity, the fixed points of the approximate system satisfy

$$N^*(\delta_N \delta_A H_{max} N^* - qp\alpha\sigma + \kappa\delta_A H_{max}) = 0.$$

This equation has degenerate roots when $-qp\alpha\sigma + \kappa\delta_A H_{max} = 0$, which, solving for σ, gives an approximate value for the bifurcation point of $\sigma = \dfrac{\kappa H_{max}\delta_A}{qp\alpha}$.

Similarly, the steady states of N corresponding to $H^* = \dfrac{-\delta_z H_{max}(\eta N^* - r)}{r(\delta_Z + \eta N^*)}$ are the roots of the cubic equation $aN^3 + bN^2 + cN + d = 0$, where

$$\begin{aligned}
a =& \delta_N H_{max}\alpha\delta_Z\eta\gamma - \delta_N H_{max}\delta_A r\eta\gamma \\
b =& qp\alpha\sigma r\eta\gamma - \gamma\kappa H_{max}\delta_A r\eta - \delta_N H_{max}\alpha\delta_Z r\gamma + \delta_N H_{max}\alpha\delta_Z\eta\delta_G - \delta_N H_{max}\delta_A r\delta_Z\gamma \\
& + \gamma\kappa H_{max}\alpha\delta_Z\eta - \delta_N H_{max}\delta_Z r\eta\delta_G \\
c =& qp\alpha\sigma r\delta_Z\gamma - \gamma\kappa H_{max}\delta_A r\delta_Z + qp\alpha\sigma r\eta\delta_G - \gamma\kappa H_{max}\alpha\delta_Z r - \delta_N H_{max}\alpha\delta_Z r\delta_G \\
& - \delta_N H_{max}\delta_A r\delta_Z\delta_G \\
d =& qp\alpha\sigma r\delta_Z\delta_G.
\end{aligned}$$

Dividing by γ and taking the limit as γ goes to infinity, the fixed points of the approximate system satisfy $N(aN^2 + bN + c) = 0$, where

$$\begin{aligned}
a =& \delta_N H_{max}\alpha\delta_Z\eta - \delta_N H_{max}\delta_A r\eta \\
b =& qp\alpha\sigma r\eta - \kappa H_{max}\delta_A r\eta - \delta_N H_{max}\alpha\delta_Z r - \delta_N H_{max}\delta_A r\delta_Z + \kappa H_{max}\alpha\delta_Z\eta \\
c =& qp\alpha\sigma r\delta_Z - \kappa H_{max}\delta_A r\delta_Z - \kappa H_{max}\alpha\delta_Z r
\end{aligned}$$

This equation has degenerate roots when $c = 0$, which, solving for σ, gives an approximate value for the bifurcation point of $\sigma = \dfrac{kH_{max}(\delta_A + \alpha)}{qp\alpha}$.

3.2.3 APAP-induced liver injury on background of chronic use

We explored the effect of chronic use in combination with APAP overdose or change in metabolic efficiency on APAP-induced liver injury. We considered five time-variant scenarios. Three scenarios involved constant chronic APAP use followed by a dose of APAP in the form of a pulse of size A_{over}. The three scenarios we considered were constant chronic APAP use prior to overdose followed by continued constant APAP use, continued constant

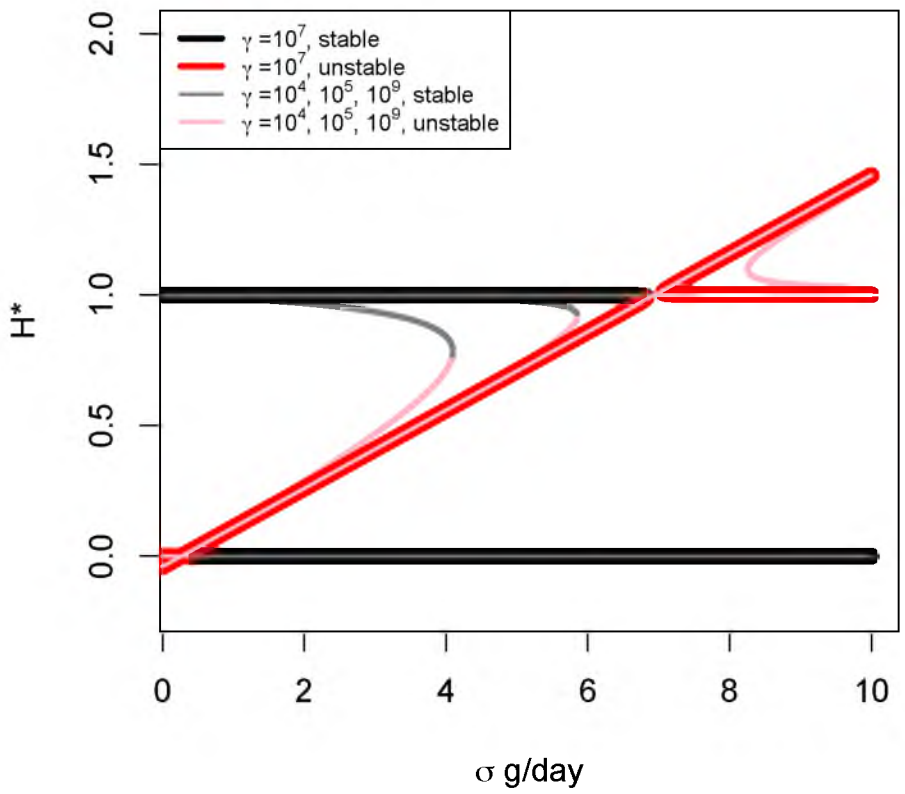

Figure 3.2. Bifurcation diagram for Hepatocytes as a fraction of H_{max} as a function of σ for various values of γ. As γ approaches infinity, the two bifurcation points near $\sigma = 6.9$ converge.

use for 1.5 days followed by no further acetaminophen use, and no further acetaminophen use after overdose (Fig. 3.3). We will refer to these scenarios as σ continued, σ continued for 1.5 days, and σ discontinued, respectively.

We also considered two time-variant scenarios with constant APAP input and lowered GSH production levels for 1.5 days. GSH production can decrease for a variety of reasons including malnutrition or starvation, which may initiate liver damage, even with constant APAP input. The two scenarios we considered were constant chronic APAP input with GSH production decreased to some fraction of normal for 1.5 days with continued constant APAP use, and constant APAP input with GSH production decreased to some fraction of normal for 1.5 days with no further APAP input when GSH production returns to normal

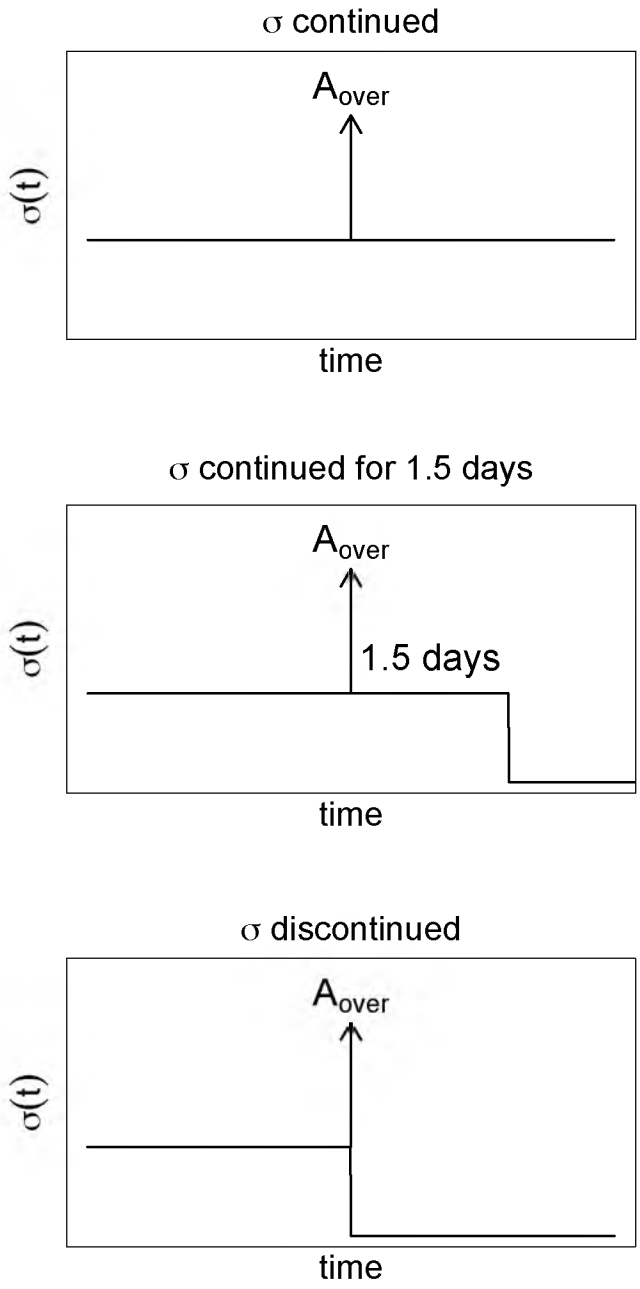

Figure 3.3. A schematic representation of three scenarios of chronic APAP use followed by an APAP overdose of size A_{over}. The scenario σ continued has continued APAP input at a constant rate after A_{over}, σ continued for 1.5 days has continued APAP at a constant rate for 1.5 days after A_{over}, and σ discontinued has no further APAP input after A_{over}.

levels (Fig. 3.4). We will refer to these scenarios as κ changing σ continued, and κ changing σ continued for 1.5 days, respectively.

We numerically solved the differential equations for the five scenarios with time varying parameters for a range of A_{over}, κ as a fraction of normal, and σ. For the three models with constant chronic APAP use followed by an overdose, initial conditions for N, G, H, Z, S, L, and F were set to the stable steady state associated with $H^* \approx H_{max}$ and the given chronic value of σ. The initial condition for A was set to the sum of the A steady state associated with $H^* \approx H_{max}$ and A_{over}. For the two models with constant chronic APAP use followed by lower GSH production, initial conditions for A, N, G, H, Z, S, L, and F were set to the stable steady state associated with $H^* \approx H_{max}$ and the given chonic value of σ.

For each combination of parameters, we tracked AST, ALT, and INR marker levels and the minimum value of H up to a range of times since A_{over} or change in κ. Values of σ ranged from 0 to 6 by 1 g/day, A_{over} ranged from 0 to 30 by 2 g, and κ as a fraction of normal ranged from 0 to 1 by 0.1. The differential equations were numerically solved for each combination of σ and A_{over} for each of the three models involving chronic acetaminophen use followed by overdose and for each combination of σ and κ as a fraction of normal for the two models involving reduced κ for 1.5 days.

The case σ discontinued is approximately equivalent to a single time overdose of a larger amount. Since γ is large, the initial NAPQI produced by the overdose is rapidly absorbed by GSH, until GSH reserves are depleted to zero, and NAPQI does not increase until GSH reserves are fully depleted. Because γ is large, the steady state values of all of the state variables except A and G are approximately equal in the chronic use case and the single time overdose case. With a background of constant chronic use, the amount of APAP absorbed by GSH before GSH levels drop to approximately zero from an overdose is $\frac{H_{max}}{qp\delta_G}\left(\kappa - \frac{qp\alpha\sigma}{H_{max}(\alpha+\delta_A)}\right)$. The level of A for a chronic user before overdose is $\frac{\sigma}{\frac{\alpha}{H_{max}}+\delta_A}$. The equivalence in overdose amount of the σ discontinued model and the single time overdose model is thus

$$A_{over,chronic} = A_{over} - \frac{\sigma}{\frac{\alpha}{H_{max}}+\delta_A} + \frac{H_{max}}{qp\delta_G}\left(\kappa - \frac{qp\alpha\sigma}{H_{max}(\alpha+\delta_A)}\right) - \frac{H_{max}\kappa}{qp\delta_G},$$

where $A_{over,chronic}$ is the overdose amount in the σ discontinued case that is equivalent to a single overdose without chronic use of size A_{over}

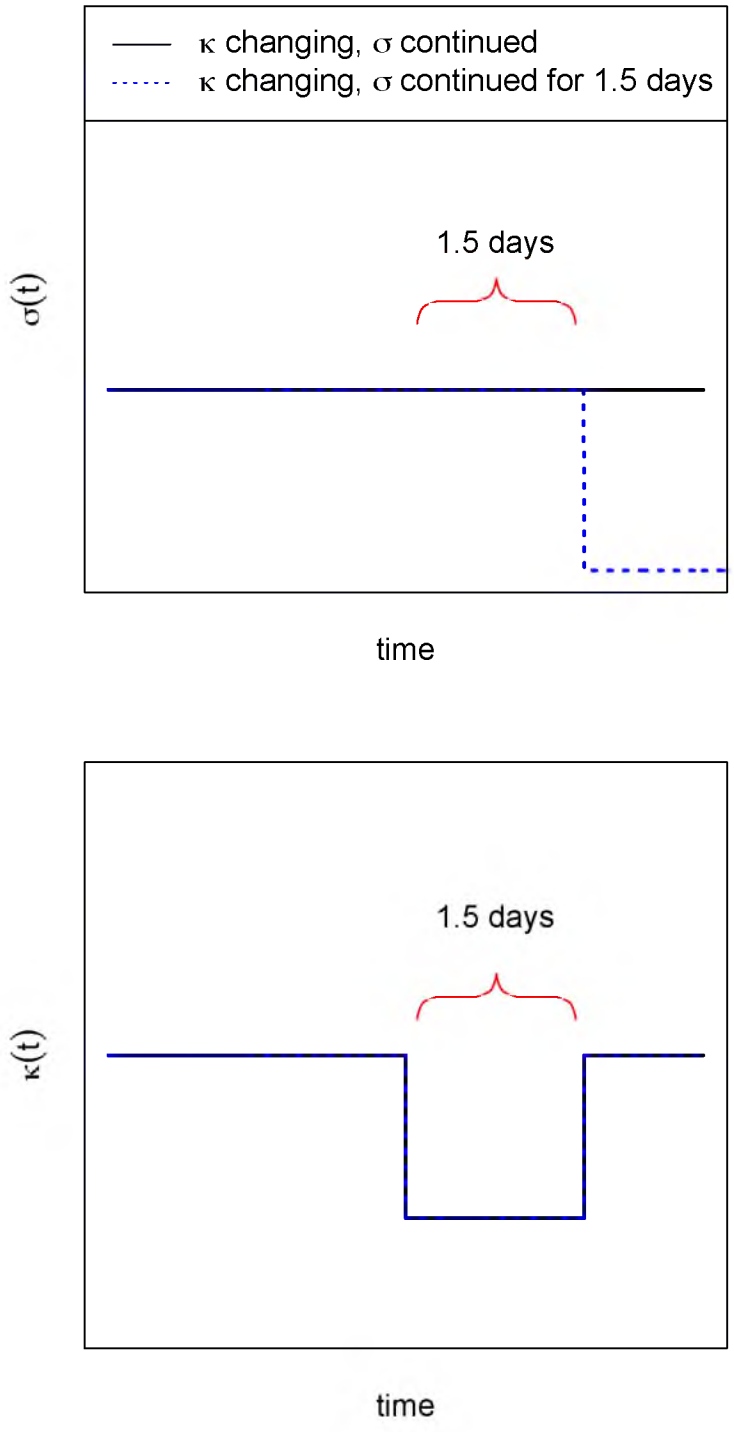

Figure 3.4. A schematic representation of the two scenarios of chronic APAP use followed by decreased GSH production for 1.5 days. The scenario κ changing, σ continued has continued APAP input at a constant rate, while the scenario κ changing, σ continued for 1.5 days has no further APAP input after GSH production returns to normal.

3.2.4 Single overdose fits to chronic model marker dynamics

To determine the ability of our single overdose model to accurately predict outcome from liver injury marker measurements arising from chronic use, we fit the AST, ALT, and INR values from the five scenarios with background chronic acetaminophen use to the single overdose model described in Ch. 2 using weighted least squares at times 1/2, 1, 2, 3, 4, 5, 6, 7 days after the pulse of A_{over} or change in κ, using MALD as described in Ch. 2 (Fig. 3.5). Values of σ ranged from 1 to 6 by 1 g/day, A_{over} ranged from 2 to 30 by 2 g, and κ as a fraction of normal ranged from 0 to 0.9 by 0.1. The model fits estimate an overdose amount and time since overdose for each patient. For each estimated overdose amount and time, we numerically solved the single time overdose model to obtain an estimated pre-admission minimum hepatocyte level and outcome.

3.3 Results

The time-invariant chronic use model has bifurcations with respect to the APAP input parameter σ. There exists a bifurcation at approximately $\sigma_1 = \dfrac{\kappa H_{max}\delta_A}{qp\alpha}$ where the fixed point associated with $H^* = 0$ changes stability and another at approximately $\sigma_2 = \dfrac{kH_{max}(\delta_A + \alpha)}{qp\alpha}$ where the the stable fixed point associated with $H^* \approx H_{max}$ collides with an unstable fixed point and vanishes. In the limit as δ_A goes to zero, all APAP is processed by hepatocytes and the fixed point associated with $H^* = 0$ is stable for all positive σ. The bifurcation at σ_2 corresponds to the ratio of GSH production and NAPQI production. If GSH production is greater than NAPQI production, the fixed point associated with $H^* \approx H_{max}$ is stable, whereas if NAPQI production exceeds GSH production, the only stable fixed point is that associated with $H^* = 0$.

The stability analysis indicates that for σ between σ_1 and σ_2 there exists an unstable fixed point from which a separatrix emanates. The fixed points associated with $H^* = 0$ and $H^* \approx H_{max}$ are stable for σ between σ_1 and σ_2, but a large enough perturbation away from these fixed points can lead to a transition from one fixed point to the other.

A perturbation resulting in transition from the fixed point associated with $H^* \approx H_{max}$ to that associated with $H^* = 0$ can occur for a variety of reasons. We developed five time-variant scenarios, two of which involve continued chronic use after a perturbation in either APAP input, σ, or GSH production, κ. Figs. 3.6 and 3.7 show the APAP pulse and κ deviation for 1.5 days required to force a transition from the fixed point associated with $H^* \approx H_{max}$ to that associated with $H^* = 0$. Also plotted is the APAP pulse and κ

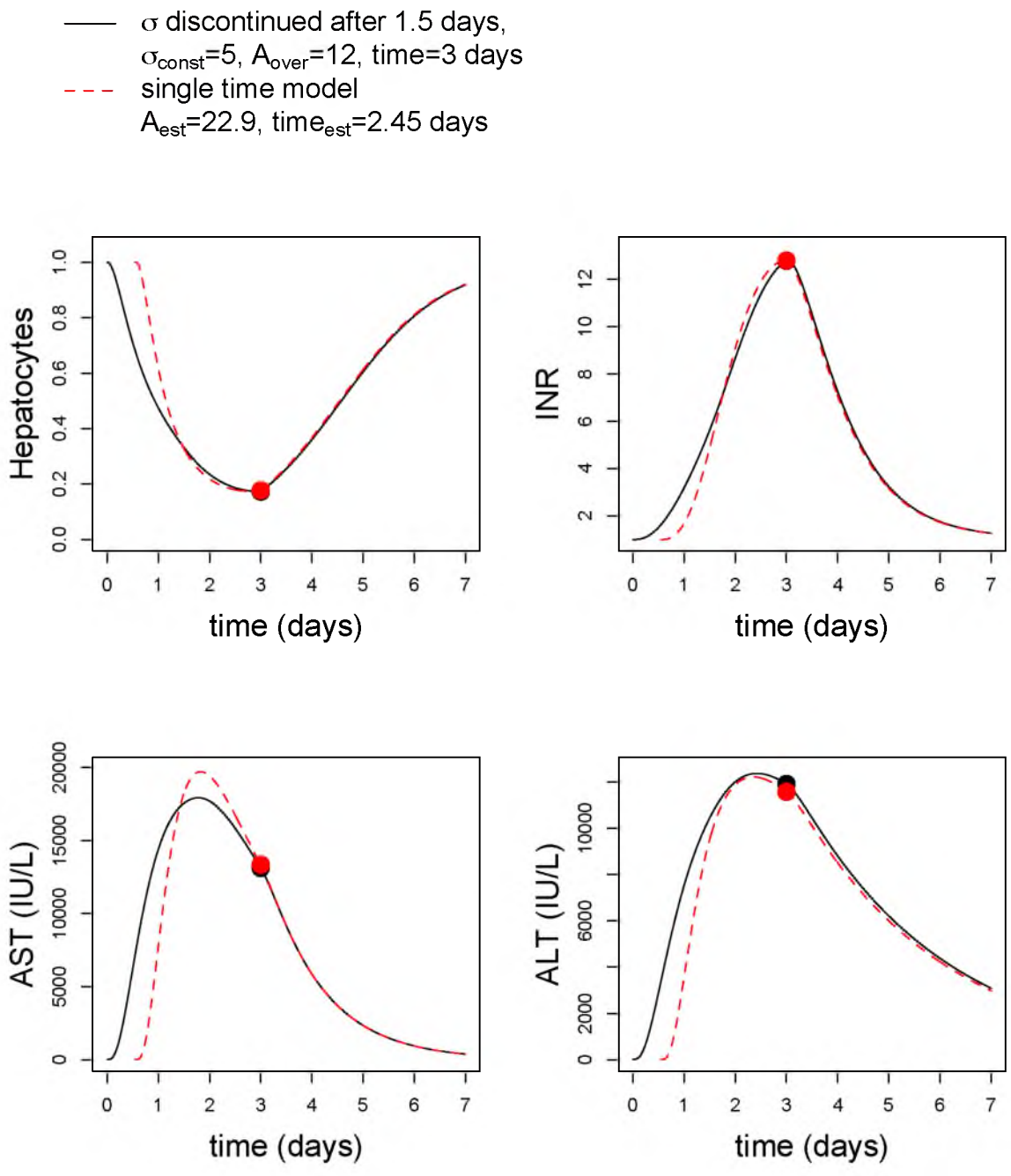

Figure 3.5. An example of marker data from a chronic overdose scenario and the single time overdose fit. The single time overdose model MALD underestimates the time since overdose by about 0.5 days, but estimates the extent of hepatocyte damage well.

deviation for 1.5 days required to reach at least 90 %, 70 %, 50 %, and 30 % necrosis, without treatment, for the three scenarios with APAP use eventually discontinued. Even when APAP use is discontinued immediately following overdose, the damage from an overdose over a background of chronic use is greater than from a typical single time overdose of a given dose because GSH levels are lowered from chronic use.

Figs. 3.8 and 3.9 show the amount of necrosis without treatment for the five time-variant scenarios as a function of APAP pulse, A_{over} (Fig. 3.8) and decreased GSH production for 1.5 days, κ as a fraction of normal (Fig. 3.9). Chronic APAP use increased hepatic necrosis for a given dose. Continued APAP intake leads to more hepatocyte damage than when APAP use is eventually discontinued. APAP intake after damage has already begun to occur results in greater damage than typical for a dose, as there are fewer hepatocytes to process the APAP.

We fit the marker levels from the five chronic use time-variant scenarios at times up to a week after overdose or change in GSH production to MALD, the single time overdose model described in Ch. 2, yielding an estimated time since overdose, overdose amount, and minimum hepatocyte level. We compared the estimated time since overdose to the actual time since APAP pulse or change in GSH production rate (Tab. 3.1) and the the estimated minimum hepatocyte level to the actual minimum hepatocyte level actually produced by the five chronic use time-variant scenarios (Tab. 3.2 and Fig. 3.10).

3.4 Discussion

The antioxidant glutathione is extremely effective at binding to NAPQI, preventing the build up of NAPQI that leads to hepatocyte damage and ultimately, if enough NAPQI is produced, liver failure and death. If GSH production cannot keep pace with NAPQI production, intracellular NAPQI levels rapidly increase and acute liver damage ensues. The fast binding of GSH to NAPQI leads to a threshold system such that the rate of NAPQI production must exceed the rate of GSH production for NAPQI to build up enough to cause liver damage.

The five time variant scenarios fit well to the single overdose model. Time since overdose estimates were best for the σ continued for 1.5 days and the σ discontinued scenarios. Time since overdose was estimated least well for the κ changing, σ continued scenario. In this scenario, it takes time for APAP to build up because of low GSH production, so there is a delay from the timing of decreased GSH production to the onset of liver injury.

Table 3.1. Simple linear regression of estimated time since overdose to actual time since APAP pulse or change in GSH production rate in the time-variant scenarios. Significant differences indicate intercept different from 0 and slope different from 1. $^{***}p < 0.001$; $^{**}p < 0.01$; $^{*}p < 0.050.1$; $^{\cdot}p < 0.1$

scenario	intercept ± s.e.	slope ± s.e.	R^2
σ continued	$0.227 \pm 0.053^{***}$	$0.793 \pm 0.013^{***}$	0.845
σ continued for 1.5 days	$0.060 \pm 0.019^{**}$	$0.930 \pm 0.005^{***}$	0.983
σ discontinued	$0.144 \pm 0.020^{***}$	$0.974 \pm 0.005^{***}$	0.984
κ changing, σ continued	$1.083 \pm 0.071^{***}$	$0.337 \pm 0.017^{***}$	0.453
κ changing, σ discontinued	$0.510 \pm 0.058^{***}$	$0.789 \pm 0.014^{***}$	0.870

Table 3.2. Simple linear regression of estimated minimum value of hepatocytes for the single time point overdose fit to the actual minimum hepatocyte level for the time-variant scenarios. Significant differences indicate intercept different from 0 and slope different from 1. $^{***}p < 0.001$; $^{**}p < 0.01$; $^{*}p < 0.050.1$; $^{\cdot}p < 0.1$

scenario	intercept $\pm$ s.e.	slope $\pm$ s.e.	R^2
σ continued	$0.003 \pm 0.001^{**}$	$0.992 \pm 0.002^{***}$	0.997
σ continued for 1.5 days	0.000 ± 0.001	$0.995 \pm 0.002^{**}$	0.997
σ discontinued	$0.002 \pm 0.001^{\cdot}$	1.002 ± 0.001	0.999
κ changing, σ continued	0.002 ± 0.004	0.994 ± 0.004	0.993
κ changing, σ discontinued	-0.006 ± 0.008	$1.005 \pm 0.008^{***}$	0.970

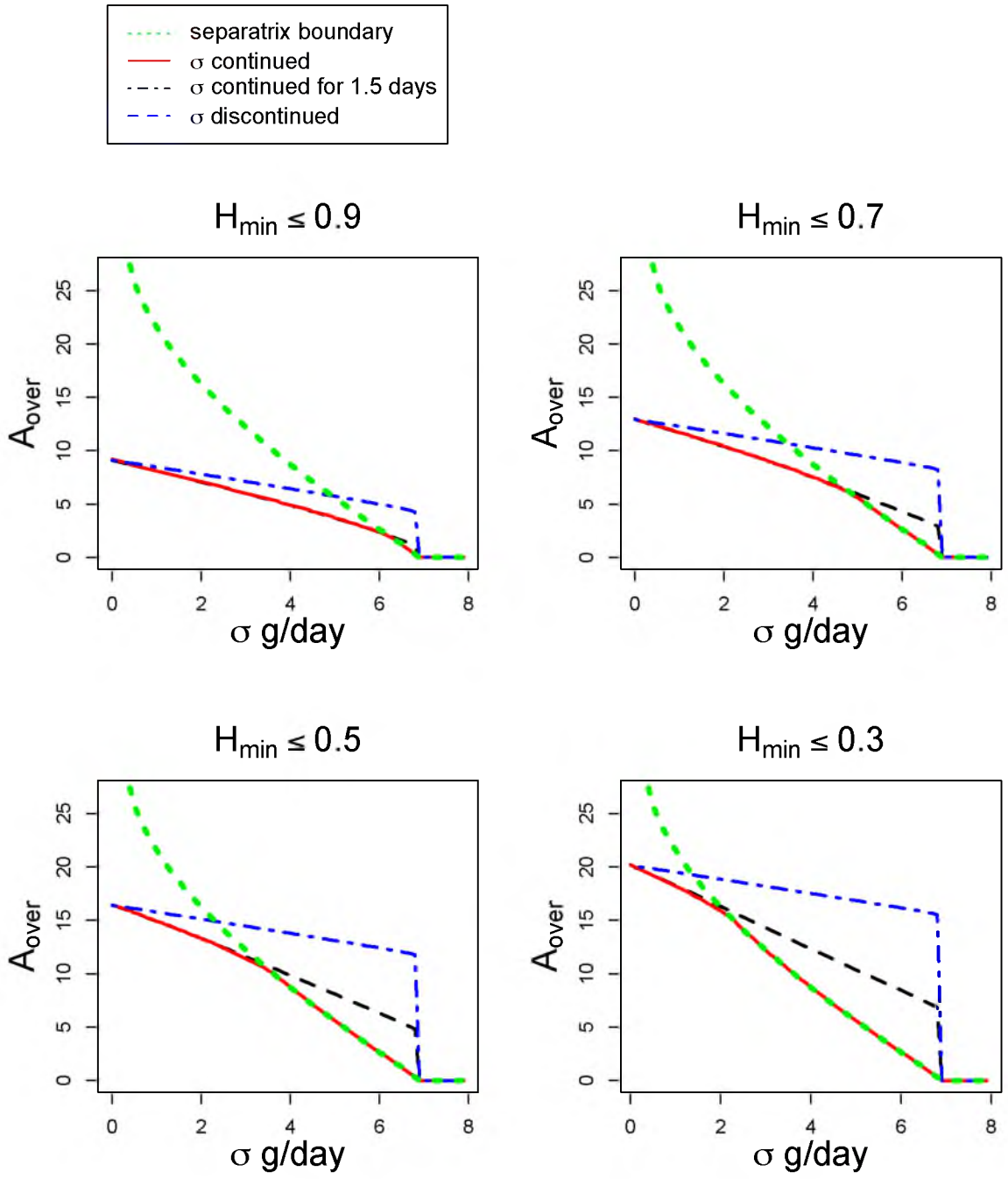

Figure 3.6. The overdose amount, A_{over}, required for minimum hepatocyte level of 0.9, 0.7, 0.5, and 0.3 for a given chronic APAP level σ for three scenarios. The separatrix boundary describes the A_{over} required to transition from the steady state associated with $H^* \approx H_{max}$ to the steady state associated with $H^* = 0$ for the σ continued scenario.

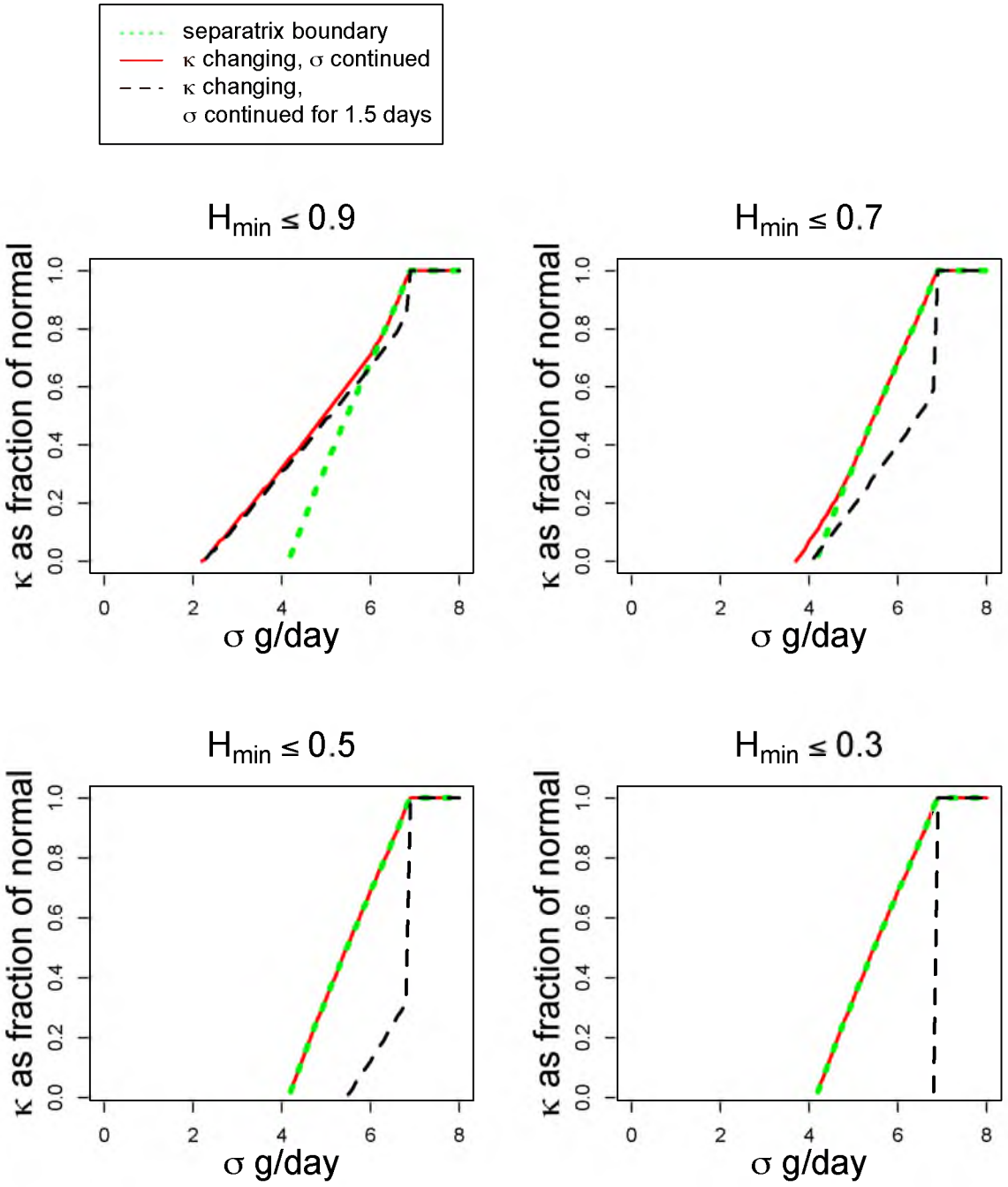

Figure 3.7. The reduction of GSH production, κ as a fraction of normal, required for minimum hepatocyte level of 0.9, 0.7, 0.5, and 0.3 for a chronic APAP level σ for two κ changing scenarios. The separatrix boundary describes the κ as a fraction of normal required to transition from the steady state associated with $H^* \approx H_{max}$ to the steady state associated with $H^* = 0$ for the κ changing, σ continued scenario.

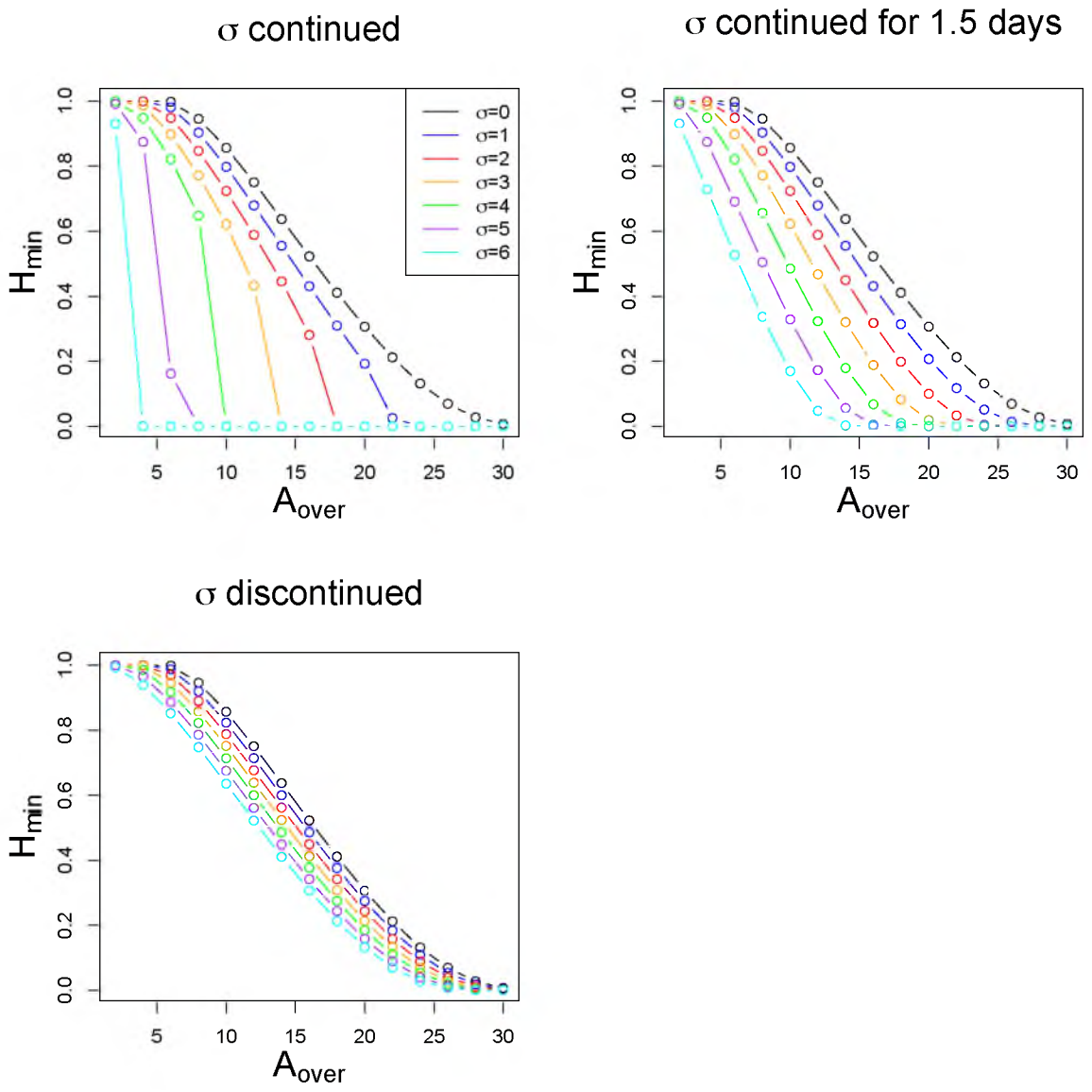

Figure 3.8. The extent of liver damage associated with a pulse overdose of amount A_{over} and a given level of chronic constant APAP input σ for the three scenarios involving chronic input followed by a pulse overdose.

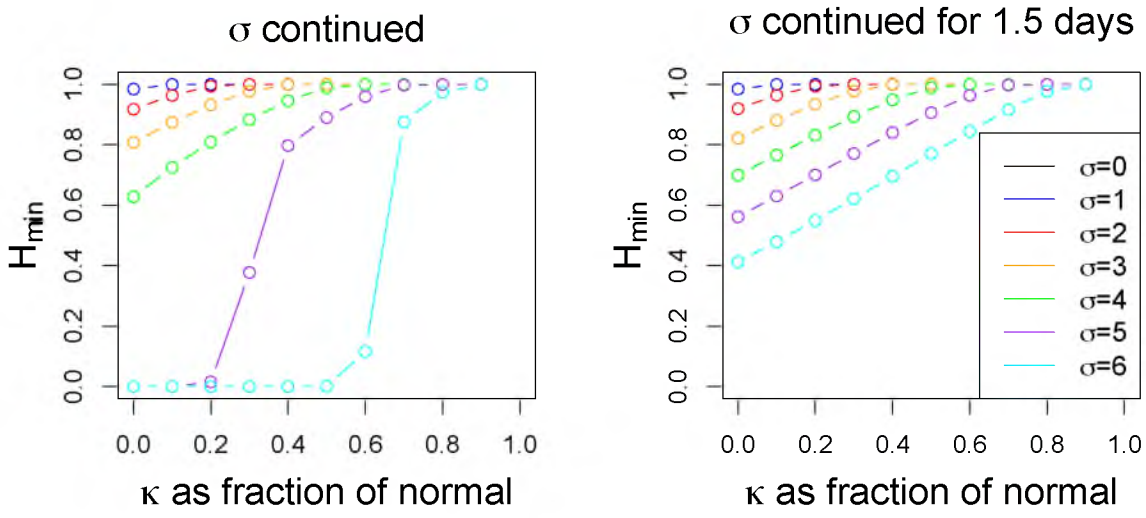

Figure 3.9. The extent of liver damage associated with a given reduction of GSH production, κ as a fraction of normal, and level of chronic constant APAP input, σ, for the two scenarios involving decreased κ.

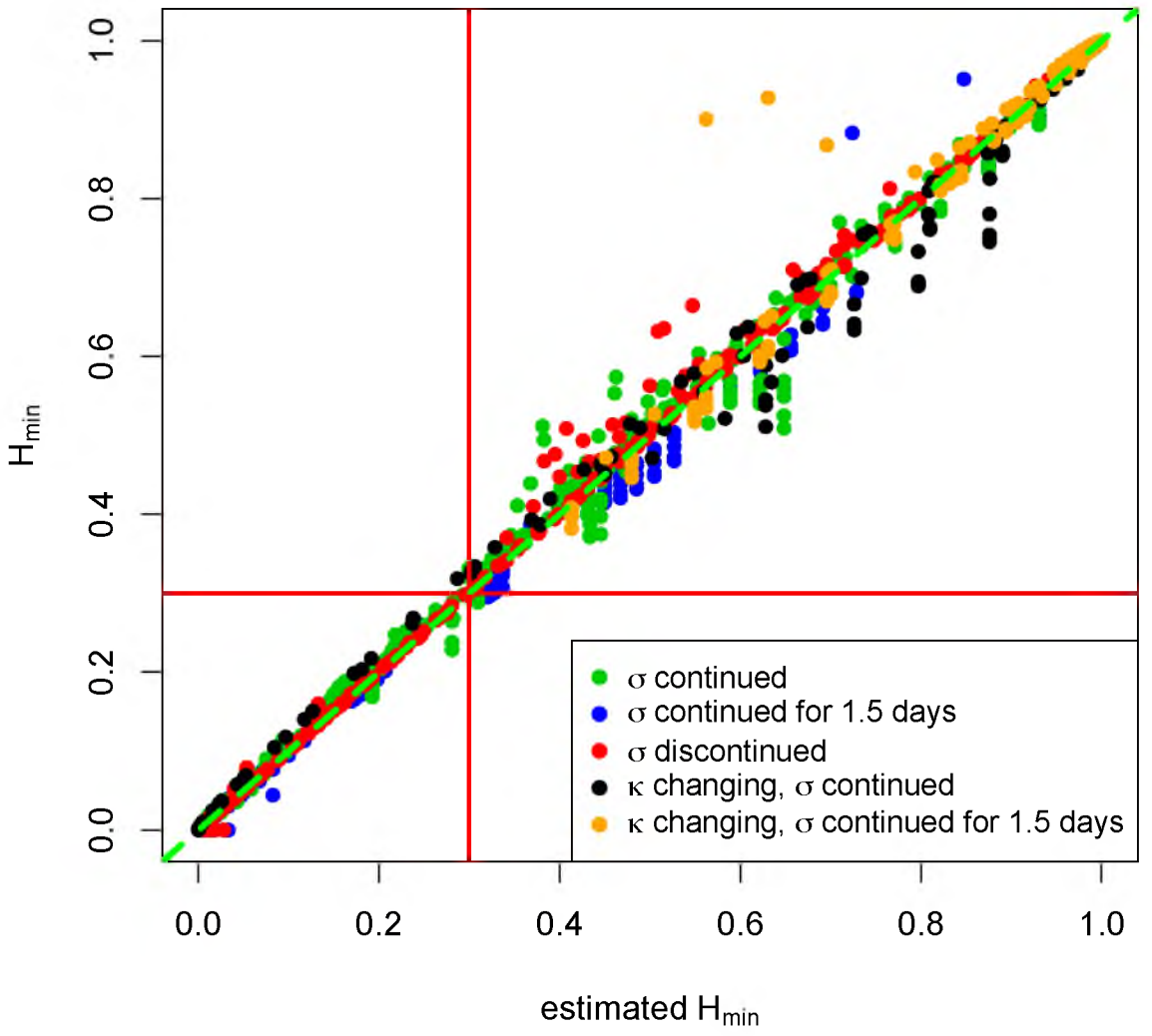

Figure 3.10. Estimated liver damage plotted against actual liver damage for 3120 combinations of time, σ, A_{over}, and κ as a fraction of normal for the five time-varying chronic scenarios.

The extent of hepatocyte necrosis was well estimated for all scenarios, even when time since overdose was poorly estimated ($R^2 > 0.97$ for all scenarios, Fig. 3.10, Tab. 3.2). Estimated intercepts were all very close to zero and slopes very close to one, indicating good fit between estimated liver damage and actual liver damage.

The threshold nature of the system leads to rapid liver injury when NAPQI production exceeds the threshold of GSH production. Either the liver is being injured rapidly, or it is not being injured since it is unlikely for APAP levels to be maintained at a level such that hepatocyte regeneration balances NAPQI production. Thus, APAP-induced liver injury is manifested as acute injury, even when APAP is used chronically. Since APAP-induced liver injury tends to be acute, hepatocyte injury dynamics are similar, even with chronic use.

Similar hepatocyte injury curves create similar marker dynamics. The characteristic time course of liver injury leads to good fits of markers from the five scenarios of chronic APAP use to the single overdose model MALD. Time since overdose is perhaps better thought of as time since initiation of liver injury since in some scenarios there is no single time of overdose. Surprisingly, even when time since onset of injury was poorly estimated, the extent of liver injury was well estimated. Because the extent of liver injury is what is used to predict outcome, predictions of outcome were robust, even when estimates of time since overdose and overdose amount were poor.

We considered five scenarios, though of course many others are possible. Some scenarios such as changing the fraction of APAP metabolized to NAPQI merely change the effective dosage, while others such as competition from other drugs may change model dynamics. The threshold nature of the system combined with the improbability of balance of NAPQI production with hepatocyte regeneration, however, leads us to predict that APAP-induced liver injury is generally acute, and thus predictions of the extent of liver injury are robust. In our model, we assume a constant intracellular GSH production rate. If GSH production is regulated in such a way so as to provide compensation for the lowered GSH levels due to chronic use, model dynamics may be altered and the impact of chronic use lessened.

Risk factors for APAP-induced liver injury can be easily understood in the context of our model. Short-term fasting, chronic alcohol use, and chronic use of P450-inducing medications all affect the model in different ways, but each increases the likelihood of hepatotoxicity for a given dose. Fasting can decrease GSH production, chronic alcohol use may decrease GSH production or increase the fraction of APAP metabolized to NAPQI, and P450-inducing medications increase the fraction of APAP metabolized to NAPQI. These

factors modify the threshold, changing the APAP dosage required for NAPQI production to exceed GSH production.

The dynamics of our APAP overdose model exhibit threshold behavior, giving insight into why chronic APAP use leads to acute, rather than chronic, liver damage. The dynamics suggest that marker fits to MALD, which are based on a single time point overdose, can accurately estimate the degree of hepatotoxicity, even when the overdose occurs on a background of chronic use.

CHAPTER 4

HOW ANIMAL NITROGEN METABOLISM SHAPES ISOTOPIC SIGNATURES OF TROPHIC DYNAMICS

4.1 Introduction

Community ecology relies on a thorough understanding of species interactions. Predator-prey relationships determine energy and nutrient flows, food web structure and dynamics, and mechanism of control of species abundance (e.g., top-down vs. bottom-up). An accurate knowledge of these relationships is needed to predict how these factors change with disturbance and management. In practice, predator-prey relationships are complex, difficult to quantify, and often vary with time, changing with season or year. Direct observation is often impractical or impossible, making indirect methods to estimate and quantify an animal's diet necessary. Stable isotopes are perhaps the most powerful indirect method available. Carbon, nitrogen, and sulfur stable isotopes in nutrients are incorporated into tissues, recording and integrating the isotopic signal of dietary sources [53, 54].

While the stable isotope ratios of diet are the major determinant of the stable isotope ratios of consumer tissue, isotopes do not act as pure tracers. Physiological and metabolic processes lead to the partial separation of light isotopes (e.g., ^{12}C, ^{14}N, etc.) from heavy isotopes (e.g., ^{13}C, ^{15}N, etc.) (Tab. 4.1). The difference between the stable isotope ratio of consumer tissue and diet is termed consumer tissue-diet discrimination. Nitrogen consumer tissue-diet discrimination tends to be positive [55], and the bioaccumulation of ^{15}N can be used to estimate trophic position [56, 57]. The level of nitrogen consumer tissue-diet discrimination is highly variable with interesting feedbacks with diet quality [58, 59] and quantity [60, 61] that depend on physiology and metabolism. It has been suggested that as protein intake increases or protein quality decreases, nitrogen consumer tissue-diet discrimination increases. Other important physiological factors that can influence the nitrogen stable isotope ratio of tissue include nitrogen recycling in the gut [62, 63], tissue turnover [54], and metabolic routing [54, 64], the preferential allocation of certain

Table 4.1. The difference between the nitrogen stable isotope ratios of consumer tissue and diet, termed nitrogen consumer tissue-diet discrimination, is highly variable and influenced by many related, potentially interacting factors that affect an organism's metabolism and nitrogen budget.

Factor	Reference
dietary protein quality	[58, 59]
dietary protein quantity	[60, 61]
total energy intake	[65, 66, 67]
tissue turnover rate	[68]
consumer class and species	[55]
form of nitrogen excretion	[55]
tissue and organ type	[55]
amino acid type	[69]
starvation and nutritional stress	[65, 66, 67]
metabolic rate	[70]
metabolic routing	[64, 54]
gut nitrogen recycling	[71]
pregnancy	[72]
growth	[73]

macronutrients to specific tissues. Because consumer tissue-diet nitrogen discrimination depends on physiology and metabolism, tissue nitrogen stable isotope ratio measurements can be used as a proxy for an animal's metabolic and nutritional state if the physiological underpinnings are well understood.

Consumer tissue-diet nitrogen discrimination also varies with amino acid: certain amino acids have high amino acid-diet nitrogen discrimination, while other amino acids have isotope ratios more similar to diet [69]. This likely depends on the details of how nitrogen is exchanged between amino acids in synthesis and catabolism [61]. Amine groups containing ^{14}N are favored in biochemical reactions that affect nitrogen in amino acids (e.g., transamination and deamination), which may result in preferential excretion of isotopically light nitrogen [74]. Though transamination may be important, isotopic fractionation associated with urea formation is thought to be largely responsible for nitrogen isotope tissue-diet discrimination [75].

We have developed a mathematical model that describes the basic nitrogen dynamics of an animal. Our model tracks nitrogen atoms in ingested molecules as they are transformed, incorporated into tissues, and excreted, and it predicts that a minimum nitrogen intake is required to maintain body protein reserves. We extended our model to track nitrogen

stable isotope and calculated the nitrogen isotope tissue-diet discrimination for a range of nitrogen intake values, as well as the turnover of nitrogen isotopes in various pools after a diet switch.

4.2 Methods

4.2.1 Nitrogen cycling in an animal

The major source of nitrogen in animal tissues is dietary protein. Proteins in diet enter the gut, where they mix with proteins of endogenous origin, mostly shed cells of the mucosal lining, and are broken into constituent small peptides and amino acids. Amino acids in the gut are absorbed via sodium-dependent amino acid transporters into the portal vein where they are processed by the liver and enter the free amino acid pool in plasma [76]. Free amino acids in the blood feed body tissues, which are constantly turning over, and represent the largest store of nitrogen in an animal.

The size of the free amino acid pool in plasma is tightly regulated, as is the size of the protein pool, provided protein intake level exceeds a minimum threshold. Excess plasma nitrogen is processed by the liver and converted to urea, under a net reaction requiring equimolar amounts of glutamate, derived from plasma amino acids, and ammonia, which can be derived from glutamate [75]. Urea is concentrated in the kidneys and excreted, though about 30 % is transported to the gut where bacteria can hydrolize it to ammonia, a process known as urea nitrogen salvage. Gut bacteria also catabolize amino acids to ammonia, as well as synthesize amino acids from ammonia that may become usable to the animal [75]. Nitrogen is also lost in feces as proteins, amino acids, ammonia, and urea, as shed proteins such as skin and hair, and as ammonia and amino acids in urine.

4.2.2 Model description

We developed a system of nonlinear differential equations to describe the major components of nitrogen cycling in an animal (Fig. 4.1).

Gut protein
$$\frac{dG_P}{dt} = \sigma - \gamma_G G_P + \nu_{MP} M_P - \delta_G G_P$$

Gut amino acid
$$\frac{dG_A}{dt} = \gamma_G G_P - \beta_{GL} G_A - \kappa_G G_A + \mu_G G_M - \delta_G G_A$$

Gut ammonia
$$\frac{dG_M}{dt} = \kappa_G G_A - \mu_G G_M + \eta_G G_U - \xi_{GL} G_M + \kappa_I I_P - \delta_G G_M$$

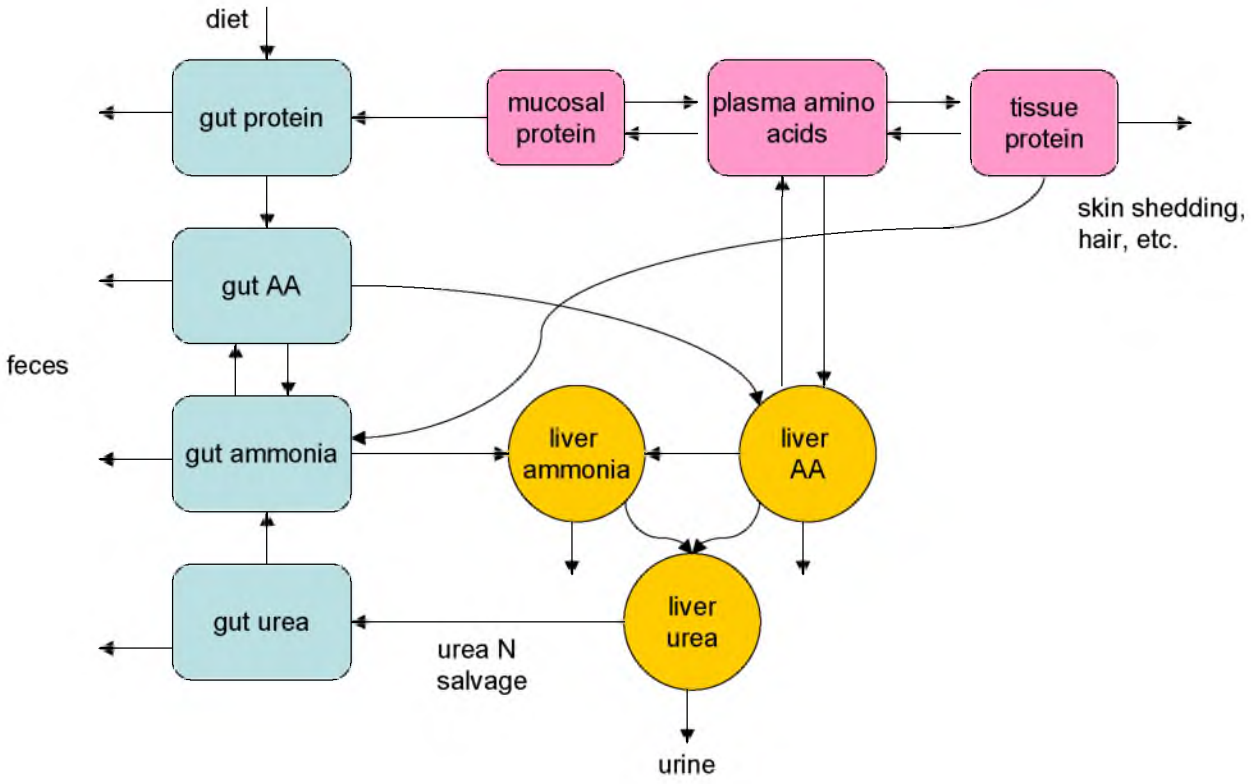

Figure 4.1. A schematic representation of the interactions of nitrogen pools in the mathematical model. Nitrogen atoms in ingested molecules are transformed, incorporated into tissues, and excreted. Nitrogen in the gut (blue) is processed by the liver (yellow) and incorporated into tissues (red).

Mucosal protein
$$\frac{dM_P}{dt} = \gamma_{PM} P_A (m_{pmax} - M_P) - \nu_{MP} M_P - \gamma_{MP} M_P$$

Liver amino acid
$$\frac{dL_A}{dt} = \beta_{GL} G_A - \eta_L L_M L_A - \kappa_L L_A + \beta_{PL} P_A - \beta_{LP} L_A (p_{amax} - P_A) - \delta_A L_A$$

Liver ammonia
$$\frac{dL_M}{dt} = \xi_{GL} G_M + \kappa_L L_A - \eta_L L_M L_A - \delta_M L_M$$

Liver urea
$$\frac{dL_U}{dt} = 2\eta_L L_M L_A - r_{LG} L_U - \delta_L L_U$$

Gut urea
$$\frac{dG_U}{dt} = r_{LG} L_U - \eta_G G_U - \delta_G G_U$$

Plasma amino acid
$$\frac{dP_A}{dt} = \gamma_{MP} M_P - \gamma_{PM} P_A (m_{pmax} - M_P) + \gamma_{IP} I_P - \gamma_{PI} P_A (i_{pmax} - I_P) + \beta_{LP} L_A (p_{amax} - P_A) - \beta_{PL} P_A$$

Intracellular protein
$$\frac{dI_P}{dt} = \gamma_{PI} P_A (i_{pmax} - I_P) - \gamma_{IP} I_P - \kappa_I I_P - \delta_I I_P$$

The nonlinear terms in the model represent the regulation of the size of the plasma amino acid pool, the mucosal protein pool, and the intracellular protein pool, and the formation of urea from liver amino acids and ammonia. We assume that the size of protein pools are well regulated, so that protein pools will tend toward a given level for a wide range of nitrogen intake rates. To achieve this effect, we use mass action like terms to describe the regulation of tissue protein production, mucosal protein production, and transfer of amino acids from the liver to plasma. For example, intracellular protein is produced by plasma amino acid at rate $\gamma_{PI} P_A (i_{pmax} - I_P)$. We use the mass action term $\eta_L L_M L_A$ to describe the formation, within the liver, of urea from ammonia and amino acids.

4.2.3 Model parameterization

We estimated model parameters for a 65 kg human, using known and estimated parameters and steady state pool sizes for an intake rate of nitrogen of 10 g/day (Tabs. 4.2 and 4.3). Using known and assumed parameters and steady state pool sizes for $\sigma = 10$ g/day, we solved the G_P, M_P, and I_P steady state equations for γ_G, γ_{PM}, and γ_{PI}, respectively. Assuming rapid exchange between the plasma amino acid pool and the liver amino acid

Table 4.2. Variables in nitrogen model.

Variable	Description	Steady state with $\sigma = 10$ g N/day	Unit	Reference
G_P	Gut protein nitrogen	10	g ^{14}N	[76]
G_A	Gut amino acid	2.0	g ^{14}N	[76]
G_M	Gut ammonia	0.21	g ^{14}N	[76]
M_P	Mucosal protein	59	g ^{14}N	[76]
L_A	Liver amino acid	1.1	g ^{14}N	assumed
L_M	Liver ammonia	0.98	g ^{14}N	assumed
L_U	Liver urea	1.1	g ^{14}N	assumed
G_U	Gut urea	0.76	g ^{14}N	[76]
P_A	Plasma amino acid	15	g ^{14}N	[77]
I_P	Intracellular body protein	2300	g ^{14}N	[76]

Table 4.3. Parameters in nitrogen model.

Parameter	Description	Value	Unit	Reference
σ	Dietary protein intake rate	0-30	g ^{14}N/day	
ν_{MP}	Shedding rate from mucosal lining to gut	0.17	1/day	[76]
δ_G	Gut nitrogen decay rate	0.1	1/day	[76]
β_{GL}	Absorption rate of amino acids to portal vein	12	1/day	[76]
η_L	Urea production rate	6.5	1/g/day	[78]
δ_A	Rate of amino acid and protein loss in urine	0.65	1/day	[79]
δ_M	Rate of ammonia loss in urine and sweat	0.46	1/day	[79]
r_{LG}	Rate of urea recycling	6.5	1/day	[78]
δ_L	Rate of urea loss in urine	6.5	1/day	[78]
η_G	Rate of urea hydrolysis	9.3	1/day	[78]
γ_{IP}	Rate of turnover of body protein	0.017	1/day	[80]
γ_{MP}	Rate of turnover of body protein	0.017	1/day	[80]
m_{pmax}	Maximum mucosal protein pool size	59.01	g ^{14}N	[76]
i_{pmax}	Maximum body protein pool size	2300.01	g ^{14}N	[76]
p_{amax}	Maximum plasma amino acid pool size	16	g ^{14}N	[76]
δ_I	Rate of shedding of skin and hair	0.00015	1/day	[81]
κ_I	Rate of ammonia production by body protein	0.001	1/day	assumed
γ_G	Degradation rate of protein to amino acid	1	1/day	calculated
γ_{PI}	Intracellular body protein production rate	278	1/ g ^{14}N/day	calculated
γ_{PM}	Mucosal protein production rate	74	1/ g ^{14}N/day	calculated
ξ_{GL}	Rate of ammonia transfer from gut to liver	18	1/day	calculated
κ_L	Rate of liver AA conversion to ammonia	3.4	1/day	calculated
β_{PL}	Plasma AA to liver AA transfer rate	100	1/day	assumed
β_{LP}	Liver AA to plasma AA transfer rate	1513	1/ g ^{14}N/day	calculated
κ_G	Rate of microbial ammonia production in gut	1	1/day	assumed
μ_G	Rate of microbial AA production in gut	36	1/day	calculated

pool, we set $\beta_{PL} = 100$, and solved the P_A steady state equation for β_{LP}. Similarly, we set $\kappa_G = 1$, and solved the G_A steady state equation for μ_G. Using these values, we solved the L_M steady state equation for κ_L, and the G_M steady state equation for ξ_{GL}.

4.2.4 Steady states

We numerically found the steady states as a function of dietary nitrogen intake σ by solving the differential equations at time 10^6 days. Parameters were set to the values in Tab. 4.3 and initial conditions were set to the the steady state values for intake rate of 10 g/day (Fig. 4.2).

4.2.5 Stable isotope model

We developed equations tracking total nitrogen fluxes. The corresponding ^{15}N differential equations, with the potential for fractionation, or preference of molecules containing either ^{15}N or ^{14}N, in each flux term are:

Gut protein ^{15}N
$$\frac{dG_P^*}{dt} = \alpha_{in} R_{in} \sigma - \alpha_{\gamma_G} \gamma_G G_P^* + \alpha_{\nu_{MP}} \nu_{MP} M_P^* - \alpha_{\delta_G} \delta_G G_P^*$$

Gut amino acid ^{15}N
$$\frac{dG_A^*}{dt} = \alpha_{\gamma_G} \gamma_G G_P^* - \alpha_{\beta_{GL}} \beta_{GL} G_A^* - \alpha_{\kappa_G} \kappa_G G_A^* + \alpha_{\mu_G} \mu_G G_M^* - \alpha_{\delta_G} \delta_G G_A^*$$

Gut ammonia ^{15}N
$$\frac{dG_M^*}{dt} = \alpha_{\kappa_G} \kappa_G G_A^* - \alpha_{\mu_G} \mu_G G_M^* + \alpha_{\eta_G} \eta_G G_U^* - \alpha_{\xi_{GL}} \xi_{GL} G_M^* + \alpha_{\kappa_I} \kappa_I I_P^* - \alpha_{\delta_G} \delta_G G_M^*$$

Mucosal protein ^{15}N
$$\frac{dM_P^*}{dt} = \alpha_{\gamma_{PM}} \gamma_{PM} P_A^* (m_{pmax} - M_P) - \alpha_{\nu_{MP}} \nu_{MP} M_P^* - \alpha_{\gamma_{MP}} \gamma_{MP} M_P^*$$

Liver amino acid ^{15}N
$$\frac{dL_A^*}{dt} = \alpha_{\beta_{GL}} \beta_{GL} G_A^* - \alpha_{\eta_{L2}} \eta_L L_M L_A^* - \alpha_{\kappa_L} \kappa_L L_A^* + \alpha_{\beta_{PL}} \beta_{PL} P_A^* - \alpha_{\beta_{LP}} \beta_{LP} L_A^* (p_{amax} - P_A) - \alpha_{\delta_A} \delta_A L_A^*$$

Liver ammonia ^{15}N
$$\frac{dL_M^*}{dt} = \alpha_{\xi_{GL}} \xi_{GL} G_M^* + \alpha_{\kappa_L} \kappa_L L_A^* - \alpha_{\eta_{L1}} \eta_L L_M^* L_A - \alpha_{\delta_M} \delta_M L_M^*$$

Liver urea ^{15}N
$$\frac{dL_U^*}{dt} = \alpha_{\eta_{L1}} \eta_L L_M^* L_A + \alpha_{\eta_{L2}} \eta_L L_M L_A^* - \alpha_{r_{LG}} r_{LG} L_U^* - \alpha_{\delta_L} \delta_L L_U^*$$

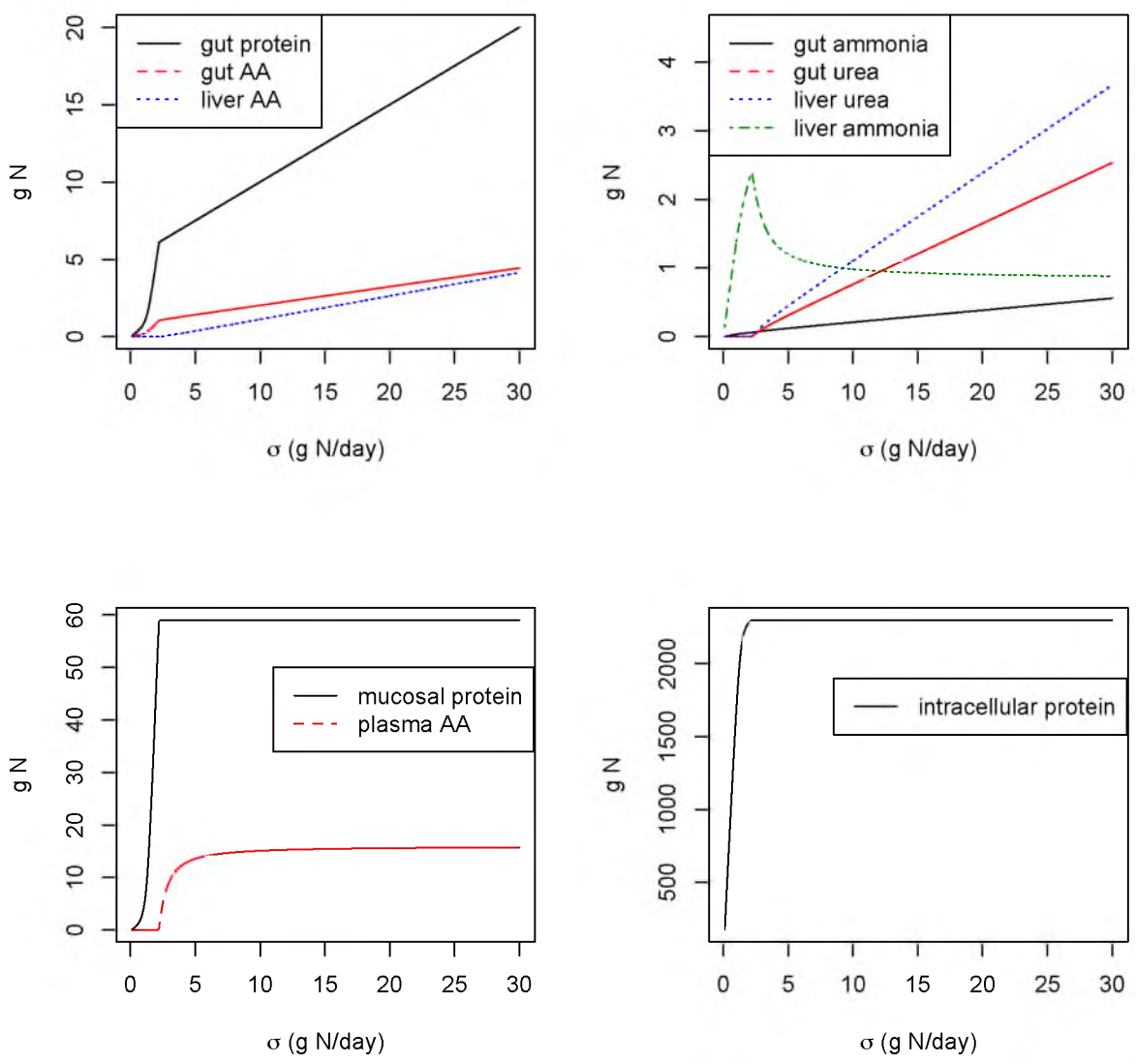

Figure 4.2. Steady state values of state variables as a function of dietary nitrogen input σ.

Gut urea ^{15}N
$$\frac{dG_U^*}{dt} = \alpha_{r_{LG}} r_{LG} L_U^* - \alpha_{\eta_G} \eta_G G_U^* - \alpha_{\delta_G} \delta_G G_U^*$$

Plasma amino acid ^{15}N
$$\begin{aligned}\frac{dP_A^*}{dt} = {} & \alpha_{\gamma_{MP}} \gamma_{MP} M_P^* - \alpha_{\gamma_{PM}} \gamma_{PM} P_A^* (m_{pmax} - M_P) \\ & + \alpha_{\gamma_{IP}} \gamma_{IP} I_P^* - \alpha_{\gamma_{PI}} \gamma_{PI} P_A^* (i_{pmax} - I_P) \\ & + \alpha_{\beta_{LP}} \beta_{LP} L_A^* (p_{amax} - P_A) - \alpha_{\beta_{PL}} \beta_{PL} P_A^*\end{aligned}$$

Intracellular protein ^{15}N
$$\begin{aligned}\frac{dI_P^*}{dt} = {} & \alpha_{\gamma_{PI}} \gamma_{PI} P_A^* (i_{pmax} - I_P) - \alpha_{\gamma_{IP}} \gamma_{IP} I_P^* - \alpha_{\kappa_I} \kappa_I I_P^* \\ & - \alpha_{\delta_I} \delta_I I_P^*.\end{aligned}$$

4.2.6 Stable isotope steady states as function of fractionation

In principle, isotopic fractionation may occur with each term. It is likely, however, that fractionation is dominated by a small number of processes. Since urine has a lower isotope ratio than diet, it is thought that the process leading to isotopic discrimination is urea formation [75].

We set all fractionation factors α in the ^{15}N differential equations to 1, except the fractionation factors associated with urea formation, $\alpha_{\eta_{L1}}$ and $\alpha_{\eta_{L2}}$, which we set equal to each other at a value now referred to as α. We numerically found the ^{15}N steady states for $\alpha = 1$, 0.996, 0.992, and 0.988 as a function of dietary nitrogen intake σ with the isotope ratio of diet $R_{in} = 0.003676$ (Fig. 4.3).

Stable isotope abundances are reported in δ notation as parts per thousands (‰), where

$$\delta = \left(\frac{R_A}{R_S} - 1 \right) * 1000 \text{ ‰}$$

and R_A and R_S are the molar ratios of the rare to abundant isotope in the sample and the standard, respectively. For nitrogen isotopes, the standard is air with a nitrogen isotope ratio of $R_S = 0.003676$.

4.2.7 Turnover from change in diet isotope composition

To assess how changes in the isotope ratio of diet propagate to internal pools, we varied R_{in} with time and numerically solved the differential equations (Figs. 4.4 and 4.5). We simulated a diet switch by setting R_{in} to be a step function equal to 0.003676, corresponding to $\delta^{15}\text{N}_{diet} = 0$ ‰, until day 100, when R_{in} switches to 0.00369438, corresponding to

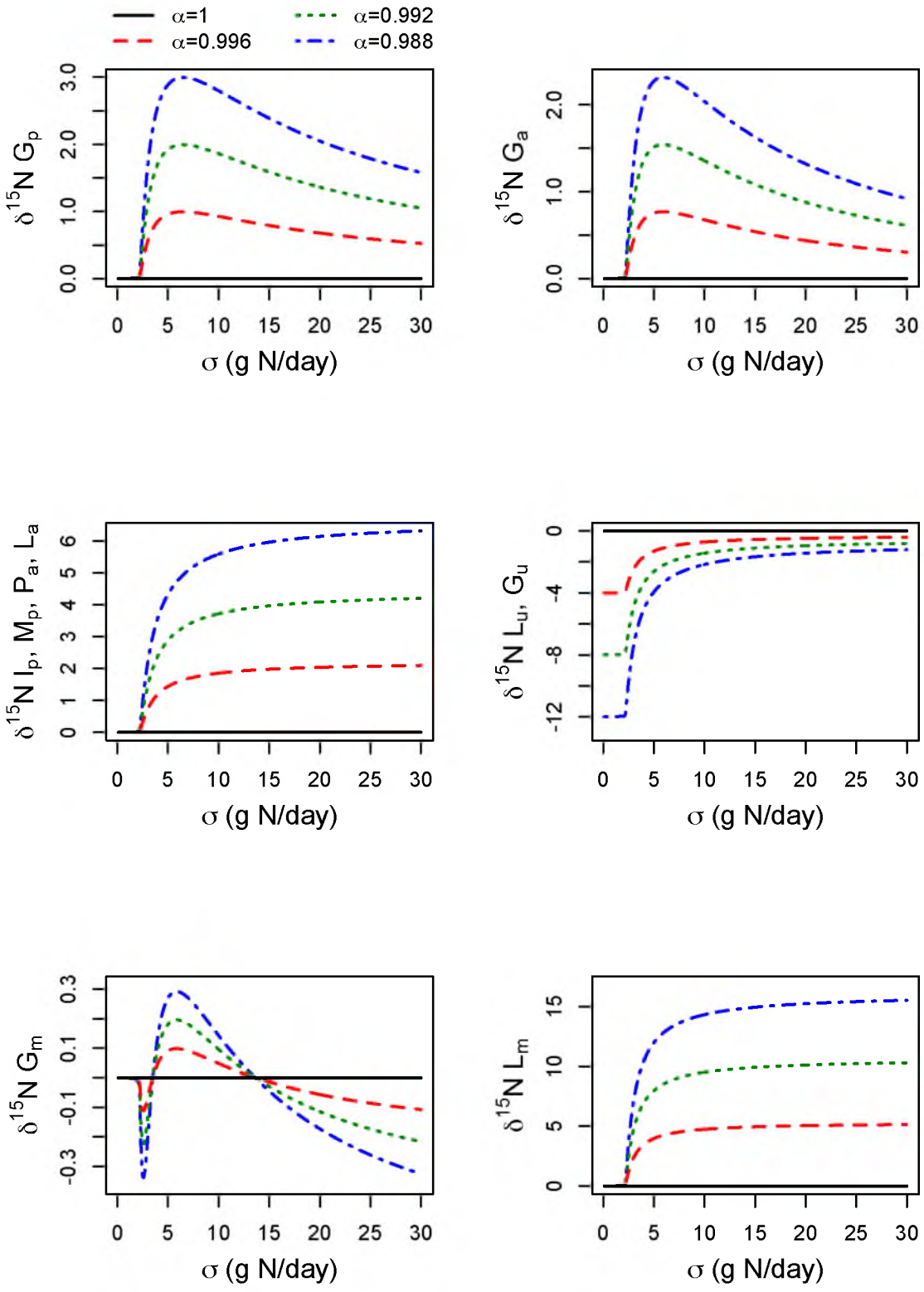

Figure 4.3. Nitrogen stable isotope ratios of the 10 pools at steady state as a function of dietary nitrogen intake, σ, and urea formation fractionation factor, α.

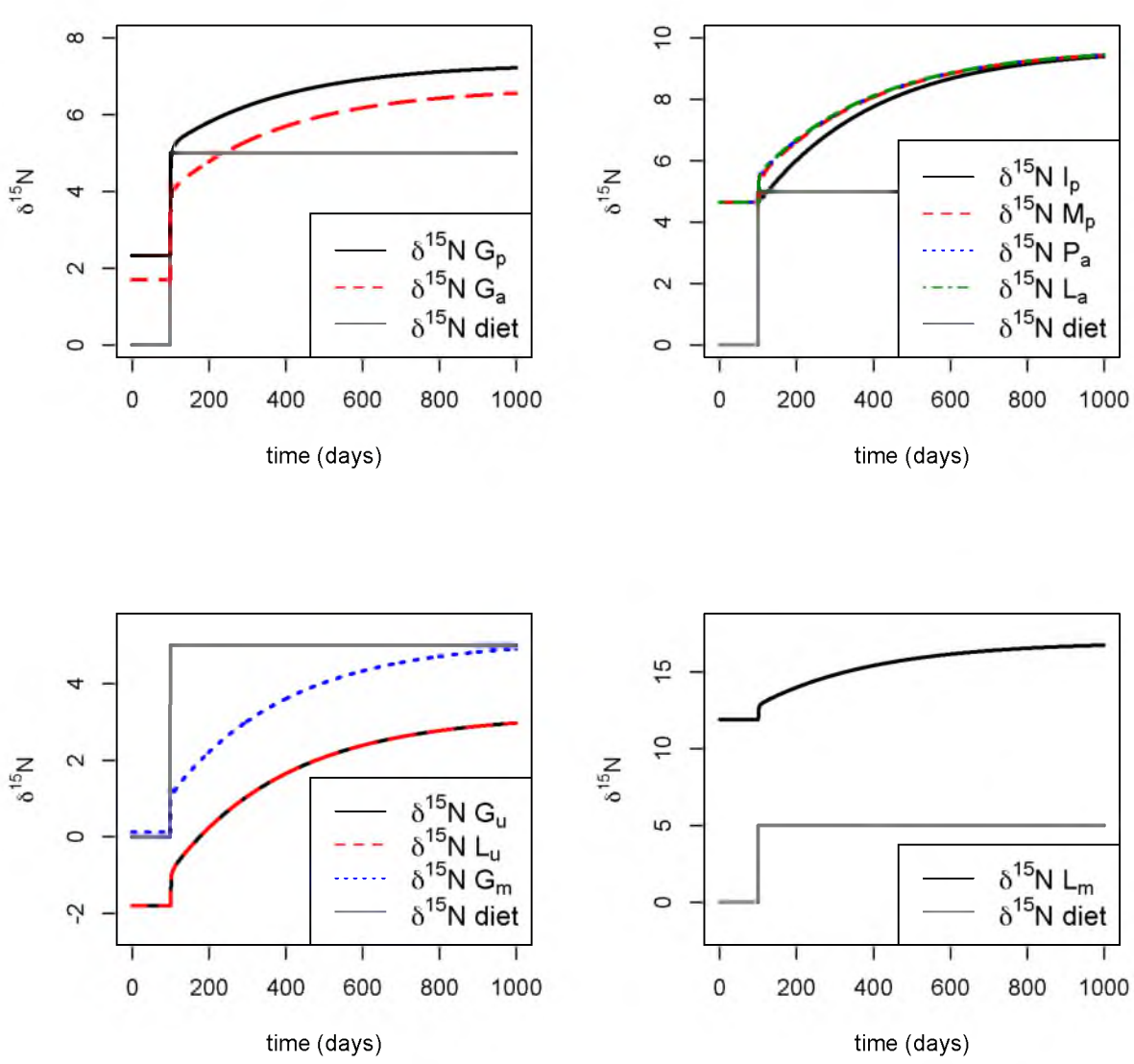

Figure 4.4. Stable nitrogen isotope ratios of the 10 pools and diet as a function of time for $\alpha = 0.990$ and $\sigma = 10$ g/day. The δ^{15}N of diet switches from 0 ‰ to 5 ‰ at day 100.

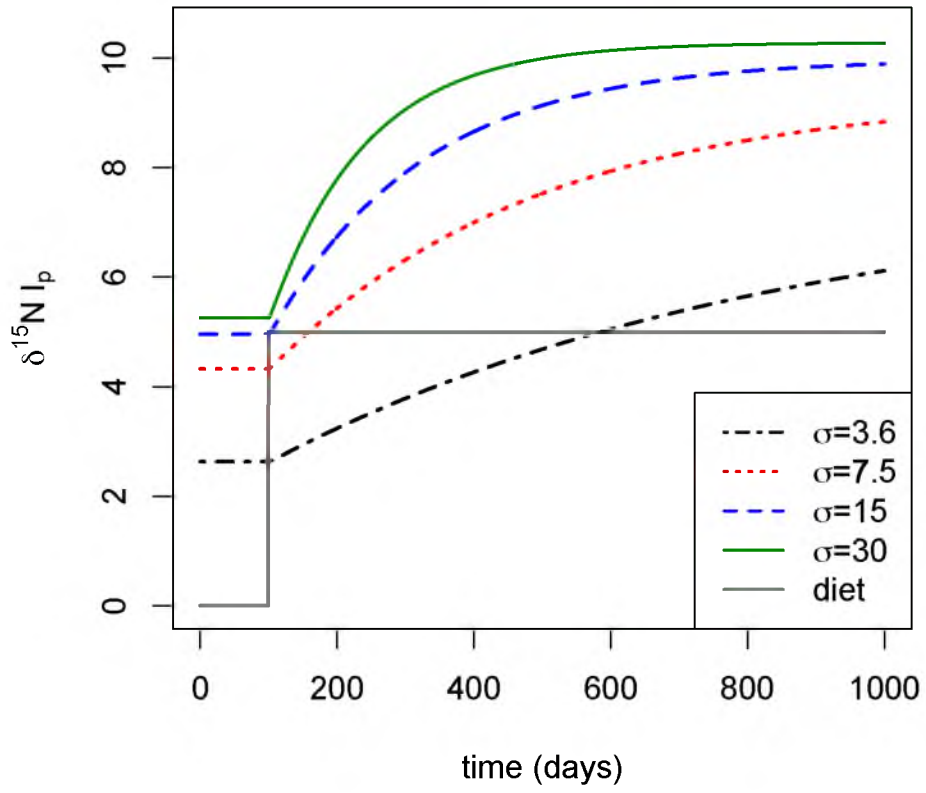

Figure 4.5. Stable nitrogen isotope ratio of intracellular protein as a function of time for $\alpha = 0.990$ and $\sigma = 3.6$, 7.5, 15, and 30. The δ^{15}N of diet switches from 0 ‰ to 5 ‰ at day 100.

$\delta^{15}N_{diet} = 5$ ‰. The total nitrogen dietary intake, σ, was fixed at 3.6, 7.5, 10, 15, or 30 g/day.

4.3 Results

In our model, a minimum dietary nitrogen intake is necessary to maintain plasma amino acid and intracellular protein levels (Fig. 4.2). Consistent with Steffee et al. [82], the steady state levels of plasma amino acids, intracellular protein, and mucosal protein are well regulated, and remain approximately constant with dietary nitrogen intake level, σ, provided σ is greater than about 2.2 g/day. There is almost no urea production for $\sigma < 2.2$ g/day, and for $\sigma > 2.2$ g/day urea production increases linearly with σ. The steady state levels of gut protein, gut amino acid, liver urea, gut urea, and liver ammonia all also increase linearly with σ for $\sigma > 2.2$ g/day.

We extended our nitrogen budget model to account for stable isotope fractionation in urea formation. With isotope fractionation occuring only at urea formation, our model predicts that urea is isotopically depleted relative to diet that body protein is isotopically enriched relative to diet at steady state (Fig. 4.3). The degree of enrichment or depletion of the pools depends on both the fractionation factor associated with urea formation, α, as well as the dietary protein intake rate, σ. For $\sigma < 2.2$ g/day, almost no urea is produced and the $\delta^{15}N$ of body protein is close to that of diet. As σ increases, the $\delta^{15}N$ of the body protein pool increases. The $\delta^{15}N$ of body protein does not increase linearly, but rather it is close to zero for $\sigma < 2.2$ g/day, and then increases very rapidly, before saturating for large σ. The $\delta^{15}N$ of body pools depends on the fractionation factor α. While the characteristic shape of the steady state body pool $\delta^{15}N$ curves as a function of σ remain the same, the degree of enrichment is determined by the fractionation factor α.

We assessed the turnover rate of the $\delta^{15}N$ of the body pools, with constant σ, and the $\delta^{15}N$ of diet switching from 0 to 5 ‰ (Figs. 4.4 and 4.5). Different pools have different turnover rates following a change in the isotope ratio of the diet. The gut protein pool turns over most rapidly following diet switch, while the intracellular body protein pool turns over most slowly. The rate of turnover following a diet switch depends on the dietary nitrogen input rate σ. The rate of turnover is slowest for low σ and increases with σ.

4.4 Discussion

We have developed a dynamical model of animal nitrogen metabolism. Our model tracks the fate of nitrogen as it is ingested as protein, incorporated into tissues, and excreted.

The model incorporates known cycling of nitrogen involved with nitrogen urea salvage and mucosal lining shedding of protein into the gut, as well as the tight regulation of the size of the body protein and plasma amino acid pools.

We also developed a corresponding system of equations that describe the metabolism of ^{15}N. Fractionation of nitrogen in urea formation is sufficient to explain the 2-6 ‰ discrimination from diet to tissue. In the model, the mechanism of the tissue-diet discrimination is the preferential formation of urea from liver ammonia and amino acids with ^{14}N. The dynamics of turnover of the intracellular protein pool are largely determined by the intake rate of nitrogen, and the gut protein and amino acid pools have one component with very fast turnover and a slow component due to the proteins of endogenous origin.

Schoeller [75] developed a simple conceptual steady state model of nitrogen balance to explain consumer diet-tissue nitrogen fractionation. In his framework, isotopes can leave the body either through a fractionated route, corresponding to urine, or an unfractionated route, corresponding to feces. He argues that nitrogen isotopes in consumer tissue are isotopically heavy compared to diet because of fractionation in nitrogen excretion, though he does not attempt to explain the large variation in nitrogen isotope consumer tissue-diet discrimination. Martinez del Rio et al. [83] developed a similar single pool mathematicaal model of nitrogen balance. They argue that the fraction of nitrogen lost through the fractionated route should increase with nitrogen intake, explaining the relationship between nitrogen intake rate and tissue-diet nitrogen discrimination. The relationship between the fraction of nitrogen lost as urea and nitrogen intake is likely complex, and a functional relationship is not easily derived.

Fractionation in our model also occurs because of preferential excretion of ^{15}N depleted urea, but our model builds upon these models in multiple ways. Our model accounts for the known physiology of nitrogen cycling in an animal, including recycling of ^{15}N depleted urea and shedding of mucosal proteins, regulation of the size of the protein pool, and regulation of urea production. This allows us to estimate the relationship between nitrogen intake rate and tissue-diet nitrogen discrimination directly, based on known physiology. Since urea formation is regulated, the fraction of nitrogen lost as urea increases with nitrogen intake, though the relationship is complex. In our model fractionation occurs in urea formation, rather than urea excretion, allowing fractionated urea to recycle through pools in the body. Therefore, the relationship between fraction of nitrogen lost as urea and δ^{15}N of tissue is damped and more complex in our model than in Martinez del Rio et al.

Balter et al. [71] developed a mass balance model of nitrogen fluxes in an animal. While their model accounts for the major cycling of nitrogen in an animal, such as gut urea recycling, they did not develop dynamic equations that describe how an animal adapts to changes in nitrogen intake rate. Our model also includes the broad scale dynamics of nitrogen cycling in an animal, and builds on this model by including dynamic equations that account for the regulation of urea formation and the size of body protein pools.

While the general structure of our model is based on physiology, undoubtedly some parameters require further refinement. It is thought that a 65 kg human requires a minimum intake of about 6.8 g N/day to maintain protein needs [84]. Our model also has a threshold such that below a certain intake level intracellular protein levels are not maintained, but at an intake of about 2.2 g N/day. However, the intake estimate of 6.8 g N/day may be an overestimate since it is likely that some leeway is required when recommending a safe minimum intake value. Also, it seems unlikely that the minimum intake value to maintain protein needs is only 30 % lower than the average daily intake of 10 g N/day.

Actual turnover rates of individual tissues may vary from those predicted by our model. It is known that different tissues, proteins, and amino acids vary in turnover rate and the isotopic composition tissues with different turnover rates may provide information regarding the timing of of diet history [54]. Our model indicates that turnover may be complicated by the structure of nitrogen cycling in an animal. Individual pools do not receive diet directly, but rather interact through the free amino acid pool, complicating isotopic turnover following a diet switch. The turnover rates of the pools in our model are strongly influenced by the rate of dietary nitrogen intake. Lower dietary nitrogen intake leads to greater recycling and reuse of amino acids by tissue protein through the free amino acid pool.

Consistent with our model, Sponheimer et al. [85] found greater hair-diet nitrogen discrimination in high protein diets in a controlled diet study of two horses. They also found that hair turned over quickly following an isotopic diet change, with equilibration occuring in less than 24 weeks. Similarly, Huelsemann et al. [86] found rapid turnover of nitrogen isotopes in human hair following a diet switch, but speculate the presence of a compartment with very slow exchange rate. If individual pools interact through the free amino acid pool as described in our model, we predict that tissues with slow turnover rates influence the turnover of other tissues such as hair, and experiments with a longer time scale are needed to determine if a tissue has truly fully equilibrated. Alternatively, if amino acids from diet are routed directly to hair rather than interacting through the free amino

acid pool, turnover may in fact be as rapid as suggested.

Our mathematical model provides a conceptual framework to better understand consumer tissue-diet nitrogen discrimination. Our model connects urea production to dietary nitrogen intake by accounting for basic nitrogen dynamics in an animal. Many other factors that are not included in the model may also affect nitrogen tissue-diet isotope discrimination. The relationship between protein metabolism and total energy intake and expenditure is complex and may affect the nitrogen budget of an animal [65, 66, 67, 70]. If energy intake is insufficient to meet energy demands, body proteins may be metabolized for energy. Protein quality may also be related to tissue-diet discrimination [58, 59]. If a diet is deficient in one or more amino acids, the biologically usable protein intake may actually be lower than the actual protein intake. Certain amino acids are highly fractionated while others are not [68], which may mean that fractionation also occurs in transamination and deamination processes unrelated to urea formation, or that certain amino acids are selectively degraded to urea. Amino acids with isotopic ratios different than bulk may be selected for the formation of certain tissues. Metabolic routing may occur, such that certain proteins or amino acids are preferentially routed to specific tissues or metabolic fates [54, 64]. Our model also assumed steady state physiological conditions in an adult. Physiological conditions that affect the nitrogen budget of an animal such as pregnancy, growth, wound healing, starvation, and the mounting of an immune response may affect nitrogen dynamics. Each of these factors represents a potential extension of the model. Nitrogen cycling in an animal is a complex process with many feedbacks and contributing cofactors. Our model begins to untangle the relationship between nitrogen cycling in an animal, diet, and stable isotope composition of tissues.

CHAPTER 5

DECONVOLUTION OF ISOTOPE SIGNALS FROM BUNDLES OF MULTIPLE HAIRS

5.1 Introduction

Organic and inorganic substances in mammals are incorporated into hair, remaining inert for relatively long periods of time [87]. Human forensic applications have long been recognized, as hair records the concentration of drugs, metabolites, toxins, and poisons at the time of formation [88, 89, 90, 91]. More recently, ecologists and anthropologists have used stable isotopes in hair to infer information about an animal's diet, migration, nutritional status, and environment [61, 92, 54, 93, 94, 95]. While the growth of hair is approximately linear, allowing the measurement of long-term chronology through segmental sampling, individual hairs typically have too low linear density to allow high-resolution sampling of a single hair. Sample sizes vary, but segments for drug testing are typically between 10 and 30 mm [88] and generally require 1-300 mg of hair [96]. Stable isotope ratios of hydrogen, carbon, nitrogen, oxygen, and sulfur require ca. 200, 50, 300, 200, and 1500 μg, respectively. To achieve these masses for animals with hair of relatively low linear density, such as humans, multiple hair strands are typically aligned at the root and combined into a single bundle for analysis [88, 97]. The challenge is to mathematically extract the true chemical signal recorded in hair given variations in growth rate and stasis, because these processes will tend to blur, or average, the temporal information recorded in hair.

Two distinct processes can cause misalignment between individual hair strands in a bundle: variation in growth phase [98] and variation in growth rate [97]. Each hair follicle cycles through three distinct phases of growth [99, 100]. In humans, approximately ninety percent of hairs are typically in the anagen, or growth, phase, which lasts for 48-72 months. The anagen phase is followed by a brief catagen phase, during which the follicle stops producing hair. The hair then enters the telogen, or resting, phase during which the follicle and hair remain dormant for 2-6 months, until the hair is shed. Variation of growth rate

between individual hairs in the growth phase can also blur the measured signal of a hair bundle. The intraindividual coefficient of variation of hair growth in humans is about 0.1 [101, 102], and similar variation has been observed in horses [103] and elephants [104]. Because individual hair strands vary in growth, signal details present in a single hair may not be captured in hair bundle measurements due to averaging misaligned hair strands in a bundle.

Previous studies assume that the measured bundle signal is equivalent to the signal of a single hair in the growth phase with average growth rate. Given known physiology of hair growth, we assume that the phase of growth and growth rates of individual hairs will vary within a bundle. We have developed a mathematical model of hair growth that describes the relationship between the signal of a bundle of hairs and the primary body signal (e.g., the isotopic pool in the body at equilibrium with hair). The model is based on an estimation of uncertainty in time since formation, or age, of the hair at a given length from the root. We used the model to develop an inverse method to estimate the primary body signal from the measured signal of a hair bundle. Our inverse method was applied to a previously described stable oxygen isotope chronology from a hair bundle of a murder victim [105] and provides a refined interpretation of the original data.

5.2 Methods

5.2.1 Model formulation

5.2.1.1 Mapping single hair signal to hair bundle measurements

Let $\phi(t)$ be the time-dependent primary body signal (e.g., drug, metabolite, isotope, etc.) to the hair. The function $\phi(t)$ refers to the input signal to the hair (e.g., the isotopic pool in the body at equilibrium with hair), not the input signal to the body (e.g., drinking water, drug dosage history, etc.), and is assumed to be equivalent to the signal of a single hair in the growth phase with the average growth rate. The expected bundle signal as a function of length is

$$\psi(l) = \int \lambda(l,\tau)\phi(\tau)d\tau, \tag{5.1}$$

where $\lambda(l,a)$ is the probability density function of time since formation, or age, of a hair at length l from the root given that the total length of the hair is at least l and the hair has not yet been shed. The kernel λ quantifies the length-dependent uncertainty in age.

5.2.1.2 Derivation of $\lambda(l, a)$

Let $\lambda(l, a)$ be the probability density function for the random variable time since formation, or age, A, of hair at length l from the root, given that the hair has not been shed and the total length of the hair is at least l. Let $\Lambda(l, a)$ be the cumulative distribution function of A, so that $\lambda(l, a) = \frac{d}{da}\Lambda(l, a)$. We assume that hair grows at constant random rate R for random time S, and then rests for random time T. We will find the distribution of Λ in terms of the distributions of R, S, and T in Tab. 5.1.

Let L be the random variable describing the total length of the hair. A hair strand is shed at random time $S + T$. Using the law of total probability, we condition on the phase of growth of the hair.

$$\begin{aligned}\Lambda(l, a) &= \Pr\left(A \leq a | L \geq l \text{ and } A \leq S + T\right) \\ &= \Pr(A \leq a | L \geq l \text{ and } A \leq S)\Pr(A \leq S | L \geq l \text{ and } A \leq S + T) + \\ &\Pr(A \leq a | L \geq l \text{ and } S \leq A \leq S + T)\Pr(S \leq A \leq S + T | L \geq l \text{ and } A \leq S + T)\end{aligned}$$

Let $g(l) = \Pr(A \leq S | L \geq l \text{ and } A \leq S + T)$. We again use the law of total probability to rewrite $\Lambda(l, a)$, this time conditioning upon the amount of time that a hair has been resting, V, given that it is in the resting phase.

$$\begin{aligned}\Lambda(l, a) &= g(l)\Pr(A \leq a | L \geq l \text{ and } A \leq S) \\ &\quad + (1 - g(l)) \int_{\tau=0}^{a} \Pr(A \leq a | L \geq l \text{ and } S \leq A \leq S + T \text{ and } V = \tau) \\ &\quad * \Pr(V = \tau | S \leq A \leq S + T) d\tau\end{aligned}$$

We will find each of these distributions in terms of the distributions in Tab. 5.1.

Table 5.1. General distributions used in hair bundle modeling

Distribution	Description
h	probability distribution function for the growth rate of hair, R
H	cumulative distribution function for the growth rate of hair, R
f_S	probability distribution function for the time spent in growth phase, S
F_S	cumulative distribution function for the time spent in growth phase, S
f_T	probability distribution function for the time spent in resting phase, T
F_T	cumulative distribution function for the time spent in resting phase, T

$$\begin{aligned}
&\Pr(A \le a | L \ge l \text{ and } A \le S) \\
&\quad = \int_0^\infty \Pr(A \le a | L \ge l \text{ and } A \le S) \Pr(R = r) dr \\
&\quad = \int_0^\infty \Pr\left(\frac{l}{r} \le a | L \ge l \text{ and } A \le S\right) h(r) dr \\
&\quad = \int_{l/a}^\infty h(r) dr \\
&\quad = 1 - H\left(\frac{l}{a}\right)
\end{aligned}$$

Similarly,

$$\begin{aligned}
&\Pr(A \le a | L \ge l \text{ and } A \le S + T \text{ and } V = \tau) \\
&\quad = \int_0^\infty \Pr(A(l) \le a | L \ge l \text{ and } A \le S + T \text{ and } V = \tau) \Pr(R = r) dr \\
&\quad = \int_0^\infty \Pr\left(\frac{l}{r} + \tau \le a | L \ge l \text{ and } A \le S + T \text{ and } V = \tau\right) h(r) dr \\
&\quad = \int_{l/(a-\tau)}^\infty h(r) dr \\
&\quad = 1 - H\left(\frac{l}{a - \tau}\right)
\end{aligned}$$

To find $\Pr(V = \tau | S \le A \le S+T)$, we find the cumulative distribution function, and then differentiate. Because the stage of hair growth is well mixed between hairs, the amount of time a hair has been resting given that it is in the resting phase, V, is uniformly distributed from 0 to T.

$$\begin{aligned}
\Pr(V \le \tau | S \le A \le S + T) &= \int_0^\infty \Pr(V \le \tau | S \le A \le S + T \text{ and } T = t) \Pr(T = t) dt \\
&= \int_0^\infty \Pr(V \le \tau | S \le A \le S + T \text{ and } T = t) f_T(t) dt \\
&= \int_0^\tau f_T(t) dt + \int_\tau^\infty \frac{\tau}{t} f_T(t) dt \\
&= F_T(\tau) + \tau \int_\tau^\infty \frac{f_T(t)}{t} dt
\end{aligned}$$

So that

$$\Pr(V = \tau | S \le A \le S + T) = \int_\tau^\infty \frac{f_T(t)}{t} dt.$$

Again, because the stage of hair growth is well mixed between hairs,

$$
\begin{aligned}
g(l) &= \Pr(A \leq S | L \geq l \text{ and } A \leq S+T) \\
&= \int_0^\infty h(r) \int_0^\infty \int_0^\infty \Pr(A \leq s | L \geq l, A \leq s+t, R=r, S=s, T=t) f_S(s) f_T(t) ds dt dr \\
&= \int_0^\infty h(r) \int_0^\infty \int_0^\infty \Pr(A \leq s | l/r \leq A \leq s+t, R=r, S=s, T=t) f_S(s) f_T(t) ds dt dr \\
&= \int_0^\infty h(r) \int_0^\infty \int_{l/r}^{s+t} \frac{s-l/r}{s+t-l/r} f_S(s) f_T(t) ds dt dr \\
&= \int_0^\infty h(r) \int_{l/r}^\infty \int_{l/r}^{v} \frac{s-l/r}{v-l/r} f_S(s) f_T(v-s) ds dv dr
\end{aligned}
$$

Putting these distributions together we have

$$\Lambda(l,a) = g(l)\left(1 - H\left(\frac{l}{a}\right)\right) + (1-g(l)) \int_0^a \left(1 - H\left(\frac{l}{a-\tau}\right)\right) \kappa(\tau) d\tau$$

where

$$g(l) = \int_0^\infty h(r) \int_{l/r}^\infty \int_{l/r}^{v} \frac{s-l/r}{v-l/r} f_S(s) f_T(v-s) ds dv dr$$

and

$$\kappa(a) = \int_a^\infty \frac{f_T(x)}{x} dx.$$

Differentiating with respect to a, we find:

$$\lambda(l,a) = g(l) \frac{l}{a^2} h\left(\frac{l}{a}\right) + (1-g(l)) \int_0^a \frac{l}{(a-\tau)^2} \kappa(\tau) h\left(\frac{l}{a-\tau}\right) d\tau.$$

5.2.1.3 Averaging due to sample interval

Signal attenuation also occurs by combining material over the sample length to obtain the mass of material required for analysis. In the case of sampling a single hair that is in the growth phase with fixed growth rate r, the expected measured signal, $f(l)$, is the average of the time-dependent primary body signal, $\phi(t)$, converted to length, over the sample length ν:

$$f(l) = \frac{r}{\nu} \int_{l/r-v/(2r)}^{l/r+v/(2r)} \phi(\tau)\, d\tau.$$

The center of the samples are at lengths $l = (2i-1)\nu/2$ where i is a positive integer. Sampling a bundle containing a large number of hairs allows for small sample length, so the measured signal of a bundle of hairs approaches $\psi(l)$.

5.2.2 Inverse method

To estimate the time-dependent input signal $\phi(t)$ from measurements of $\psi(l)$, we discretized equation 5.1 into the matrix vector equation $Kf = d$, where f is a discretization of $\phi(t)$, d is a vector containing a smoothing of the measured values of $\psi(l)$, and K is an mxn matrix. The smoothing was performed using a cubic smoothing spline with the trace of the smoother matrix chosen by generalized cross-validation, and the dimension n was chosen to be large enough to obtain an accurate quadrature approximation of λ.

As in the estimation of a primary input signal from a measured stable isotope tooth enamel signal described by Passey et al. [106], we used Tikhonov regularization to invert K, yielding the estimation

$$f_{est} = f_{guess} + K^T[KK^T + \epsilon^2 I]^{-1}[d - Kf_{guess}],$$

where I is an identity matrix, f_{guess} is an *a priori* reference vector, and ϵ is a scalar regularization parameter. The reference vector f_{guess} was chosen to be a vector containing the mean value of the measurements d.

The damping factor ϵ was chosen using generalized cross-validation. The chosen ϵ minimizes the GCV functional

$$GCV(\epsilon) = \frac{\frac{1}{n}||r_\epsilon||^2}{\left[\frac{1}{n}\text{trace}(I - A_\epsilon)\right]^2}$$

where $r_\epsilon = Kf_{est} - d$ and $A_\epsilon = K(K^TK + \epsilon^2 I)^{-1}K^T$ [107].

5.3 Results

Using the distributions in Tab. 5.2, the model depends on two parameters: γ is the fraction of hairs in the resting phase (anagen and telogen), and α is the coefficient of variation of hair growth rate. The integral transform kernel, $\lambda(l, a)$, is the probability

density function of time since formation, or age, of hair at a given length from the root and describes the amount of signal attenuation in the hair bundle signal. The kernel $\lambda(l, a)$, with $\gamma = 0.1$ and $\alpha = 0.1$, is shown in Fig. 5.1. We varied γ and α to assess how these parameters affect $\lambda(l, a)$ (Fig. 5.2). A high fraction of hairs in the resting phase, γ, results in high variance in age of hair at all lengths and a mean age that is higher than the length divided by the mean growth rate. A high coefficient of variation of hair growth rate, α, results in increasing variance of age with length. The distribution of age dictates the uncertainty in time when sampling a single hair and also the expected amount of averaging from sampling a bundle of multiple hairs.

We compared the expected value of the signal from sampling a bundle of hairs that contains hairs with varying growth rates and phases, with $\alpha = 0.1$ and $\gamma = 0.1$, to sampling a single hair that has a growth rate of 1 cm/month and sample length $\nu = 1.5$ cm (Fig. 5.3). The primary body signal is the stable nitrogen isotope record of an elephant tail hair from an individual that migrated between two isotopically distinct zones, extended periodically to create a longer signal. The primary body signal refers to the signal of the body pool at equilibrium with hair and is the signal of a single hair in the growth phase with average growth rate. Elephants have thick hairs with high linear density, allowing for high-resolution sampling of a single hair. Signal attenuation occurs when sampling a single hair because of combining material over the sample length. Combining multiple hairs into a bundle for sampling attenuates the primary body signal because of varying growth phases and growth rates of hairs in the bundle. Signal details of sufficiently short duration are highly damped and are not captured in the bundle signal because of averaging. When sampling a single hair, events of duration shorter than the sample length may not be recorded. Additionally, when sampling a single hair there is considerable uncertainty in assigning time to length since the exact growth rate and phase of growth of the sampled hair is not usually known.

To test the ability of the inverse method to accurately reconstruct a primary body signal from measurements, we used the hair bundle model, with $\alpha = 0.1$ and $\gamma = 0.1$, to create a synthetic measured bundle signal from an assumed primary body signal. We then used the inverse method to estimate the primary body signal from the synthetic bundle signal (Fig. 5.4). The primary body signal is from a previously described carbon stable isotope record of elephant tail hair in Samburu National Reserve, and represents a typical ecologically relevant body signal [93]. The estimated primary body signal is more similar to the primary body signal (correlation coefficient $R^2 = 0.81$) than the measured hair bundle

Table 5.2. Parameters and specific distributions used in hair bundle modeling.

Parameter	Description	Value
γ	fraction of hairs in resting phase	0.05, 0.1, 0.3
α	coefficient of variation of hair growth rate	0.05, 0.1, 0.25
β	average hair growth rate	1 cm/month [101, 97]
ν	average time from beginning of growth phase to hair shedding	66 months [98]

Distribution	Description	Value
h	hair growth rate probability density function	$\mathcal{N}(\beta, (\beta\alpha)^2)$
f_S	time in growth phase probability density function	$\mathcal{N}(\nu(1-\gamma), (0.1\nu(1-\gamma))^2)$
f_T	time in resting phase probability density function	$\mathcal{N}(\nu\gamma, (0.1\nu\gamma)^2)$

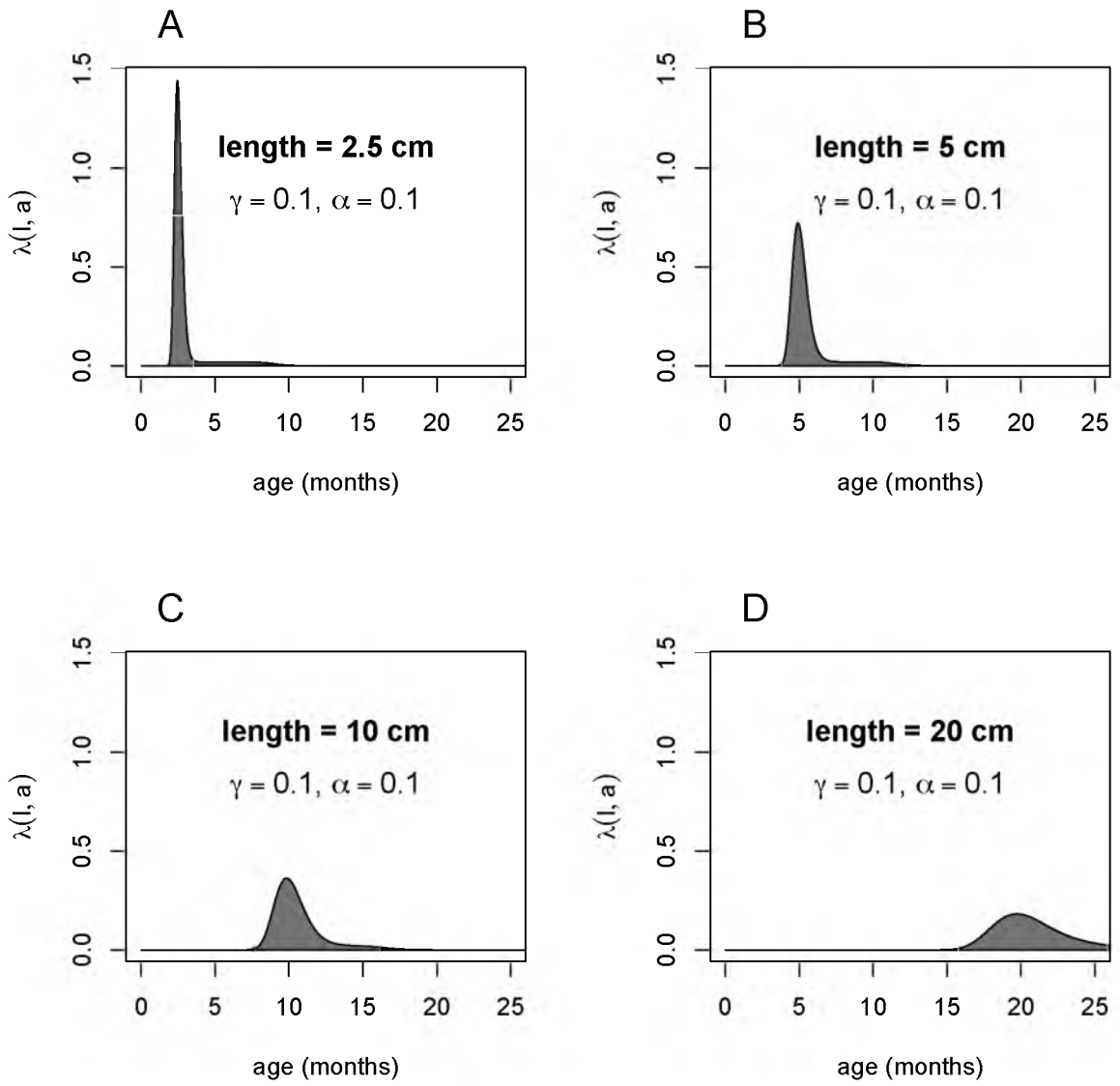

Figure 5.1. The kernel $\lambda(l, a)$ at lengths 2.5 cm, 5 cm, 10 cm, and 20 cm, A-D, respectively, describes the variation of time since formation, or age, at a given length from the root.

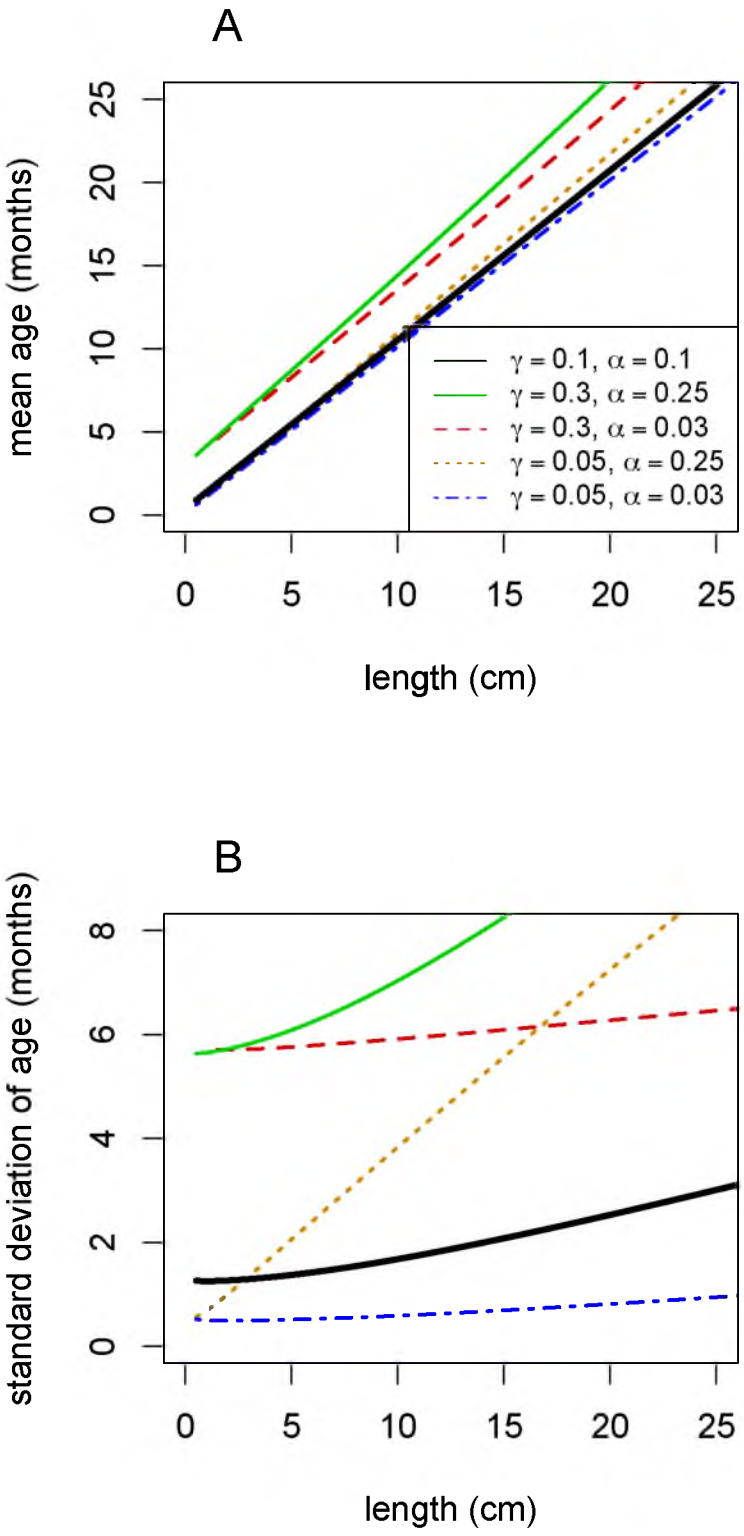

Figure 5.2. Mean, A, and standard deviation, B, of time since formation, or age, of hair at a given length from the root for various values of fraction of hairs in the resting phase, γ, and coefficient of variation of hair growth rate, α.

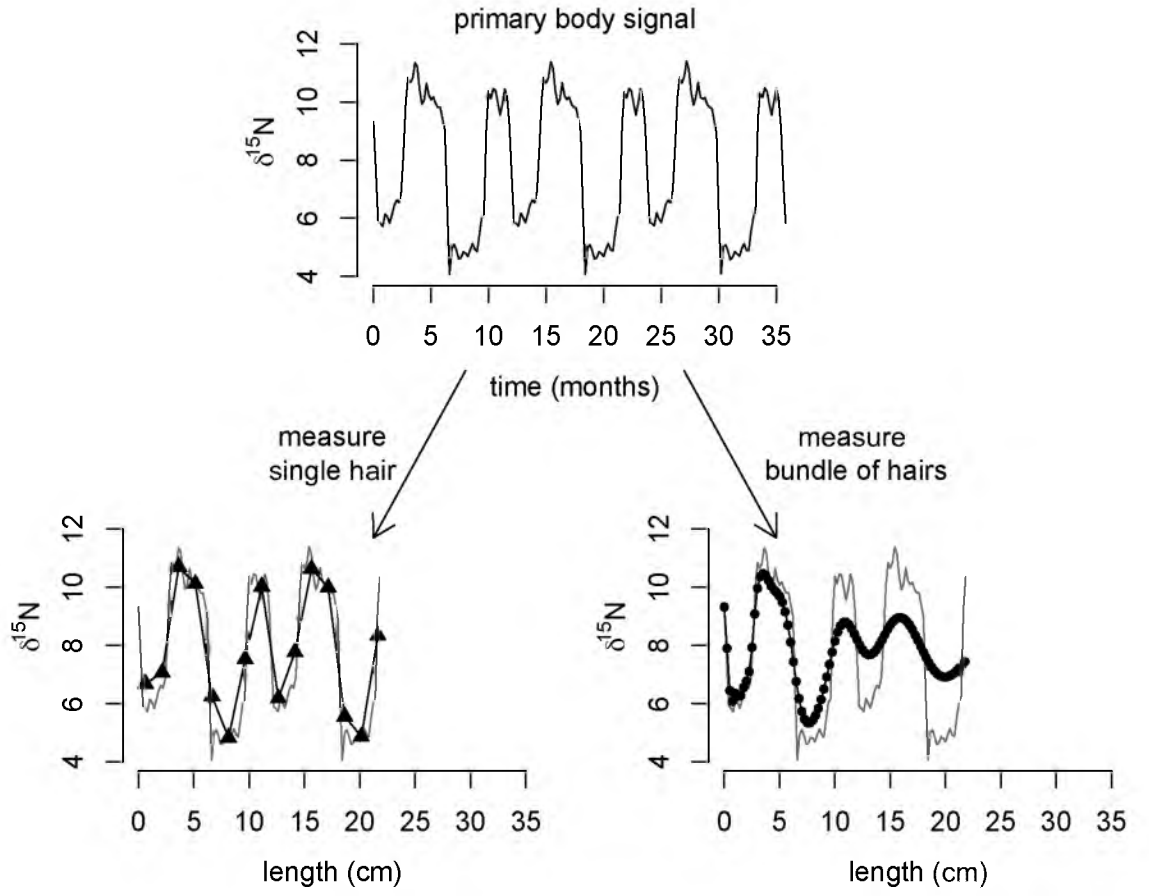

Figure 5.3. Expected length-dependent single hair signal and hair bundle signal derived from our mathematical model using an assumed time-dependent primary body signal. Time indicates months prior to root formation, length indicates cm from root. The signal of the measured bundle of hairs is highly attenuated relative to the primary body signal.

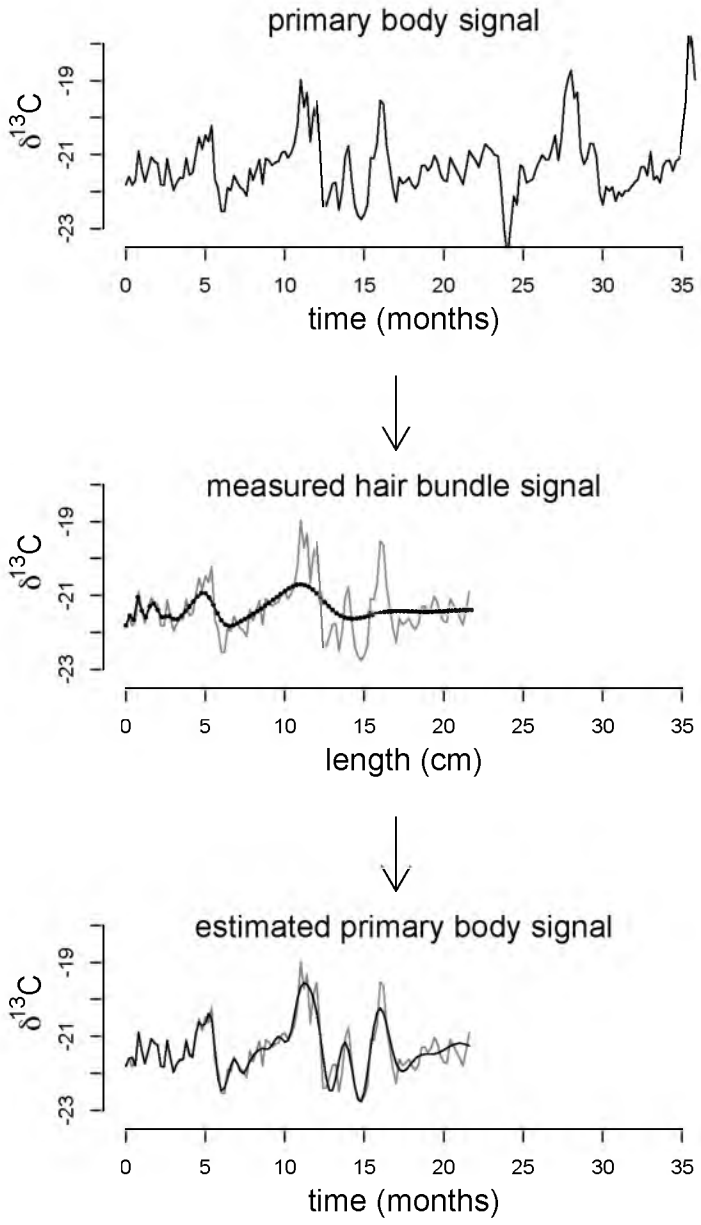

Figure 5.4. A primary body signal that is attenuated from sampling a bundle of hairs can be partially reconstructed from measurements using inverse methods. Time indicates months prior to root formation, length indicates cm from root.

signal is to the primary body signal (correlation coefficient $R^2 = 0.43$). High frequency details are lost in the estimated input signal, but the general pattern remains well estimated.

The assumed stable isotope primary input signals in Fig. 5.3 and Fig. 5.4 are from single elephant tail hairs sampled at 5 mm intervals. Elephants have thick hairs with high linear density, allowing for high-resolution sampling of a single hair. The data in Fig. 5.3 represent an individual migrating between two areas with different δ^{15}N values for vegetation and thus an abrupt change in δ^{15}N occurs at each migration event [108]; transitions between areas were made in less than 12 hours based on GPS-tracking data. Migration events result in a signal approximating a step function. Data from this individual are previously unpublished, but the individual had behavior analogous to that described by Cerling et al. [108]. The data in Fig. 5.4 are from Cerling et al. [93] and represents gradual diet transitions coinciding with two rainy seasons per year. Samples were run on an isotope ratio mass spectrometer in continuous-flow mode coupled to an elemental analyzer (EA-CF-IRMS).

5.4 Application of inverse method to murder victim data

We applied the inverse method to previously described oxygen stable isotope measurements from the organic component of a hair bundle of an unidentified murder victim, with $\gamma = 0.1$ and $\alpha = 0.1$ (Figs. 5.5 and 5.6) [105, 109]. Oxygen stable isotope measurements of the organic component of hair can be used to determine time-dependent geographic region-of-origin because oxygen isotopes in drinking water vary with location [110] and are incorporated into hair [111, 112].

The confidence interval for the estimated primary body signal was obtained by inverting data with noise added to each measurement. We created 1000 replicates of measurements by adding normally distributed noise with mean zero and standard deviation of 0.15 ‰ to each measurement. For each set of measurements with added noise, we selected a regularization parameter using generalized cross validation, and performed the inversion using Tikhonov regularization to estimate the primary body signal. We excluded 48 estimates of the primary body signal because their isotope values lay outside the biologically feasible range of 7 to 16 ‰. The shaded region corresponds δ^{18}O within two standard deviations of the mean estimated primary body signal.

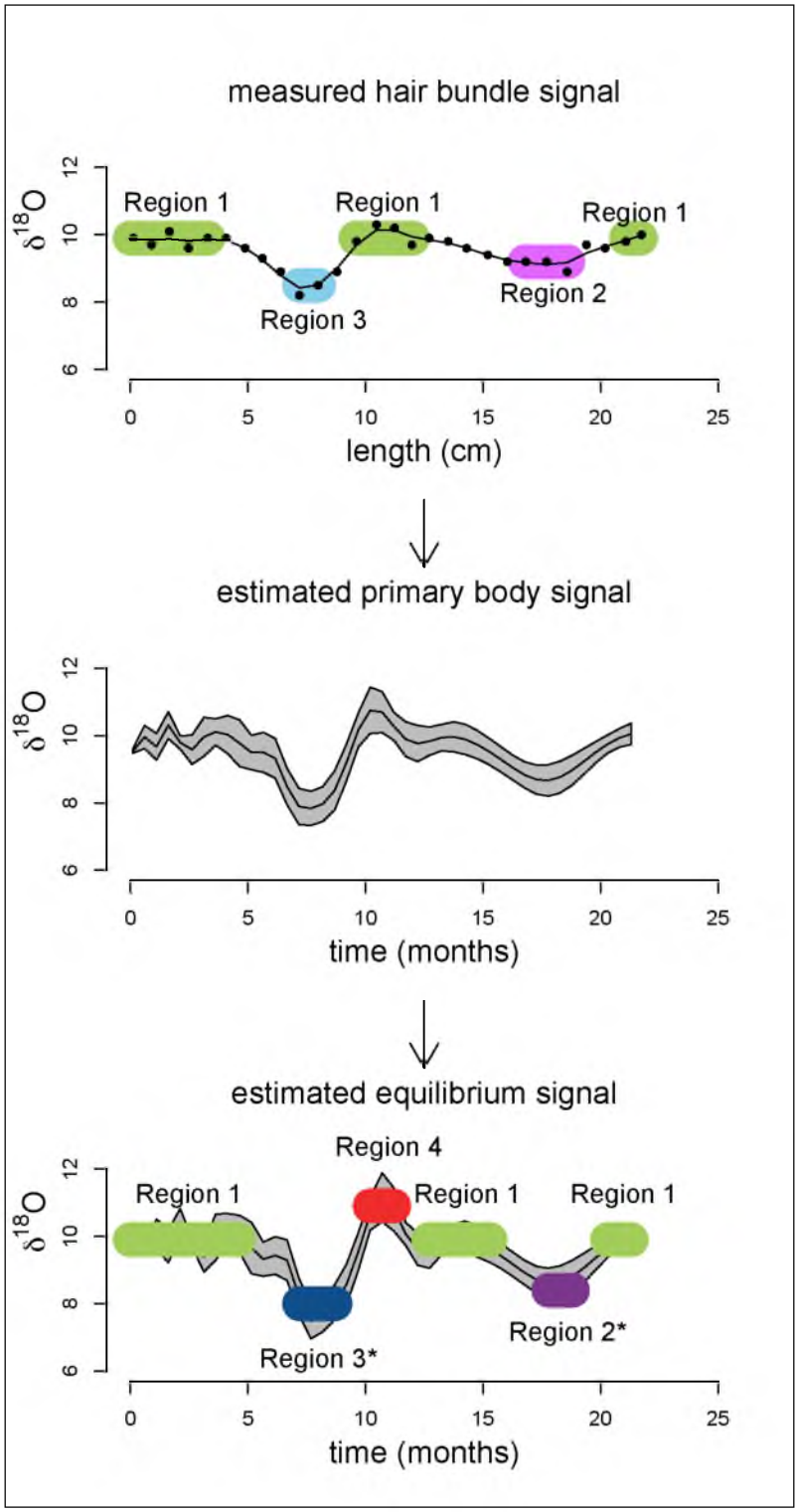

Figure 5.5. Estimated primary body signal and equilibrium signal from hair δ^{18}O measurements of a previously described hair bundle of a murder victim.

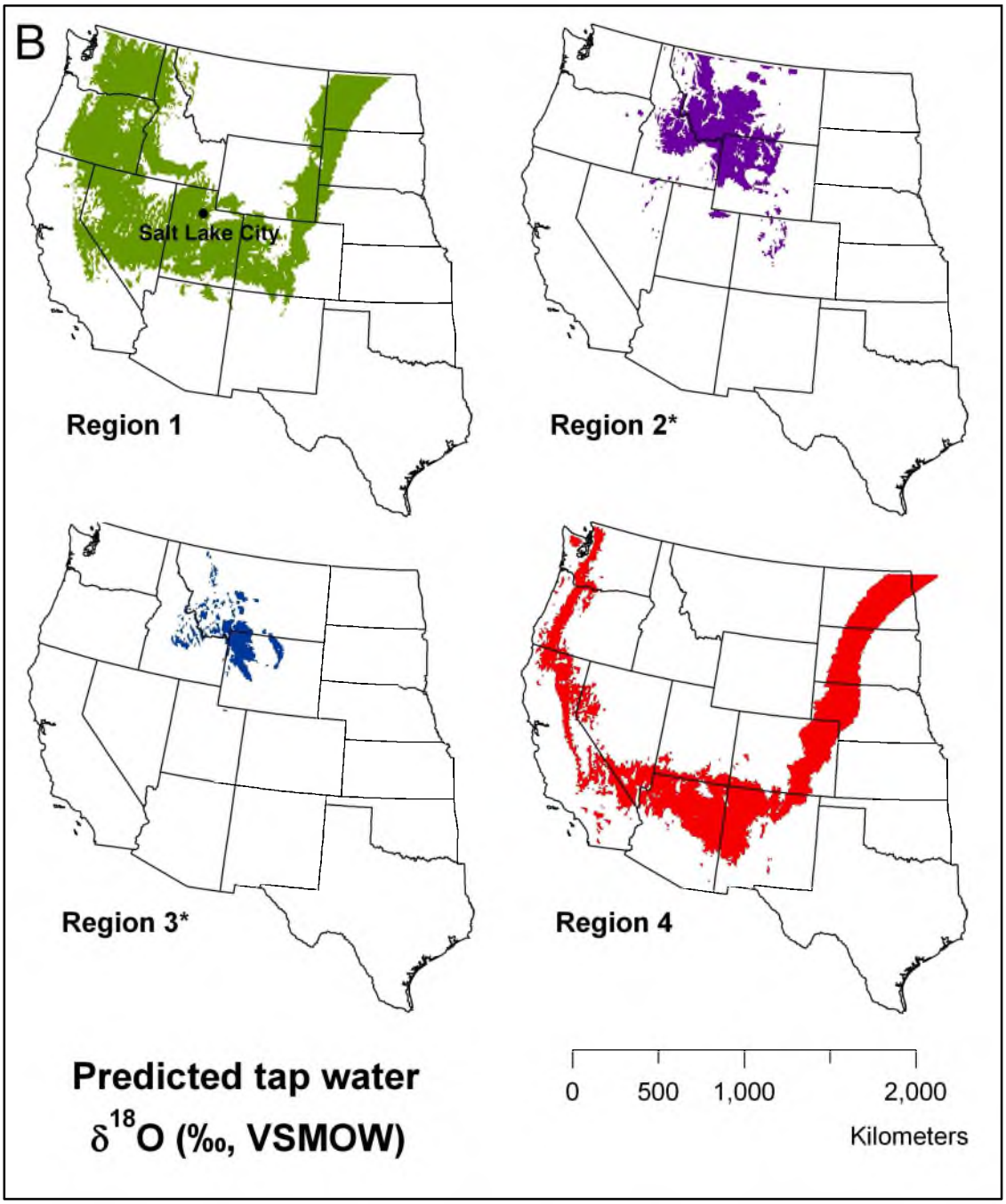

Figure 5.6. Tap water maps for geographic regions predicted by the estimated equilibrium signal.

5.4.1 Estimating equilibrium signal from estimated primary body signal

The model inversion yields an estimate of the primary body pool at equilibrium with the hair, not the input signal to the body. The body equilibrium signal refers to the primary body signal if it were in instantaneous equilibrium with the input. The body equilibrium signal can be reconstructed using a previously described method based on multiple pools with first order kinetics contributing to the primary body pool that is at equilibrium with hair [113, 114]. Briefly, the isotope composition of the j^{th} pool contributing to hair formation at time t is

$$\delta_j^t = \delta_j^{t-1} e^{-\lambda_j \Delta t} + \delta^{eq}(1 - e^{-\lambda_j \Delta t})$$

where δ_j^{t-1} is the isotope composition of the j^{th} pool at time $t-1$, Δt is the difference in time between $t-1$ and t, λ_j is the rate constant of the j^{th} pool, and δ_{eq} is the isotope composition of the pool if it were at instantaneous equilibrium with the environment. For a p pool system, δ_{eq} can be calculated incrementally from the stable isotope signal of a single hair, δ_H^t, as

$$\delta_{eq}^t = \frac{\delta_H^t - \sum_{i=1}^{p} f_i \delta_i^{t-1} e^{-\lambda_i \Delta t}}{\sum_{i=1}^{p} f_i (1 - e^{-\lambda_i \Delta t})}$$

where f_i is the fractional contribution of of pool i to the pool at equilibrium with hair. For application to the murder victim, we used a single pool with half-life of 7 days.

5.4.2 Region-of-origin maps

Region-of-origin maps were created in two steps. For each region, we used the semi-mechanistic model by Ehleringer et al. [112] to predict drinking water δ^{18}O values required to produce the hair isotope ratio, with an added 0.5 ‰ to either side of the hair value. Once the maximum and minimum δ^{18}O values of drinking water were predicted for each isotopic region, we used the δ^{18}O tap water isoscape produced by Bowen et al. [115] for the contiguous United States to identify regions with isotope values matching our predicted range. Regions with matching isotope values were highlighted in color using ArcGIS 9.3.1®.

The data were originally interpreted as movement between three isotopically distinct geographic regions, Regions 1, 2, and 3, corresponding to measured δ^{18}O values of approximately 9.9 ‰, 8.4 ‰, and 9.2 ‰, respectivly. The transitions from Region 1 to Region 2 and from Region 2 to Region 1 at about 20 cm and 15 cm, respectively, occur over multiple

cm (or equivalently multiple months) of growth, slow movement between geographic regions. The transitions from Region 1 to Region 3 and from Region 3 to Region 1 at about 9 cm and 5 cm, respectively, occur over a short length interval, rapid movement between geographic regions. Region 1 is consistent with the location where the victim was found, Salt Lake City, UT.

The inverse method was applied to the measured hair δ^{18}O to estimate the primary body signal. In addition to averaging due to hair bundling, turnover of the primary body pool must also be accounted for to determine geographic search regions. We used a previously described method [113, 114] to estimate the isotopic composition of the primary body pool if it were at instantaneous equilibrium with the environment from the estimated primary body signal. To estimate the equilibrium signal, we assumed a single pool with turnover half-life of 7 days, which is consistent with observations of hair oxygen stable isotopes in humans (calculated from [111, 112]). In this case, the estimated equilibrium signal is very similar to the estimated primary body signal (correlation coefficient $R^2 = 0.89$) because of rapid turnover of the primary body pool relative to changes in the input signal. Estimated tap water maps were produced using a previously described relationship between hair organic δ^{18}O and drinking water δ^{18}O [112] and a relationship between tap water and geography [115].

The estimated equilibrium signal differs from the measured hair bundle in several important ways (Figs. 5.5, 5.6, 5.7, and 5.8). Transitions between isotopically distinct regions are more rapid, with more time spent in each region. Region 2* and Region 3* have lower δ^{18}O than Region 2 and Region 3, respectively, and correspond to different geographic regions (Fig. 5.7). Regions 2* and 3* have considerable overlap (Fig. 5.8), suggesting that they may correspond to the same geographic location. Region 1 is isotopically similar in both the measurements and the estimated equilibrium signal, and the δ^{18}O is consistent with the location where the victim was found. The estimated equilibrium signal has a new short duration region, Region 4, with δ^{18}O of about 10.9 ‰ that does not appear in the measured hair bundle signal. Plotted maps were restricted to the western United States. Region 4 also contains a small region in the northeast United States as well as parts of Canada.

5.5 Discussion

Multiple hairs that may be in different growth phases and have different growth rates are typically combined into a single bundle of hairs for segmental analysis. We have developed a

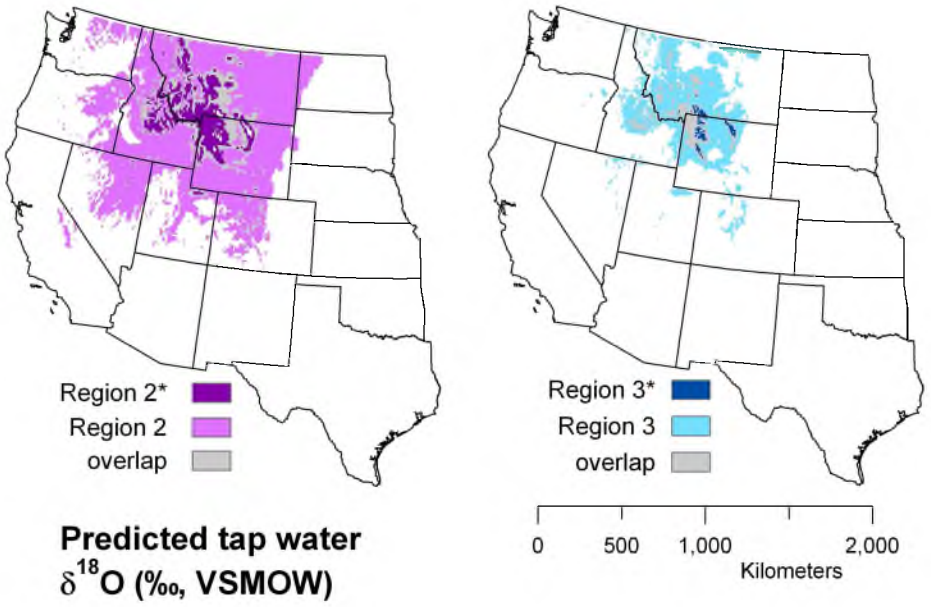

Figure 5.7. Comparison of Region 2 with Region 2* and Region 3 with Region 3*.

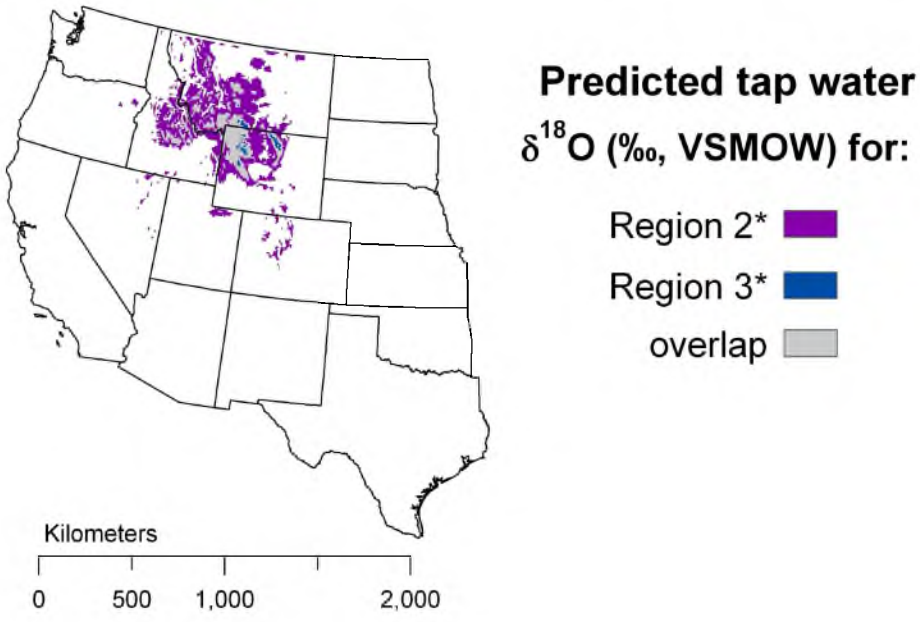

Figure 5.8. Comparison of Region 2* with Region 3*.

mathematical model that describes the signal averaging caused by bundling hairs for analysis as well as an inverse method to estimate the primary body signal from measurements of a hair bundle. If the growth rates of hairs within a bundle vary substantially or a high proportion of hairs are in the resting phase of hair growth, the measured hair bundle signal is highly averaged relative to the primary body signal, which may lead to misinterpretation of the signal.

Our model is based on uncertainty in time since formation, or age, of hair a given length from the root. Assigning times to length when sampling a single hair strand also relies on an estimation of length-dependent age variation. High variation in growth rates or a high proportion of hairs in the resting phase of hair growth leads to high uncertainty in assigning time to measurements along the length of a single hair strand.

The determination of whether to bundle hairs or sample a single hair depends on the research question. If precise timing of an event is critical or high-resolution sampling is desired to capture events in the recent past, multiple hairs should be combined into a bundle to decrease sample length and reduce uncertainty in the time corresponding to measurements. If multiple hairs are to be combined, it is preferred to combine many hairs rather than few, as the uncertainty in the bundle signal decreases with the number of hairs. If the amplitude of a long duration event is more important or an individual hair strand has high enough linear density to allow for a high-resolution sample interval, sampling a single hair strand may result in less signal averaging than sampling a bundle of hairs. When sampling a single hair, however, there may be high uncertainty in assigning time to measurements.

The inverse method we developed allows for the estimation of the primary body signal from a measured hair bundle signal. The method is especially useful in situations where the primary body signal is averaged, but characteristics of the signal remain. If the averaging is significant enough, however, noise may dominate, preventing meaningful reconstruction of the primary body signal.

It may be possible to minimize signal averaging from bundling multiple hairs by ensuring hairs are in the growth phase. Van Scott et al. have described a technique to examine a hair's follicle to determine its phase of growth [116], though this is only possible if a hair's root can be observed (i.e., hair was plucked rather than cut). Excluding hairs in the resting phase from a bundle has been shown to reduce the growth cycle error in hair stable isotope analysis [117]. This can be incorporated into our model by reducing γ, the fraction of hairs

in the resting phase, which results in less signal averaging. If the hair has never been cut, selecting hairs for analysis with small total length also increases the likelihood of hair being in the growth phase. Since each hair grows for a period of time before shedding, hairs with small total length are more likely to be in the growth phase. However, the bundled signal will still be attenuated due to variation in growth rate of individual hairs.

We applied our inverse method to a previously described [105, 109] oxygen stable isotope chronology from the organic component of the hair of a murder victim. The signal obtained from the inverse method is an estimate of the δ^{18}O of the primary body pool that is in equilibrium with the hair, rather than the time-dependent isotopic composition of drinking water. Applying a model of turnover of the primary body pool δ^{18}O to the estimated primary body signal provides an estimate of the equilibrium signal. This further sharpens the transitions between regions, though the effect is small due to the relatively rapid turnover of oxygen isotopes in the primary body pool at equilibrium with hair. In cases where turnover of the body pool at equilibrium with hair is slow (e.g., carbon [118] and nitrogen isotopes [85]), the signal attenuation caused by turnover of the body pool may be larger than that caused by bundling multiple hairs. The search maps determined by the estimated equilibrium signal differ from previously published interpretations in several important ways. Transitions between isotopically distinct regions are more rapid, and the δ^{18}O of the regions are different. An additional region of short duration is present in the estimated equilibrium, that may have been have averaged by measuring a bundle of multiple hairs.

Similar methods may also be used to estimate uncertainty in time since formation, when time cannot be constrained using other methods, in other length-dependent measurements of "ecological tape recorders," such as measurements of nails, horn, or tropical trees lacking growth rings. Additionally, similar probability density functions may be useful for estimating the uncertainty in age of an animal or plant from size or length. The details of these methods will depend on growth characteristics. Other biological systems, such as cell-cycle dependent processes, also rely on inverse methods to estimate individual signal from population-level measurements [119, 120, 121, 122]. In these models, variation in cell-cycle phase of individual cells can result in important differences between population measurements and individual cell dynamics.

Hair records the concentration of drugs, toxins, metabolites, and stable isotopes in the body as it grows. Segmental analysis of a bundle of hair allows for the construction of a high-resolution record of the history of an animal. However, variation in the growth of

individual hair strands can distort the relation between measurements and the actual history of the animal. Our mathematical model provides an estimate of uncertainty in time since formation, or age, of a hair strand a given length from the root as well as an inverse method to estimate the time-dependent primary body signal (e.g., drug, metabolite, isotope, etc.) from segmental analysis of a bundle of hairs, based on measurable growth characteristics of individual hair strands.

REFERENCES

[1] Nourjah P, Ahmad SR, Karwoski C, and Willy M. Estimates of acetaminophen (paracetamol)-associated overdoses in the United States. *Pharmacoepidemiol Drug Saf*, 15:398–405, 2006.

[2] Mitchell JR, Jollow DJ, Potter WZ, Davis DC, Gillette JR, and Brodie BB. Acetaminophen-induced hepatic necrosis. I. Role of drug metabolism. *J Pharmacol Exp Ther*, 187:185–194, 1973.

[3] Bond GR. Acetaminophen protein adducts: A review. *Clinical Toxicology*, 47(1):2–7, 2009.

[4] Mitchell JR, Jollow DJ, Potter WZ, Gillette JR, and Brodie BB. Acetaminophen-induced hepatic necrosis. IV. Protective role of glutathione. *J Pharmacol Exp Ther*, 187:211–217, 1973.

[5] Mitchell JR, Thorgeirsson SS, Potter WZ, Jollow DJ, and Keiser H. Acetaminophen-induced hepatic injury: Protective role of glutathione in man and rationale for therapy. *Clin Parmacol Ther*, 16:676–684, 1974.

[6] Potter WZ, Davis DC, Mitchell JR, Jollow DJ, Gillette JR, and Brodie BB. Acetaminophen-induced hepatic necrosis. III. Cytochrome p-450 mediated covalent binding in vitro. *J Pharmacol Exp Ther*, 187:203–210, 1973.

[7] Jollow DJ, Mitchell JR, Potter WZ, Davis DC, Gillette JR, and Brodie BB. Acetaminophen-induced hepatic necrosis II. Role of covalent binding in vivo. *J Pharmacol Exp Ther*, 187:195–202, 1973.

[8] Schmidt LE, Dalhoff K, and Poulsen HE. Acute versus chronic alcohol consumption in acetaminophen-induced hepatotoxicity. *Hepatology*, 35:876–882, 2002.

[9] Smilkstein MJ, Knapp GL, Kulig KW, and Rumack BH. Efficacy of oral N-acetylcystein in the treatment of acetaminophen overdose: Analysis of the National Multicenter Study (1975 to 1985). *N Engl J Med*, 319(24):1557–1562, 1988.

[10] Singer AJ, Carracio TR, and Mofenson HC. The temporal profile of increased transaminase levels in patients with acetaminophen-induced liver dysfunction. *Ann Emerg Med*, 25:49–53, 1995.

[11] Slattery JT, Wilson JM, Kalhorn TF, and Nelson SD. Dose-dependent pharmacokinetics of acetaminophen: Evidence of glutathione depletion in humans. *Clin Pharmacol Ther*, 41:413–418, 1987.

[12] Price CP and Alberti KGMM. Biochemical assessment of liver function. *In Wright R., Alberti K. G. M. M., Karran S., Millward-Sadler G. H., eds. Liver and Billiary disease: pathophysiology, diagnosis, management.*, 1979.

[13] Harrison PM, O'Grady JG, Keays RT, Alexander GJ, and Williams R. Serial prothrombin time as prognostic indicator in paracetamol induced fulminant hepatic failure. *Br Med J*, 301:964–966, 1990.

[14] AK Sohlenius-Sternbeck. Determination of the hepatocellularity number for human, dog, rabbit, rat and mouse livers from protein concentration measurements. *Toxicology in Vitro*, 20(8):1582–1586, 2006.

[15] Furchtgott LA, Chow CC, and Periwal V. A model of liver regeneration. *Biophysical Journal*, 96(10):3926–3935, 5 2009.

[16] Donaldson BW, Gopinath R, Wanless IR, Phillips MJ, Cameron R, Roberts EA, Greig PD, Levy G, and Blendis LM. The role of transjugular liver biopsy in fulminant liver failure: Relation to other prognostic indicators. *Hepatology*, 18:1370–1376, 1993.

[17] Rumack BH and Matthew H. Acetaminophen poisoning and toxicity. *Pediatrics*, 55(6):871–876, 6 1975.

[18] Miner DJ and Kissinger PT. Evidence for the involvement of n-acetyl-p-benzoquinone imine in acetaminophen metabolism. *Biochem Pharmacol*, 28:3285–3290, 1979.

[19] Ookhtens M, Hobdy K, Corvasce MC, Aw TY, and Kaplowitz N. Sinusoidal efflux of glutathione in the perfused rat liver. *J Clin Invest*, 75, 1985.

[20] Lauterburg BH, Adams JD, and Mitchell JR. Hepatic glutathione homeostasis in the rat: Efflux accounts for glutathione turnover. *Hepatology*, 4(4):586–590, 1984.

[21] Aw TY, Ookhtens M, Clement R, and Kaplowitz N. Kinetics of glutathione efflux from isolated rat hepatocytes. *Am J Physiol Gast Liver*, 250:G236–G243, 1986.

[22] Pehlivanov B, Milchev N, and Kroumov G. Factor VII deficiency and its treatment in delivery with recombinant factor VII. *European Journal of Obstetrics & Gynecology and Reproductive Biology*, 116(2):237–238, 10 2004.

[23] Chun LJ, Tong MJ, Busuttil RW, and Hiatt JR. Acetaminophen hepatotoxicity and acute liver failure. *J Clin Gastroenterol*, 43(4):342–349, 2009.

[24] O'Grady JG, Alexander GJ, Hayllar KM, and Williams R. Early indicators of prognosis in fulminant hepatic failure. *Gastroenterology*, 97(2):439–445, 1989.

[25] Lee WM, Squires RH, Nyberg SL, Doo E, and Hoofnagle JH. Acute liver failure: Summary of a workshop. *Hepatology*, 47(4):1401–1415, 2008.

[26] Sivilotti MLA, Good AM, Yarema MC, Juurlink DN, and Johnson DW. A new predictor of toxicity following acetaminophen overdose based on pretreatment exposure. *Clinical Toxicology*, 43:229–234, 2005.

[27] Craig DG, Ford AC, Hayes PC, and Simpson KJ. Systematic review: prognostic tests of paracetamol-induced acute liver failure. *Ailment Pharmacology and Therapeutics*, 31:1064–1976, 2010.

[28] Bailey B, Amre DK, and Gaudreault P. Fulminant hepatic failure secondary to acetaminophen poisoning: A systematic review and meta-analysis of prognostic criteria determining the need for liver transplantation. *Crit Care Med*, 31(1):299–305, 2003.

[29] Renner EL. How to decide when to list a patient with acute liver failure for liver transplantation? Clichy or King's College Criteria, or something else? *J Hepatology*, 46:554–557, 2007.

[30] Schmidt LE and Dalhoff K. Alpha-fetoprotein is a predictor of outcome in acetaminophen-induced liver injury. *Hepatology*, 41:26–31, 2005.

[31] Mitchell I, Bihari D, Chang R, Wendon J, and Williams R. Earlier identification of patients at risk from acetaminophen-induced acute liver failure. *Crit Care Med*, 26:279–284, 1998.

[32] Bernal W, Auzinger G, Sizer E, and Wendon J. Early prediction of outcome of acute liver failure using bedside measurement of interleukin-6. *Hepatology*, 46(Suppl. 1):617A, 2007.

[33] Zaman MB, Hoti E, Qasim A, Maguire D, McCormick PA, Hegarty JE, Geoghegan JG, and Traynor O. MELD score as a prognostic model for listing acute liver failure patients for liver transplantation. *Transplant Proc*, 38:2097–2098, 2006.

[34] Bechmann LP, Jochum C, Kocabayoglu P, Sowa JP, Kassalik M, Gieseler RK, Saner F, Paul A, Trautwein C, Gerken G, and Canbay A. Cytokeratin 18-based modification of the MELD score improves prediction of spontaneous survival after acute liver injury. *J Hepatology*, 53(4):639–647, 2010.

[35] Bernal W and Wendon J. More on serum phosphate and prognosis of acute liver failure. *Hepatology*, 38:533–534, 2003.

[36] Bernal W, Donaldson N, Wyncoll D, and Wendon J. Blood lactate as an early predictor of outcome in paracetamol-induced acute liver failure: A cohort study. *Lancet*, 359:558–563, 2002.

[37] Schmidt LE and Larsen FS. Is lactate concentration of major value in determining the prognosis in patients with acute liver failure? Hardly. *J Hepatol*, 53:211–212, 2010.

[38] Rumack BH. Acetaminophen overdose in young children. *Am J Dis Child*, 138:428–433, 1984.

[39] McClain CJ, Kromhout JP, Peterson FJ, and Holtzman JL. Potentiation of acetaminophen hepatotoxicity by alcohol. *JAMA*, 244:251–253, 1980.

[40] Lesser PB, Vietti MM, and Clark WD. Lethal enhancement of therapeutic doses of acetaminophen by alcohol. *Dig Dis Sci*, 3:103–105, 1986.

[41] Bonkovsky HL, Kane RE, Jones DP, Galinsky RE, and Banner B. Acute hepatic and renal toxicity from low doses of acetaminophen in the absence of alcohol abuse or malnutrition: Evidence for increased susceptibility to drug toxicity due to cardiopulmonary and renal insufficiency. *Hepatology*, 19:1141–1148, 1994.

[42] McClements BM, Hyland M, Callender ME, and Blair TL. Management of paracetamol poisoning complicated by enzyme induction due to alcohol or drugs. *Lancet*, 335:1526, 1990.

[43] Pirotte JH. Apparent potentiation of hepatotoxicity from small doses of acetaminophen by phenobarbital. *Ann Intern Med*, 101:403, 1984.

[44] Crippin JS. Acetaminophen hepatotoxicity: Potentiation by isoniazid. *Am J Gastroenterol*, 88:590–592, 1993.

[45] James LP, Letzig L, Simpson PM, Capparelli E, Roberts DW, Hinson JA, Davern TJ, and Lee WM. Pharmacokinetics of acetaminophen protein adducts in adults with acetaminophen overdose and acute liver failure. *Drug Metab Dispos*, 37:1–6, 2009.

[46] Gregory B, Larson AM, Reisch J, and Lee WM. Acetaminophen dose does not predict outcome in acetaminophen-induced acute liver failure. *J Invest Med*, 58:707–710, 2010.

[47] Larson AM, Polson J, Fontana RJ, Davern TJ, Lalani E, Hynan LS, Reisch JS, Schiødt FV, Ostapowicz G, Shakil AO, and Lee WM. Acetaminophen-induced acute liver failure: Results of a United States multicenter, prospective study. *Hepatology*, 42(6):1364–1372, 2005.

[48] Paulose-Ram R, Hirsch R, Dillon C, Losonczy K, Cooper M, and Ostchega Y and. Prescription and non-prescription analgesic use among the US adult population: results from the third National Health and Nutrition Examination Survey (NHANES III). *Pharmacoepidemiology and Drug Safety*, 12:315–326, 2003.

[49] Li C and Martin BC. Trends in emergency department visits attributable to acetaminophen overdoses in the United States: 1993-2007. *Pharmacoepidemiology and Drug Safety*, 20:810–818, 2011.

[50] Lee WM. Drug-induced hepatotoxicity. *N Engl J Med*, 349:474–485, 2003.

[51] Schiodt FV, Rochling FJ, Casey DL, and Lee WM. Acetaminophen toxicity in an urban county hospital. *N Engl J Med*, 337:1112–1117, 1997.

[52] Wolf MS, King J, Jacobson K, Di Francesco L, Cooper Bailey S, Mullen R, McCarthy D, Serper M, Davis TC, and Parker RM. Risk of unintentional overdose with non-prescription acetaminophen products. *J Gen Intern Med*, page Epub ahead of print, 2012.

[53] Martinez del Rio C, Wolf N, Carleton SA, and Gannes LZ. Isotopic ecology ten years after a call for more laboratory experiments. *Biological Reviews*, 84:91–111, 2009.

[54] Wolf N, Carleton SA, and Martinez del Rio C. Ten years of experimental animal isotopic ecology. *Functional Ecology*, 23(1):17–26, 2009.

[55] Vanderklift MA and Ponsard S. Sources of variation in consumer-diet δ^{15}N enrichment: a meta-analysis. *Oecologia*, 136:169–182, 2003.

[56] Vander Zander MJ, Cabana G, and Rasmussen JB. Comparing trophic position of freshwater littoral fish species using stable nitrogen isotopes δ^{15}N and literature dietary data. *Canadian Journal of Fisheries and Aquatic Sciences*, 54:1142–1158, 1997.

[57] Post DM. Using stable isotopes to estimate trophic position: Models, methods, and assumptions. *Ecology*, 83:703–718, 2002.

[58] Roth JD and Hobson KA. Stable carbon and nitrogen isotopic fractionation between diet and tissue of captive red fox: Implications for dietary consideration. *Canadian Journal of Zoology*, 78:848–852, 2000.

[59] Robbins CT, Felicetti LA, and Florin ST. The impact of protein quality on stable isotope discrimination and assimilated diet estimation. *Oecologia*, 162:571–579, 2010.

[60] Pearson SF an Levey DJ and Martinez del Rio C. Effects of elemental composition on the incorporation of dietary nitrogen and carbon isotopic signatures in an omnivorous songbird. *Oecologia*, 135:516–523, 2003.

[61] Martinez del Rio C, Wolf N, Carleton SA, and Gannes LZ. Isotopic ecology ten years after a call for more laboratory experiments. *Biological Reviews*, 84:91–111, 2009.

[62] Fuller MF and Reeds PJ. Nitrogen cycling in the gut. *Annual Review of Nutrition*, 18:385–411, 1998.

[63] Bergen WG and Wu Guoyao. Intestinal nitrogen recycling and utilization in health and disease. *The Journal of Nutrition*, 139(5):821–825, 2009.

[64] Schwartz HP. Some theoretical aspects of isotope paleodiet studies. *Journal of Archaeological Science*, 18:261–275, 1991.

[65] Hobson KA, Alisauskas RT, and Clark RG. Stable-nitrogen isotope enrichment in avian tissues due to fasting and nutritional stress: Implications for isotopic analysis of diet. *Condor*, 95:388–394, 1993.

[66] Adams TS and Sterner RW. The effect of dietary nitrogen content on trophic level ^{15}N enrichment. *Limnology and Oceanography*, 45(3):601–607, 2000.

[67] Fuller BT, Fuller JL, Sage NE, Harris DA, O'Connell TC, and Hedges REM. Nitrogen balance and δ^{15}N: Why you're not what you eat during nutritional stress. *Rapid Communications in Mass Spectrometry*, 19:2497–2506, 2005.

[68] DeNiro MJ and Epstein S. Influence of diet on the distribution of nitrogen isotopes in animals. *Geochim Cosmochim Acta*, 45:341–351, 1981.

[69] McClelland JW and adn Montoya JP. Trophic relationships and the nitrogen isotopic composition of amino acids in plankton. *Ecology*, 83:2173–2180, 2002.

[70] MacAvoy SE, Arneson LS, and Bassett E. Correlation of metabolism with tissue carbon and nitrogen turnover rate in small mammals. *Oecologia*, 150:190–201, 2006.

[71] Balter V, Simon L, Fouillet H, and Lecuyer C. Box-modeling of δ^{15}N/δ^{14}N in mammals. *Oecologia*, 147:212–222, 2006.

[72] Fuller BT, Fuller JL, Sage NE, Harris DA, O'Connell TC, and Hedges REM. Nitrogen balance and δ^{15}N: Why you're not what you eat during pregnancy. *Rapid Communications in Mass Spectrometry*, 18:2889–2896, 2004.

[73] Carleton SA and Martinez del Rio C. Growth and catabolism in isotopic incorporation: a new formulation and experimental data. *Functional Ecology*, 24:805–812, 2010.

[74] Gannes LZ, Martinez del Rio C, and Koch P. Natural abundance variations in stable isotopes and their potential uses in animal physiological ecology. *Comparative Biochemistry and Physiology*, 119:725–737, 1988.

[75] Schoeller DA. Isotope fractionation: Why aren't we what we eat? *Journal of Archaeological Science*, 26:667–673, 1999.

[76] Chacko A and Cummings JH. Nitrogen losses from the human small bowel: Obligatory losses and the effect of physical form of food. *Gut*, 29:809–815, 1988.

[77] Fouillet H, Juillet B, Bos C, Mariotti F, Gaudichon C, Benamouzig R, and Tome D. Urea-nitrogen production and salvage are modulated by protein intake in fed humans: Results of an oral stable-isotope-tracer protocol and compartmental modeling. *Am J Clin Nutr*, 87(1702-1714), 2008.

[78] Langran M, Moran BJ, Murphy JL, and Jackson AA. Adaptation to a diet low in protein: effect of complex carbohydrate upon urea kinetics in normal man. *Clin Sci (Lond)*, 82(2):191–198, 1992.

[79] Linder MC. *Nutrition and metabolism of proteins. In Nutritional Biochemistry and Metabolism.* Elsevier, 1985.

[80] Swick RW and Song H. Turnover rates of various muscle proteins. *Journal of Animal Science*, 38(5):1150–1157, 1974.

[81] Tome D and Bos C. Dietary protein and nitrogen utilization. *The Journal of Nutrition*, 130:1868S–1873S, 2000.

[82] Steffee WP, Goldsmith RS, Pencharz PB, Scrimshaw NS, and Young VR. Dietary protein intake and dynamic aspects of whole body nitrogen metabolism in adult humans. *Metabolism*, 25(3):281–297, 1976.

[83] Martinez del Rio C and Wolf BO. *Mass balance models for animal isotopic ecology.* Science Publishers, 2005.

[84] Rand WM, Pellett PL, and Young VR. Meta-analysis of nitrogen balance studies for estimating protein requirements in healthy adults. *Am J Clin Nutr*, 77:109–27, 2003.

[85] Sponheimer M, Robinson T, Ayliffe L, Roeder B, Hammer J, Passey B, West A, Cerling T, Dearing D, and Ehleringer J. Nitrogen isotopes in mammalian herbivores: Hair δ^{15}N values from a controlled feeding study. *International Journal of Osteoarchaeology*, 13:80–87, 2003.

[86] Huelsemann F, Flenker U, Koehler K, and Schaenzer W. Effect of a controlled dietary change on carbon and nitrogen stable isotope ratios of human hair. *Rapid Communications in Mass Spectrometry*, 23:2448–2454, 2009.

[87] Henderson GL. Mechanisms of drug incorporation into hair. *Forensic Science International*, 63:19–29, 1993.

[88] Cooper GAA, Kronstrand R, and Kintz P. Society of Hair Testing guidelines for drug testing in hair. *Forensic Science International*, 2011.

[89] Sachs H. History of hair analysis. *Forensic Science International*, 84:7–16, 1997.

[90] Selavka CM and Rieders F. The determination of cocaine in hair: A review. *Forensic Science International*, 70:155–164, 1995.

[91] Staub C. Analytical procedures for determination of opiates in hair: A review. *Forensic Science International*, 70:111–123, 1995.

[92] Crawford K, McDonald RA, and Bearhop S. Applications of stable isotope techniques to the ecology of mammals. *Mammal Review*, 38(1):87–107, 2008.

[93] Cerling TE, Wittemyer G, Ehleringer JR, Remien CH, and Douglas-Hamilton I. History of animals using isotope records (HAIR): A 6-year dietary history of one family of African elephants. *Proc Nat Acad Sciences (USA)*, 106:8093–8100, 2009.

[94] Petzke KJ, Fuller BT, and Metges CC. Advances in natural stable isotope ratio analysis of human hair to determine nutritional and metabolic status. *Current opinion in clinical nutrition and metabolic care*, 13(5):532–540, 2010.

[95] Schwertl M, Auerswald K, and Schnyder H. Reconstruction of the isotopic history of animal diets by hair segmental analysis. *Rapid Communications in Mass Spectrometry*, 17:1312–1318, 2003.

[96] Wainhaus SB, Tzanani N, Dagan S, Miller ML, and Amirav A. Fast analysis of drugs in a single hair. *J Am Soc Mass Spectrom*, 9:1311–1320, 1998.

[97] Lebeau MA, Montgomery MA, and Brewer JD. The role of variations in growth rate and sample collection on interpreting results of segmental analyses of hair. *Forensic Science International*, 210:110–116, 2011.

[98] Sachs H. Theoretical limits of the evaluation of drug concentrations in hair due to irregular hair growth. *Forensic Science International*, 70:53–61, 1995.

[99] Chase HB. Growth of the hair. *Physiol Rev*, 34:113–126, 1954.

[100] Kligman AM. The human hair cycle. *J Invest Dermatol*, 33:307–316, 1959.

[101] Myers RJ and Hamilton JB. Regeneration and rate of growth of hairs in man. *Annals of the New York Academy of Sciences*, 53:562–568, 1951.

[102] Lee SH, Kwon OS, Oh JK, Park WS, Moon SE, and Eun HC. Bleaching phototrichogram: an improved method for hair growth assessment. *J Dermatol*, 32(10):782–787, 2005.

[103] West AG, Ayliffe LK, Cerling TE, Robinson TF, Karren B, Dearing MD, and Ehleringer JR. Short term diet changes revealed using stable carbon isotopes in horse tail-hair. *Functional Ecology*, 18:616–624, 2004.

[104] Wittemyer G, Cerling TE, and Douglas-Hamilton I. Establishing chronologies from isotopic profiles in serially collected animal tissues: An example using tail hairs from African elephants. *Chemical Geology*, 263:3–11, 2009.

[105] Ehleringer JR, Thompson AH, Podlesak DW, Bowen GJ, Chesson LA, Cerling TE, Park T, Dostie P, and Schwarcz H. A framework for the incorporation of isotopes and isoscapes in geospatial forensic investigations. In West JB et al., editor, *Isoscapes: Understanding movement, pattern, and process on earth through isotope mapping*, chapter 17, pages 357–387. Springer, 2010.

[106] Passey BH, Cerling TE, Schuster GT, Robinson TF, Roeder BL, and Krueger SK. Inverse methods for estimating primary input signals from time-averaged intra-tooth isotope profiles. *Geochim Cosmochim Acta*, 69:4101–4116, 2005.

[107] Vogel CR. *Computational Methods for Inverse Problems*. SIAM, 2002.

[108] Cerling TE, Wittemyer G, Rasmussen HB, Vollrath F, Cerling CE, Robinson TJ, and Douglas-Hamilton I. Stable isotopes in elephant hair document migration patterns and diet changes. *Proc Nat Acad Sciences (USA)*, 103(2):371–373, 2006.

[109] Kennedy CD, Bowen GJ, and Ehleringer JR. Temporal variation of oxygen isotope ratios (δ^{18}O) in drinking water: Implications for specifying location of origin with human scalp hair. *Forensic Science International*, 208:156–166, 2011.

[110] Bowen GJ and Wilkinson B. Spatial distribution of δ^{18}O in meteoric precipitation. *Geology*, 30(4):315–318, 2002.

[111] O'Brien DM and Wooller MJ. Tracking human travel using stable oxygen and hydrogen isotope analyses of hair and urine. *Rapid Communications in Mass Spectrometry*, 21(15):2422–2430, 2007.

[112] Ehleringer JR, Bowen GJ, Chesson LA, West AG, Podlesak DW, and Cerling TE. Hydrogen and oxygen isotope ratios in human hair are related to geography. *Proc Nat Acad Sciences (USA)*, 105(8):2788–2793, 2008.

[113] Cerling TE, Passey BH, Ayliffe LK, Cook CS, Ehleringer JR, Harris JM, Dhidha MB, and Kasiki SM. Orphans' tales: Seasonal dietarry changes in elephants from Tsavo National Park, Kenya. *Palaeogeogr Palaeoclim Palaeoecol*, 206:367–376, 2004.

[114] Cerling TE, Ayliffe LK, Dearing MD, Ehleringer JR, Passey BH, Podlesak DW, Torregrossa AM, and West AG. Determining biological tissue turnover using stable isotopes: The reaction progress variable. *Oecologia*, 151:175–189, 2007.

[115] Bowen GJ, Ehleringer JR an Chesson LA, Stange E, and Cerling TE. Stable isotope ratios of tap water in the contiguous United States. *Water Resour Res*, 43:1–12, 2007.

[116] Van Scott EJ, Reinertson RP, and Steinmuller RJ. The growing hair root of the human scalp and morphological changes therein following ametropin therapy. *J Invest Dermatol*, 29:197–204, 1957.

[117] Williams LJ, White CD, and Longstaffe FJ. Improving stable isotopic interpretations made from human hair through reduction of growth cycle error. *American Journal of Physical Anthropology*, 145:125–136, 2011.

[118] Ayliffe LK, Cerling TE, Robinson T, West AG, Sponheimer M, Passey BH, Roeder B, Dearing MD, and Ehleringer JR. Turnover of carbon isotopes in tail hair and breath CO_2 of horses fed an isotopically varied diet. *Oecologia*, 151:175–189, 2007.

[119] Lu P, Nakorchevskiy A, and Marcotte E. Expression deconvolution: A reinterpretation of DNA microarray data reveals dynamic changes in cell populations. *Proc Nat Acad Sciences (USA)*, 100:10370–10375, 2003.

[120] Bar-Joseph Z, Rosenfield R, Farkash S, Simon I, and Gifford DK and. Deconvolving cell cycle expression data with complementary information. *Bioinformatics*, 20:23–30, 2004.

[121] Rowicka M, Kudlicki A, Tu BP, and Otwinowski Z. High-resolution timing of cell cycle-regulated gene expression. *Proc Nat Acad Sciences (USA)*, 104:16892–16897, 2007.

[122] Siegal-Gaskins D, Ash JN, and Crosson S. Model-based deconvolution of cell cycle time-series data reveals gene expression details at high resolution. *PLoS Computational Biology*, 5(8):e1000460, 2009.